2017

Electron Yield Measurements of High-Yield, Low-Conductivity Dielectric Materials

Justin Christensen
Utah State University

ELECTRON YIELD MEASUREMENTS OF HIGH-YIELD, LOW-CONDUCTIVITY DIELECTRIC MATERIALS

by

Justin Christensen

A thesis submitted in partial fulfillment
of the requirements for the degree

of

MASTER OF SCIENCE

in

Physics

Approved:

_____	_____
JR Dennison, Ph.D. Major Professor	D. Mark Riffe, Ph.D. Committee Member
_____	_____
Farrell Edwards, Ph.D. Committee Member	Mark R. McLellan, Ph.D. Vice President for Research and Dean of the School of Graduate Studies

UTAH STATE UNIVERSITY
Logan, Utah

2017

ABSTRACT

ELECTRON YIELD MEASUREMENTS OF HIGH-YIELD, LOW-CONDUCTIVITY DIELECTRIC MATERIALS

by

Justin Christensen, Master of Science

Utah State University, 2017

Major Professor: Dr. JR Dennison
Department: Physics

This study focuses on electron-induced electron emission from materials, through the measurement of a material property called electron yield; this is defined as the ratio of emitted-to-incident electrons at a specific incident energy. Electron yield determines whether a material will charge negatively or positively under incident electron bombardment. While this has been studied extensively for conductive materials, electron yield information is lacking for high-yield, low-conductivity materials. Charging of these materials during measurement affects the sample charge and thereby, the electron yield. This thesis focuses on the improvement and development of methods to measure the (intrinsic) yield of uncharged insulating materials.

Methods implemented include efforts to make measurements with small amounts of charge and to neutralize acquired charge between measurements. To minimize charge used for measurements fast, sensitive current sensors, as well as short-pulsed electron beams, are implemented. Charge neutralization techniques use low-energy electron flooding to neutralize positive sample charge and ultraviolet (UV) irradiation to neutralize negative charge through the photoelectric effect.

To validate and quantify the improvements made in this study, tests were developed to demonstrate improvements in noise reduction, charge neutralization, pulsed-beam properties, and data analysis. These tests display a reduction in charge used per pulse from ~500 to 400 fC with the future potential to reach sensitivities of ~20 fC (10^5 electrons) per measurement using a point-wise calculation

method. Charge neutralization techniques are shown to be much more effective; however, UV irradiation does not fully neutralize materials with large work functions. Yield measurements of high-yield, low-conductivity materials were only partially neutralized. These materials were sapphire (Al_2O_3), polyether ether ketone (PEEK), and quartz (SiO_2).

(127 pages)

PUBLIC ABSTRACT

ELECTRON YIELD MEASUREMENTS OF HIGH-YIELD, LOW-CONDUCTIVITY DIELECTRIC MATERIALS

Justin Christensen, Master of Science

Utah State University, 2017

Materials exposed to the space plasma environment acquire electric charge, which can have harmful effects if it leads to arcing or electrostatic breakdown of important spacecraft components. In fact, spacecraft charging is the leading environmentally induced cause of spacecraft anomalies. This study focuses on measuring electron yield, a property of materials that describes how many electrons are ejected from a material under energetic electron bombardment, which can vary depending on the energy of incident electrons. Intrinsic electron yield is defined as the average number of electrons emitted per incident electron from an electrically neutral material. The specific aim of this work is to improve yield measurements for insulator materials, which can be difficult to test using conventional methods due to charge accumulation in insulators.

Most studies of electron yield use a steady current electron beam in a vacuum chamber to irradiate materials to be tested. By comparing the amount of current deposited in the material to the total incident current, the emitted current can be calculated. This works well for conductors; however, insulators charge up quickly, which either repel incident electrons or reattract emitted electrons producing erroneous yield measurements. This study improves on methods that use a pulsed electron beam to measure yield with small amounts of charge per pulse, as well as neutralization methods to dissipate stored charge between pulse measurements.

The improvements to instrumentation and data analysis techniques are quantified to demonstrate their validity. These improvements will allow for continued studies on extreme insulator materials. Future studies will provide new understanding of interactions between electron radiation and materials, which will allow for better modeling of spacecraft charging and the development of materials that meet desired electron emission specifications.

ACKNOWLEDGMENTS

I want to give a special thank you to all of the people who worked alongside me through all of my undergraduate and graduate work. I want to thank JR Dennison, my mentor, for giving me the opportunity to work in the Materials Physics Group and for the countless hours he spends helping students acquire the skills and knowledge to take their next steps in life. I want to thank him for his patience with me and for continuing to encourage and push me through the challenging weeks.

I want to thank all of the other members of the Materials Physics Group for offering their talents and moral support, as well as for keeping life interesting. I want to thank former members of the group including Justin Dekany and Amberly Jensen for welcoming me into the group and teaching me the skills that have helped me in my research studies. I also want to thank Jordan Lee for the hours he spent taking data to help me finish on time, and for asking lots of questions. Thinking of ways to explain what I was trying to do helped me solve many of the problems in this thesis.

This research would not have been possible without funding from the Utah NASA Space Grant Consortium and NASA Goddard Space Flight Center, which supported me and my family and allowed me to focus on my studies and thesis work.

Lastly, and most importantly, I want to thank my wife, Sarah, for supporting me emotionally, for being patient through the long hours of work, and for being my best cheerleader. I really could not have accomplished this without you.

Justin Christensen

CONTENTS

Page

LIST OF TABLES

Table Page

LIST OF FIGURES

Figure Page

LIST OF SYMBOLS

Symbol

b = range coefficient

b_1 = double exponent range coefficient 1

b_2 = double exponent range coefficient 2

C_{sample} = sample capacitance

ΔT_{ToF} = temporal spacing in time of flight calculations

E_0 = incident beam energy

E_{cross} = crossover energy

$E_{\max}$ = incident energy where δ_{max} or η_{max} occurs

E_1 = first crossover energy

E_2 = second crossover energy

$f(z)$ = actual electron beam shape

I_{in} = incident current

I_{out} = emitted current

I_{coll} = collector current

I_{stage} = stage current

I_{grid} = grid current

I_{sample} = sample current

k = material parameter for Chung Everhart model

$M(s)$ = measured Faraday current at a vertical position s

m = stopping power exponent

m_e = electron mass

N_{in} = number of incident electrons per pulse

N_p = number of data points in the pulse segment of an oscilloscope trace

$n(z, E_0)$ = energy, and depth-dependent number of SEs produced per material thickness *dz*

n = range power exponent

n_1 = double exponent range exponent 1

n_2 = double exponent range exponent 2

$P(z)$ = depth-dependent SE escape probability

Q_0 = initial charge deposited in the sample at the beginning of TEY decay run

Q_{dep} = total charge deposited in the sample

Q_{inc} = total charge incident on the sample

Q_{out} = total charge emitted from the sample

$R(E_0)$ = energy-dependent range

r = radius of Faraday cup

$S(E_0)$ = stopping power. Also denoted $-\frac{dE}{dz}$

t = time

$U(z)$ = Faraday cup response curve

V_{sample} = surface potential of a charged sample

V_{bias} = voltage applied to the biased grid

z = depth in material perpendicular to surface

$Z(E_0)$ = energy-dependent penetration depth

β = secondary electron escape coefficient

$\Gamma_{\mathrm{element}}$ = collection efficiency of an element of the HGRFA

Γ_{lost} = fraction of emitted electrons that leave the HGRFA through the drift tube

$\Gamma_{\mathrm{coll}}^{\mathrm{BSE}}$ = fraction of emitted BSEs that are captured by the collector

γ = combined coefficient in SEY model

$\delta(E_0)$ = energy-dependent secondary electron yield

δ_{max} = maximum secondary yield

ε_m = average (mean field) energy required to excite a secondary electron

ε_T = fractional transmission of the hemispherical grids

$\eta(E_0)$ = energy-dependent backscattered electron yield

η_0 = asymptotic backscattered electron yield for large incident energies

η_{max} = maximum backscattered electron yield

θ_{PE} = incident angle of primary electrons

θ_{SE} = emission angle of secondary electron

λ_{SE} = distance for SE emission probability to fall by a factor of 1/*e*

$\sigma(E_0)$ = energy-dependent total electron yield

$\sigma_0(E_0)$ = energy-dependent intrinsic electron yield

σ_{DC} = DC yield measurement

$\sigma_{pt-wise}$ = point-wise yield measurement

σ_{pulsed} = pulsed yield measurement

σ_{width} = beam profile Gaussian function width parameter

χ = electron affinity of material

LIST OF ABBREVIATIONS

BSE	Backscattered Electron
BSEY	Backscattered Electron Yield
CSDA	Continuous Slow Down Approximation
DAQ	Data Acquisition
ESD	Electrostatic Discharge
FC	Faraday Cup
HGRFA	Hemispherical Grid Retarding Field Analyzer
HOPG	Highly Ordered Pyrolytic Graphite
LED	Light Emitting Diode
MPG	Materials Physics Group
NASCAP	NASA Charging Analyzer Program
PE	Primary Electron
PMT	Photo Multiplier Tube
RIC	Radiation Induced Conductivity
SE	Secondary Electron
SEEM	Space Environment Effects Materials
SEM	Scanning Electron Microscope
SEY	Secondary Electron Yield
TEY	Total Electron Yield
UHV	Ultrahigh Vacuum
USU	Utah State University
UV	Ultraviolet
1D	One Dimensional
3D	Three Dimensional

CHAPTER 1

INTRODUCTION

If you heard the phrase space environment in a sentence, what types of things would come to your mind? You might imagine what would happen to a person exposed to the ultrahigh vacuum (UHV) sucking the air from their lungs and causing bubbles to form in their bloodstream, or the extreme hot and cold temperatures, which occur when going from solar exposure to shadows. If you are really smart you might even know about high-velocity micrometeorite dust, which can blast holes through objects like microscopic bullets. But, most people are unaware of one other harsh space environment condition… plasma-induced electrical charging.

When materials are bombarded by energetic electrons, they can acquire either negative or positive net charge. Negative charging occurs when incident electrons are embedded in the material. Positive charging occurs when electrons are ejected from within the material by deposited energy. Because materials charge differently from one another under various incident electron energies, huge potential differences can develop between adjacent spacecraft components. This can lead to electrostatic discharge (ESD) around and through insulators, which can damage sensitive electronics, optics, and mechanical components vital to the proper functionality of the satellite. In fact, electrostatic discharge due to differential charging of spacecraft materials has been shown to be the leading cause of environmentally induced spacecraft anomalies (Hastings and Garrett, 1996). Electron emission is also very important in other areas of science, such as scanning electron microscopy (SEM), particle accelerators, photomultiplier tubes (PMTs), and the multipactor effect. The process by which materials acquire charge under electron bombardment can be better understood by studying a material-dependent property termed electron yield. The measurement of electron yield, particularly for low-conductivity, high-yield dielectric materials, which cause most spacecraft charging events, is the focus of this thesis.

1.1. Nature of Electron Yield

The energy-dependent electron yield of a material under electron irradiation is defined as the average number of emitted electrons per incident electron at a given incident energy. Total yield values less

than one indicate that a material gains more electrons than it is loses and therefore, charges negatively, while a value greater than one produces positive charging (see Fig. 1.1). To understand how impinging negative charges can produce either positive or negative charging, consider the origin of the emitted electrons.

Two types of electrons can be emitted from a material under electron bombardment (see Section 2.1). The first, termed backscattered electrons or BSEs, are primary electrons (PE), which originate in the incident beam and undergo any number of quasi-elastic collisions inside the material before being scattered back out of the material surface. These electrons generally have energies close to the incident energy due to their minimal energy loss. Conservation of energy sets an upper bound on BSE energy equal to the incident electron energy, E_0. This occurs when an incident electron undergoes only an elastic collision with no inelastic energy loss. Because they originate and end up outside the material, BSEs do not contribute to sample charging.

The second type of emitted electrons are secondary electrons or SEs. These electrons originate in the material and are excited by the energy deposited by incident, or primary, electrons. These tend to have energies much lower than the beam and their loss is responsible for positive charging.

Each variety of emitted electrons has their own yield named backscattered electron yield (BSEY),

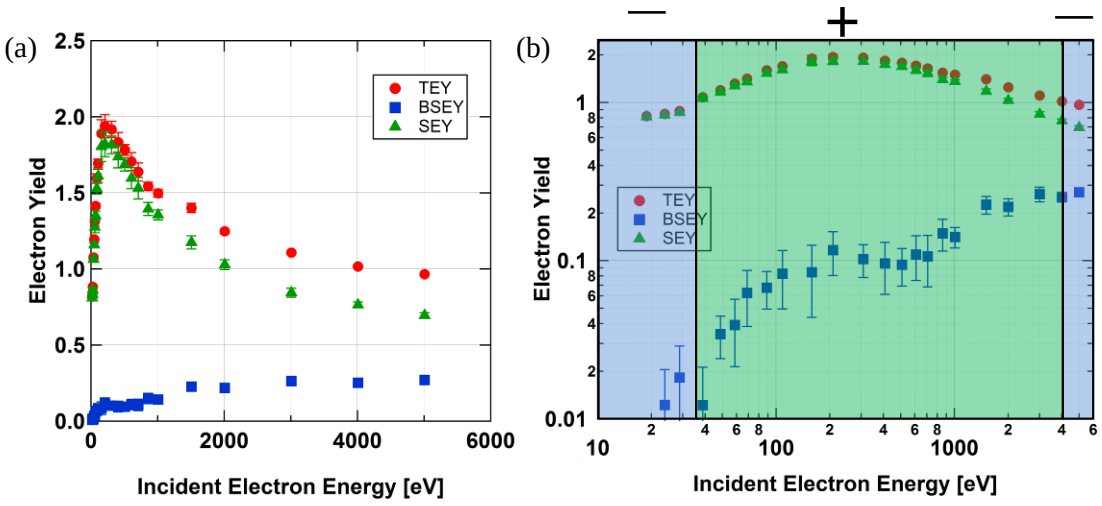

FIG. 1.1. Total electron yield variation for different incident electron energies. These figures show tungsten TEY, BSEY, and SEY measurements over a range of different energies. Axes are in (a) linear, and (b) logarithmic form. Figure (b) shows different energy regimes, which produce negative or positive charging, denoted by – and + symbols, respectively.

and secondary electron yield (SEY). When both are measured together, the resulting yield is the total electron yield (TEY), which is just the sum of BSEY and SEY. A common experimental convention separates these electrons by their emission energy; electrons emitted at <50 eV are termed SEs and those with emission energies >50 eV are termed BSEs.

As discussed in detail in Chapter 2, electron yield is dependent on the energy of incident electrons. A typical yield versus incident electron energy curve has three energy regions (see Fig. 1.1). The first low-energy region has negative charging, because incident electrons do not have enough energy to excite many SEs out of the material. As the incident energy is increased, the measured total yield values of a material usually rise above one because more energy is deposited exciting more SEs. This occurs at what is called the first crossover energy or E_1. At even higher energies, the electron yield peaks (at E_{max}) and begins to fall with increasing incident energy because primary electrons begin to penetrate deep enough into the material that most excited electrons are not likely to reach the surface and the yield drops below one again. This is called, not surprisingly, the second crossover energy or E_2. The two crossover energies are special because at these points, no net charge is deposited in the material.

1.2. Yield Measurements

The basic concept used to measure electron yield is as follows. A sample is exposed to an electron beam of a known energy and current in a UHV chamber, and emitted electron current is measured. The ratio of measured emitted current to incident current then gives the electron yield. (For more information see Chapter 3.) The actual details of how incident and emitted current are measured can differ depending on the type of collection apparatus used. For example, some researchers measure the incident beam current before irradiating their sample and then measure the current that flows from the sample to ground to determine the amount of charge deposited. The Utah State University (USU) Materials Physics Group (MPG) uses a different method where the sample being studied is enclosed inside a hemispherical-grid retarding-field analyzer, or HGRFA, which captures nearly all of the emitted electrons (Nickles, 2002; Hoffmann, 2010). The HGRFA allows for the simultaneous measurement of both the incident and emitted charge. This method minimizes measurement errors that would occur as a result of instability of electron gun emission current or beam alignment.

If the material being irradiated is electrically isolated from ground, (i.e., an insulator or floating conductor), it will develop a surface voltage, which modifies the TEY by either changing the landing energy of primary electrons or reattracting low-energy, secondary electrons (Fig. 1.2). Because of this, it is desirable to measure the yield of an uncharged sample, or the intrinsic yield. The TEY of insulators can be very difficult to measure because the act of measuring causes charge build up, which will alter further measurements. Some attempts have been made in the past to fix this problem (Hoffmann, 2010; Chen, *et al.*, 2011; Gineste, *et al.*, 2014; Dennison, *et al.*, 2016a; Montero, *et al.*, 2016). The USU MPG developed a system for making sensitive, low-current, pulsed beam measurements to reduce the charging, which occurs with each measurement (Thomson, *et al.*, 2003; Hoffmann, 2010). We also use a low-energy electron flood gun to neutralize positive charge on the material surface and an ultraviolet (UV) light-emitting diode (LED) to neutralize negative charge through the photoelectric effect and radiation-induced conductivity (RIC) between each pulse.

1.3. Overview of Thesis Objectives and Proposed Experiments

While novel techniques developed by the USU MPG have been able to greatly improve our ability to measure the electron yield of insulators, there are still problems with charging in extreme insulators, which have made yield measurement very difficult. Previous charging tests have shown that substantial charging has occurred even within one pulse measurement (Hoffmann, 2010). Fig. 1.2 shows consecutive

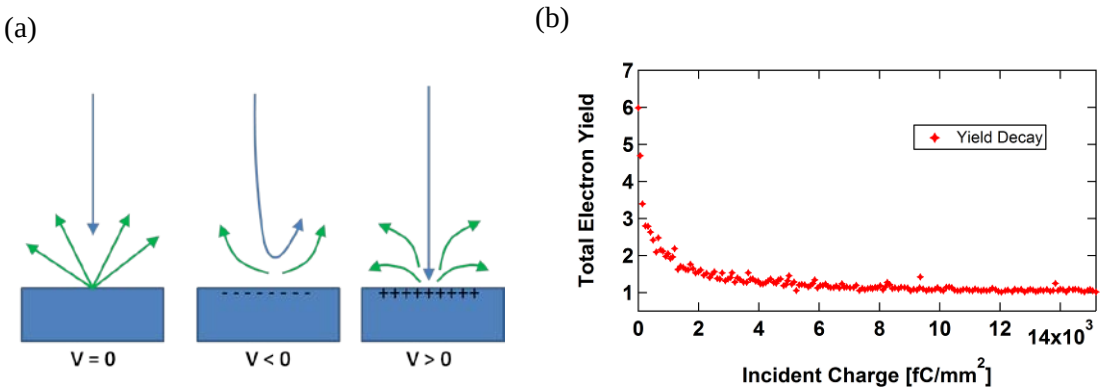

FIG. 1.2. Effects of charge buildup on yield measurements. (a) Charge buildup in insulators during electron yield measurement affects the trajectories of incident and emitted electrons. (b) Yield decay curve for single crystal sapphire at 600 eV.

yield measurements on single crystal sapphire at an incident energy of 608 eV without sample discharge between pulses. The shape of this curve shows how the resulting charge build-up from yield measurements causes a shift in the measured yield value towards an eventual steady state where just as much charge is deposited as is emitted. This results in an asymptotic approach to a yield of one. Because of the low flux output of the electron flood gun and the low-energy UV technology in the past, neutralization techniques were not adequate enough to remove all charging in high-yield, low-conductivity materials.

The goal of this thesis is to improve the measurement capabilities of our system for these types of materials by decreasing the pulse current and improving the neutralization capabilities of the HGRFA. To do this, new analysis software was developed to improve the sensitivity of our measurements at low incident charge, the electron flood gun was modified to put out a more uniform low-energy electron beam, and new high-energy UV LED technology developed in recent years was utilized.

CHAPTER 2

BACKGROUND

In this chapter, we discuss the theories and other information used to physically describe the processes involved in electron-induced electron emission from materials. To do this, total electron yield (TEY) is broken down into its constituent yields for each type of emitted electron. These are termed secondary electron yield (SEY) and backscattered electron yield (BSEY). Next, a model is set forth that describes SEY as a function of incident electron energy. This provides more information about the various material properties that can affect SEY. Another model is given for BSEY as a function of incident electron energy. Finally, the energy distribution of emitted electrons is used to explain the effect of sample charge buildup on SEY measurements. A deeper understanding of each of these items will allow us to discuss how to study electron emission and improve neutralization methods for charged insulators. It will also hopefully shed some light on the difficulties encountered in such studies.

2.1. Theory of Electron Emission

When incident primary electrons (PEs) impinge on a material, they are either scattered back out of the material (termed backscattered electrons or BSE) or deposited inside (see Fig. 2.1). Scattering can either occur at the material surface or after entering and undergoing one or more collisions with the atoms of the material. Deposition occurs when PEs enter a material, and experience a series of elastic and inelastic collisions scattering and losing energy until they come to a complete stop (Andronov, *et al.*, 2013). Studies of how charge is distributed as a function of depth under electron irradiation have shown that the majority of incident electrons come to a stop in a narrow region centered at a well-defined depth called the range (Wilson and Dennison, 2012).

As the incident electron loses energy to the material, it produces various types of excitations. This can be in the form of lattice vibrations (phonons) or electron excitations. If excited electrons reach the conduction band, they can propagate through the material until they either: (i) decay into a bound state emitting a photon (Jensen, 2014); (ii) are reflected by the work function potential barrier at the surface; or (iii) if their energy is large enough, overcome the work function of the material and are emitted from the

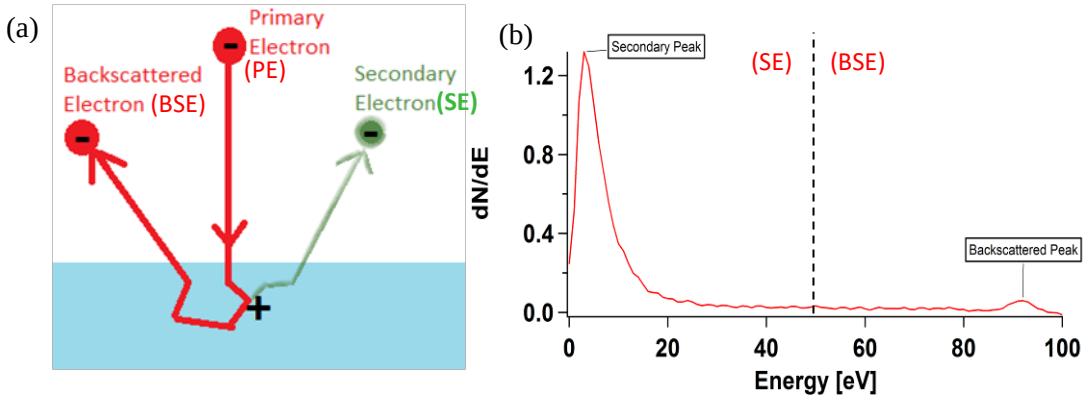

FIG. 2.1. Types of electrons involved in electron-induced electron emission. (a) Interactions between incident electrons and material atoms and electrons. (b) Energy distribution of emitted electrons for Au at a PE energy of ~92 eV. Secondary electrons have energy less than 50 eV by convention, while backscattered electrons have greater energies up to a peak at the incident energy of primaries.

surface (Andronov, *et al.*, 2013). Because these excited secondary electrons, or SEs, are generally produced with low total energies, they must be produced close to and traveling toward the surface to minimize the chances of recapture and energy loss from lattice collisions (Seiler, 1983). Figure 2.1 (b) shows the emitted electron energy distributions for these various types of electrons. Note, the distributions of true SEs and BSEs overlap. Because of this, it is not possible to tell just by looking at the energy of an electron whether it is a SE or BSE. For measuring purposes, secondaries have been given the definition of all emitted electrons with energy less than 50 eV, and BSEs cover all energies greater than 50 eV. To study electron emission from materials, a property called electron yield is defined as the average number of electrons emitted from the material per incident electron,

$$\sigma = \frac{\mathrm{N}_{out}^{\mathrm{e}}}{N_{in}^{\mathrm{e}}}. \tag{2.1}$$

As discussed in Chapter 1, there are also yields for backscattered electrons (BSEY or η) and secondary electrons (SEY or δ). The sum of SEY and BSEY gives the total electron yield (TEY or σ).

2.2. Yield Models

Most empirical models for describing secondary electron yield as a function of PE energy (E_0) take the form of an integral, as follows (Seiler, 1983; Lin and Joy, 2005):

$$\delta(E_0) = \int_0^{R(E_0)} n(z, E_0) P(z) dz, \tag{2.2}$$

where $R(E_0)$ is the range or penetration depth of the primary electrons of energy, E_0, $n(z, E_0)$ is the average number of secondary electrons produced per unit of penetration depth, dz, and $P(z)$ is the probability of a secondary electron reaching the surface from a depth of z. The variations, which are seen between models, come from the assumptions that are made and models used to describe the range, secondary production, and emission probability. Common assumptions are:

- **Limiting problem to one-dimensional (1D) scatter.** The problem is initially limited to normal incidence, with penetration and backscatter only normal to the surface. This assumption can be relaxed, to varying degrees, as noted below.
- **SE production**. The number of electrons produced per unit of penetration depth, *dz*, is proportional to the amount of energy deposited in the same distance,

$$n(z, E_0) = n(E_0) = \frac{-1}{\varepsilon_m}\frac{dE}{dz}. \tag{2.3}$$

  Here, ε_m is the average (mean field) energy required to produce a secondary electron. This assumption also implies that the number of electrons produced is not dependent on depth.

- **The continuous slowdown approximation (CSDA)**. Energy is deposited equally along the primary electrons trajectory from the surface down to the penetration depth. Thus, the stopping power is

$$S(E_0) = \frac{dE}{dz} \rightarrow \frac{dE}{dz} \overset{CSDA}{\longrightarrow} \frac{-E_0}{R(E_0)} \overset{3D}{\rightarrow} \frac{-E_0}{Z(E_0)}. \tag{2.4}$$

  Here, a distinction is made between incident electron range $[R(E_0)]$ (the maximum distance primary electrons can travel along their initial direction once entering the material), and penetration depth, $Z(E_0)$, (the average final depth normal to the surface of the material). While it may not be immediately obvious, there are a few different reasons why the penetration depth for any particular electron may fall short of the range:

  - Stochastic variations in distance between collisions inside the material lead to a distribution of final deposition depths.

- When PEs have an incident angle of θ_{PE} off of normal to the material surface, then the penetration depth normal to the surface will be smaller than the range and given by

$$Z(E_0) = R(E_0)\cos(\theta_{PE}). \quad (2.5)$$

- Each time an electron undergoes a collision, it can be scattered off at an angle relative to its trajectory before the collision. This causes a zig-zag trajectory inside the material, which produces some uncertainty for where the electron will come to rest. These effects are difficult to incorporate into our model, so for the purposes of this thesis, we will only consider deviations in penetration depth due to incident electron angle. With this in mind, combining Eqs. 2.3 and 2.4 gives,

$$n_{CSDA}(E_0) = \frac{1}{\varepsilon_m}\cdot\frac{E_0}{R(E_0)} \overset{3D}{\rightarrow} \frac{1}{\varepsilon_m}\cdot\frac{E_0}{Z(E_0)}. \quad (2.6)$$

- **Probability of emission.** The probability of SEs escaping the material is the product of two terms. An exponential decay term describes the likelihood of electrons reaching the surface from a depth z, and a constant term, (β), describes the probability of the electron overcoming the surface barrier. Together this gives a probability of

$$P(z) = \beta\cdot\alpha\cdot e^{\frac{-z}{\lambda_{SE}}}, \quad (2.7)$$

where λ_{SE} is a depth parameter that has to do with the distance secondary electrons travel before being recaptured. This is commonly taken as the inelastic mean free path of SEs at an average SE energy (typically only a few eV). If we assume 1D scattering, the geometry factor $\alpha^{1D} = 1/2$, given that SE trajectories toward and away from the surface are equally likely. This ignores half of the SEs, which travel deeper into the material. However, this is different for the three-dimensional (3D) case where SEs produced with trajectories not normal to the surface will have to travel a further distance in order to reach the surface (see Fig. 2.2). In this case the role of α is played by an integral over all space. Assuming that SE trajectories are distributed uniformly in every direction, the probability of emission becomes

$$P(z) = \frac{\beta}{4\pi}\int_0^{2\pi} d\phi \int_0^{\pi/2} \sin(\theta_{SE}) e^{\frac{-1}{\lambda_{SE}}\frac{z}{\cos(\theta_{SE})}} d\theta_{SE}$$

$$= \frac{\beta}{2}\int_0^{\pi/2} \sin(\theta_{SE}) e^{\frac{-1}{\lambda_{SE}}\frac{z}{\cos(\theta_{SE})}} d\theta_{SE} = \frac{\beta}{2}\int_0^1 e^{\frac{-z}{\lambda_{SE}}\frac{1}{h}} dh, \quad (2.8)$$

where $h \equiv \cos(\theta_{SE})$.

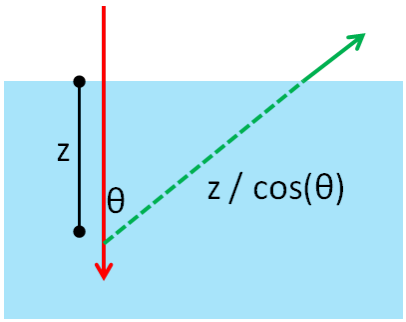

FIG. 2.2. 3D path length diagram. This figure shows how the distance a SE travels before it reaches the surface depends on the angle of its trajectory.

- **Electron Range.** Various choices for the electron range model produce slightly different yield curve shapes. The most typical models for the range use a power law; Table 2.1 lists several common models of the form $R(E_0) = bE_0{}^n$ with different values for n. A somewhat more general form, used in the seminal spacecraft charging code NASCAP (Mandell, *et al.*, 2005), approximates the range as the sum of two power laws (Katz, *et al.*, 1977).

$$R_N(E_0) = b_1 E_0{}^{n_1} + b_2 E_0{}^{n_2}. \tag{2.9}$$

Table 2.1. Range models.

Model	n	$\frac{R(E_{max})}{\lambda_{SE}}$
(Young, 1956)	1.35	2.283
(Viatskin and Makhov, 1958)	1.4	2.138
(Lane and Zaffarano, 1954)	1.67	1.614
(Seiler, 1983)	1.8	1.45
(Terrill, 1923)	2	1.256
(Whiddington, 1912)	2	1.256

There is at least empirical evidence that the two exponents are related as $n_1 = 1 - \alpha$, $n_2 = 1 + \alpha$, and $n_1 + n_2 = 2$. Wilson develops a similar range model applicable over a wider range of energies (Wilson and Dennison, 2012)

2.2.1. 1D Yield Model

Taking these assumptions together, Eq. (2.1) for SEY in 1D gives

$$\delta_{CSDA}^{1D}(E_0) = \frac{\beta}{2\varepsilon_m}\frac{E_0}{R(E_0)} \cdot \int_0^{R(E_0)} e^{\frac{-z}{\lambda_{SE}}} dz = \frac{\beta\lambda_{SE}}{2R(E_0)}\frac{E_0}{\varepsilon_m}\left(1 - e^{-\frac{R(E_0)}{\lambda_{SE}}}\right). \quad (2.10)$$

Using the simplest single power law range model of $R(E_0) = bE_0{}^n$ in Eq. (2.10) simplifies the equation to

$$\delta_{CSDA}^{1D}(E_0) = \frac{\lambda_{SE}}{2b}\frac{\beta E_0{}^{1-n}}{\varepsilon_m}\left(1 - e^{-\frac{bE_0{}^n}{\lambda_{SE}}}\right) = \frac{\beta}{2\gamma}\frac{E_0{}^{1-n}}{\varepsilon_m}\left(1 - e^{-\gamma E_0{}^n}\right), \quad (2.11)$$

where $\gamma = b/\lambda_{SE}$. Since β and ε_m both appear as multiplicative constants, they can be combined into one constant. This has the same result as setting either of them constant. All work in this thesis assumes that β=1.

Eq. 2.11 can be differentiated and set equal to zero to find the maximum yield, δ_{max}, and corresponding energy, E_{max} (Dionne, 1975). This is, however, impossible to solve analytically and so Dionne develops a simple relationship, which can be solved numerically for the ratio

$$\frac{R(E_{max})}{\lambda_{SE}} = \left(1 - \frac{1}{n}\right)\left(e^{\frac{R(E_{max})}{\lambda_{SE}}} - 1\right), \quad (2.12)$$

at E_{max}. These ratios for values of n found in the literature are included in Table 2.1.

To understand how Eq. (2.11) behaves, it is first instructive to graph the function with different parameters. In different limits of the secondary yield model, the function can be approximated by power laws. Because of this, it is much more instructive to graph the secondary yield versus energy using log-log axes because this produces straight lines at low- and high-incident energies. Figure 2.3 shows the effect of varying the power in the range model.

- Notice that higher powers *n* causes the maximum yield value (δ_{max}) to decrease. Increasing *n* increases the range for a given energy. This causes a drop in the stopping power, which lowers the number of electrons produced per unit of penetration depth (Eq. (2.6)).

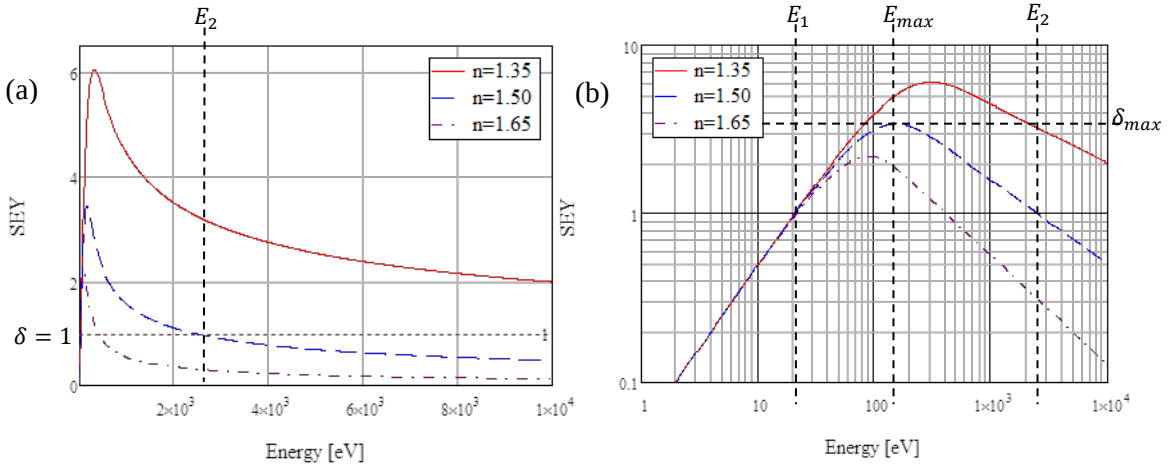

FIG. 2.3. Yield model comparisons. Graphs show the above model (Eq. 2.11) for $\varepsilon_m = 10\,eV$, $\lambda_{SE} = 10\,nm$, and $R(E_0) = bE_0{}^n nm$ with $b = 0.01\,nm$, and $n = 1.35$ (solid), $n = 1.50$ (dashed), and $n = 1.35$ (dot-dashed) in (a) linear and (b) log-log form. Markers indicate first and second crossover energies (E_1 and E_2), as well as the energy of largest yield, E_{max}, with the associated yield at E_{max}, δ_{max}. These markers are for the $n = 1.5$ case.

- Next, notice how increasing *n* causes the function to peak at lower energies (E_0^{max}). Other researchers have noticed that for *n* = 1.35, the maximum in the SEY curve occurs when the $R(E_{max}) = 2.28\,\lambda_{SE}$ (Dionne, 1975) (see Table 2.1). Similar results occur using other values of *n* with slightly different proportionality relationships (see Table 2.1). Because of this, larger values of *n* cause the range to be $\sim\lambda_{SE}$ at a lower energy.
- To get approximate power laws for the low- and high-energy sides of these functions, we can do the following. For small energies, the term in parenthesis in Eq. (2.11) can be approximated using a Taylor expansion of $e^x \cong 1 + x$ with $x \equiv -\gamma E_0{}^n$ such that

$$\delta_{CSDA}^{1D}\left(E_0{}^{small}\right) \cong \frac{1}{2\varepsilon_m}\frac{E_0{}^{1-n}}{\gamma}\left(\gamma E_0{}^n\right) = \frac{E_0}{2\varepsilon_m}, \quad \text{for} \quad \gamma E_0 \ll 1, \tag{2.13}$$

which is linear in E_0 and independent of n and γ. For high energies, the exponential term approaches zero, leaving just the left side of Eq. (2.11),

$$\delta_{CSDA}^{1D}\left(E_0{}^{large}\right) \cong \frac{E_0{}^{1-n}}{2\varepsilon_m\gamma}, \quad \gamma E_0 \gg 1. \tag{2.14}$$

The low-energy approximation says that we should have the same slope on a log-log plot for all low-energy measurements, regardless of material. Measured yield curves, however, can produce different slopes at low energies. Therefore, some models account for this by changing the model to

$$\delta_{m,n}(E_0) = \frac{1}{2\varepsilon_m}\frac{{E_0}^{m-n}}{\gamma}\left(1 - e^{-\gamma {E_0}^n}\right), \tag{2.15}$$

where m gives the slope at low energies (see Fig. 2.4). Using $m = 1$ gives the same result as Eq. (2.11). This physically might relate to an alternate assumption of the stopping power (Eq. 2.4) with a small modification so

$$\left({dE}/{dz} = -\frac{{E_0}^m}{R(E_0)}\right).$$

2.2.2. 3D Yield Model

A more physical model takes into consideration the 3D nature of emitted electron trajectories in the material. Using the 3D model for probability of SE emission (Eq. 2.8), the model for secondary yield becomes

$$\delta_{CSDA}^{3D} = \int_0^{Z(E_0)} \frac{1}{\varepsilon_m} \cdot \frac{E_0}{Z(E_0)} \frac{1}{2} \int_0^1 e^{\frac{-z}{\lambda_{SE}}\frac{1}{\mathrm{h}}} dh\, dz.$$

β is not included because it was absorbed into ε_m (see Section 2.2.1). Changing the order of integration and integrating with respect to z gives.

$$\delta_{CSDA}^{3D} = \frac{E_0}{2\varepsilon_m} \cdot \frac{1}{Z(E_0)} \int_0^1 \mathrm{dh} \int_0^{Z(E_0)} e^{\frac{-1}{\lambda_{SE}\cdot h}\cdot z}\, dz,$$

$$= \frac{E_0}{2\varepsilon_m} \cdot \frac{\lambda_{SE}}{Z(E_0)} \int_0^1 \mathrm{h} \left(1 - e^{\frac{-Z(E_0)}{\lambda_{SE}}\frac{1}{\mathrm{h}}}\right) dh,$$

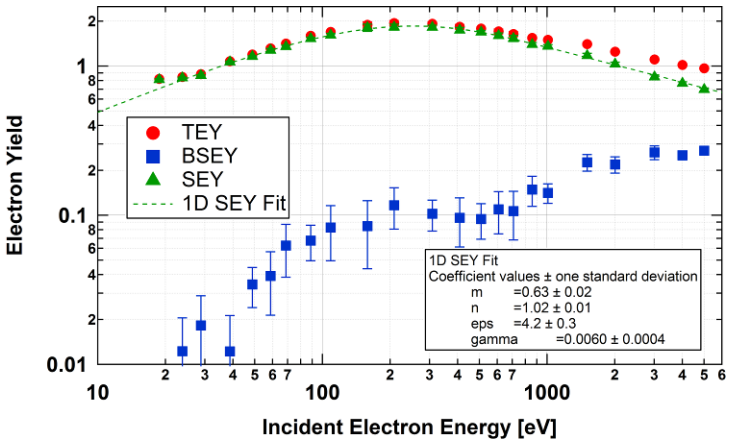

FIG. 2.4. Yield fit of tungsten. This figure shows a fit using Eq. (2.13) to yield measurements on tungsten. The parameters used in the fit are $\varepsilon_m = 4.2 \pm 0.3$, $\gamma = 0.006 \pm 0.0004$, $m = 0.63 \pm 0.02$, and $n = 1.02 \pm 0.01$.

$$= \frac{E_0}{2\varepsilon_m} \cdot \frac{\lambda_{SE}}{Z(E_0)} \left(\frac{1}{2} - \int_0^1 h e^{\frac{-Z(E_0)}{\lambda_{SE}} \cdot \frac{1}{h}} dh \right),$$

$$= \frac{E_0}{2\varepsilon_m} \cdot \frac{\lambda_{SE}}{Z(E_0)} \left(\frac{1}{2} - \int_0^1 h e^{\frac{-Z(E_0)}{\lambda_{SE}} \cdot \frac{1}{h}} dh \right).$$

Finally, substituting $v = \frac{1}{h}$ gives

$$\delta_{CSDA}^{3D} = \frac{E_0}{2\varepsilon_m} \cdot \frac{\lambda_{SE}}{Z(E_0)} \left(\frac{1}{2} - \int_1^\infty \frac{1}{v^3} \cdot e^{\frac{-Z(E_0)}{\lambda_{SE}} v} dv \right).$$

This integral has no elementary function solution. However, there is a special function called the exponential integral defined as

$$Ei(n, x) = \int_1^\infty \frac{1}{v^n} \cdot e^{-x \cdot v} dv,$$

which can be used to give a numerical solution to the equation. This gives a final solution as

$$\delta_{CSDA}^{3D} = \frac{E_0}{2\varepsilon_m} \cdot \frac{\lambda_{SE}}{Z(E_0)} \left(\frac{1}{2} - \mathrm{Ei}\left(3, \frac{Z(E_0)}{\lambda_{SE}}\right) \right). \tag{2.16}$$

Similar to the 1D model for incident beams normal to the surface and using the same power law range model, Eq. 2.16 becomes

$$\delta_{CSDA}^{3D} = \frac{{E_0}^{m-n}}{2\varepsilon_m \gamma} \left(\frac{1}{2} - \mathrm{Ei}(3, \gamma \cdot {E_0}^n) \right). \tag{2.17}$$

The exponent *m* was also included in this model in analogy to Eq. 2.15 for 1D.

It should be expected that allowing SEs to travel at nonperpendicular angles relative to the surface of the material should cause a decrease in the probability of reaching the surface and hence, a decrease in the resulting yield curve. Figure 2.5 shows this drop, which results from using the 3D model. Using the same values of parameters $m,\ n,\ \varepsilon_m$, and γ, there is a significant drop (a factor of 2) in the two models at high energies, as well as a lower value for E_{max} using the 3D model. Note, though that the slopes are still the same for the high and low regions of the curves.

2.3. Backscattered Yield Model

The equations that the USU MPG use to model BSEY as a function of incident energy originate from NASA's spacecraft charging simulation software NASCAP 2k (referred to from here on as NASCAP). The formula that NASCAP uses to model BSEY has little to no physical basis. It was designed

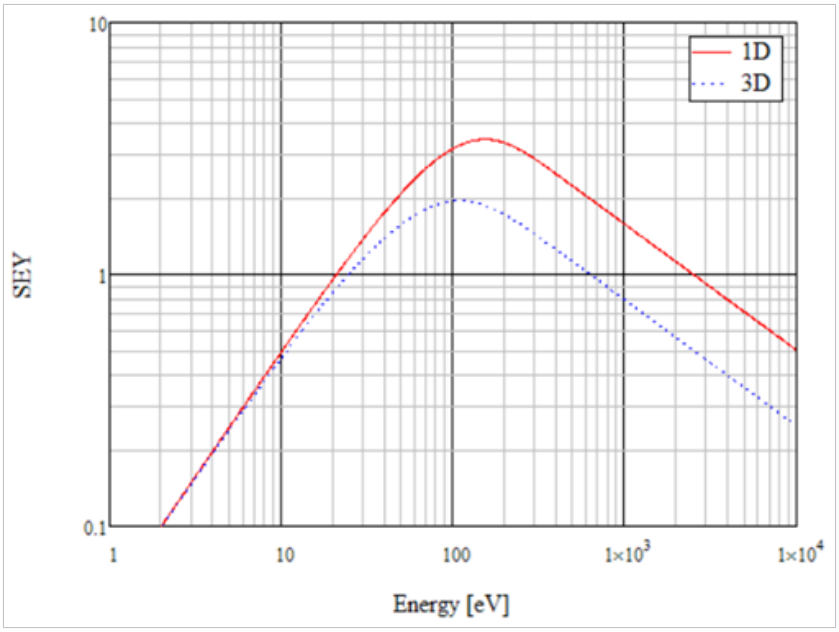

FIG. 2.5. Comparison of 1D and 3D SEY models. The red curve is calculated with Eq. (2.15) and the blue curve with Eq. (2.17), both using m=1, n=1.5, $\varepsilon_m = 10$, and $\gamma = 0.001$.

to reproduce the typical BSEY trends, which have been seen experimentally. This model has a fixed maximum height of 0.1 at 1000 eV, and the only free parameter η_0 adjusts the high-energy asymptotic value.

$$\eta(E_0) = \begin{cases} 0 & if\ E_0 \leq 50\ eV \\ \frac{\log\left({}^{E_0}/_{50\ eV}\right)}{\log\left({}^{1000\ eV}/_{50\ eV}\right)} \cdot \left[0.1 \cdot e^{\frac{-E_0}{5000\ eV}} + \eta_0\right] & if\ 50\ eV < E_0 \leq 1000\ eV \\ \left[0.1 \cdot e^{-\frac{-E_0}{5000\ eV}} + \eta_0\right] & if\ 1000\ eV < E_0 \end{cases}. \quad (2.18)$$

This model rises from zero at 50 eV, to a maximum value at 1000 eV, then it falls asymptotically approaching the constant value of η_0.

Many materials exhibit maximum values at other energies than 1000 eV, and maximum values that do not match what the NASCAP model produces. The USU MPG has modified the NASCAP BSEY model to have three parameters to allow for the maximum BSEY (η_{max}) and energy at maximum yield (E_{max}) to be adjusted, as well. This takes the form of

$$\eta(E_0) = \begin{cases} 0 & if\ E_0 \le 50\ eV \\ \frac{\log\left(E_0/_{50\ eV}\right)}{\log\left(E_{max}/_{50\ eV}\right)} \cdot \left[(\eta_{max} - \eta_0) \cdot e^{\frac{-(E_0 - E_{max})}{E_{max}}} + \eta_0\right] & if\ 50\ eV < E_0 \le E_{max} \\ \left[(\eta_{max} - \eta_0) \cdot e^{\frac{-(E_0 - E_{max})}{E_{max}}} + \eta_0\right] & if\ E_{max} < E_0 \end{cases}. \quad (2.19)$$

Figure 2.6 shows Eq. 2.19 fit to BSEY data for quartz along with a fit to SEY (Eq. 2.17) and their sum to fit TEY data. For more information about these data see Section 4.3.4.2.

2.4. Emitted Electron Energy Distribution

Not only does the number of emitted electrons matter in these studies, but the emitted energy also has a very large bearing on how materials charge up. This section will briefly describe the typical energy spectrum for emitted electrons, as well as how this information can be used to understand changes in yield measurements as samples acquire charge.

The typical emitted electron energy spectrum has two main peaks of interest to us. The first peak is the secondary electron peak, which rises quickly from zero to a peak energy, usually between 2-5 eV, and then decays gradually back to zero with higher energies. This peak usually gets small enough at 50 eV that secondary electrons are defined as electrons with less than 50 eV of kinetic energy. The second peak is

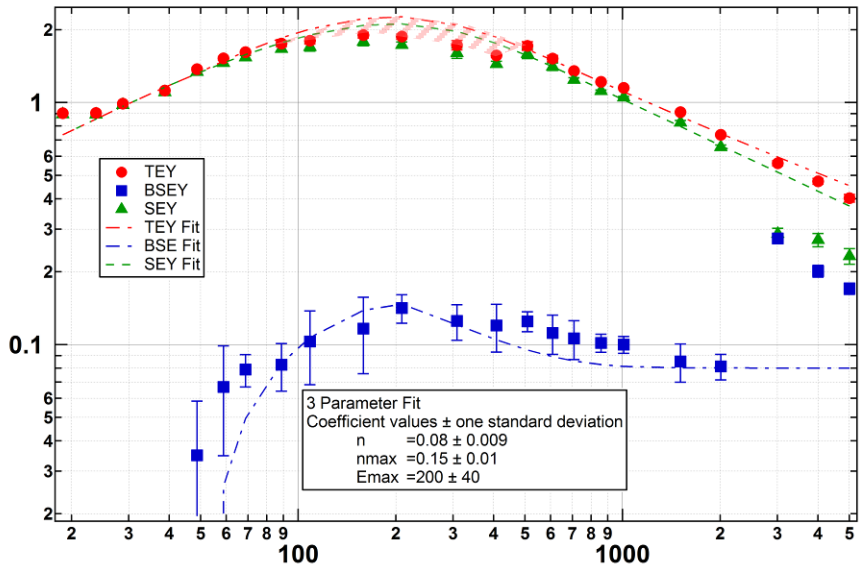

FIG. 2.6. Yield fits to quartz data. Figure shows fits to quartz TEY, SEY (Eq. 2.17), and BSEY (Eq. 2.19) data. The three parameter fit is used for BSEY data to have an adjustable max yield and corresponding incident energy. Shaded region shows discrepancy between data and fit due to positive sample charging.

the backscattered peak, which, by definition, has energy larger than 50 eV. In reality this peak has a maximum very close to the incident beam energy with a shape close to Gaussian and a width given by the thermal distribution of electrons. The measured width, however, is a convolution with the HGRFA response curve (also a Gaussian). The HGRFA response curve has a finite spread due to asphericity of the grids, as well as small fringe fields near the drift tube, both of which cause small deviations from perfectly radial retarding fields. For the new tungsten filament in the pulsed electron gun used here, the thermal source width is ~0.32 eV, which is much smaller than the measured BSE peak width. This suggests that most of the width we see is caused by imperfections of the HGRFA. Nickles (Nickles, 2002) estimated this as ~ 1.5 eV.

One thing to note about the 50 eV definition, is that if the incident beam energy is close to, or less than 50 eV, then the backscattered primary electrons are counted as secondaries. This makes measuring the backscattered yield for incident energies less than 50 eV ill defined. Previous work used models to fit these two peaks, and further studies like this may lead to better definitions for these two types of emitted electrons (Hoffmann, 2010).

If the emitting material is not electrically neutral due to the lack of ability for charges to flow to ground (i.e., floating conductors or insulating materials) then the emitted SE energy spectrum will experience a shift in energy by the surface potential of the material. The BSE peak will not be shifted because it feels the same electric forces traveling toward the sample as it does going away. Because of this, if the incident electrons experience a change in kinetic energy coming into the sample, they will experience the opposite change in energy on the way back out. If the sample potential is positive, the SE spectrum shift leads to a reattraction of low-energy, secondary electrons (Fig. 2.7). This can be used to calculate the measured yield as a function of sample potential by determining the percent decrease in area under the curve when the shaded region is excluded and dropping the yield by the same percentage (Hoffmann, 2010).

The Chung-Everhart model (Chung and Everhart, 1974) describes the emitted SE energy distribution as

$$\frac{dN_{SE}(E,E_0)}{dE} = \frac{k}{E_0}\frac{E}{(E+\chi)^4}, \tag{2.20}$$

where E_0 and E are the incident and emitted electron energies, χ is the electron affinity of the material, and k is a material parameter, which only affects the height of the peak distribution. Hoffmann used this equation to develop another model for the decreased SEY of a material as a function of accumulated sample charge or surface voltage (Hoffmann, 2010). The idea behind his model is that starting with an uncharged sample and a small amount of incident charge, the yield produces a small amount of charge build up, which produces a small change in the sample potential. The next increment of incident charge then has a different yield determined by the sample potential, which produces another small change in built up charge and incremented sample potential. This process progresses until the sample asymptotically approaches a steady potential, which has a yield of one, and the incremental deposited charge is zero (see Fig. 2.8).

The secondary yield as a function of sample potential is found by integration of Eq. 2.20 over the appropriate electron energies. Adding this integral to the backscattered yield (which is assumed to be independent of sample potential), gives

$$\sigma(V_{sample}, E_0) = \left[\frac{1}{N_{inc}} \int_{V_{sample}}^{\infty} \frac{k}{E_0} \frac{E}{(E+\chi)^4} dE\right] + \eta(E_0)$$

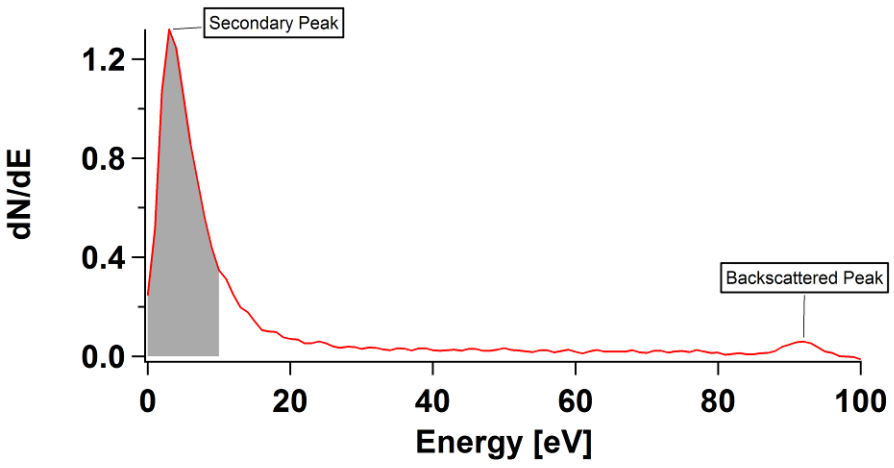

FIG. 2.7. Positive bias emission spectra for Au. If the sample is charged to +10 V, then all secondary electrons with energies less than 10 eV (shaded region) will be reattracted to the sample. This causes a drop in the measured electron yield due to the lowered number of emitted electrons. This data was taken with an incident electron energy of ~ 92 eV.

$$= \left[\frac{1}{N_{inc}}\frac{k}{E_0}\frac{3V_{sample}+\chi}{6(V_{sample}+\chi)^3}\right] + \eta(E_0). \tag{2.21}$$

Assuming that the sample behaves as a capacitor is valid as long as the range for incident electron energies is much smaller than the sample thickness and the conductivity is low enough to neglect the loss of charge via charge migration. This gives the sample potential as

$$V_{Sample} = {Q_{dep}}/{C_{sample}}, \tag{2.22}$$

where Q_{dep} is the charge deposited and C_{sample} is the sample capacitance. To relate the incident charge to deposited charge we need

$$dQ_{dep} = dQ_{inc} - dQ_{out} = dQ_{inc} - dQ_{inc} \cdot \sigma(V_{sample}, E_0)$$
$$= dQ_{inc} \cdot \left(1 - \sigma(V_{sample}, E_0)\right). \tag{2.23}$$

Here, Q_{inc} is the net incident charge, and Q_{out} is the net emitted charge. This differential equation is extremely difficult, if not impossible, to solve analytically for a nice function relating yield to incident charge. It can, however, be approximated numerically as

$$Q_{dep_i} = Q_{dep_{i-1}} + dQ_{inc} \cdot \left(1 - \sigma\left(V_{sample}(Q_{dep_{i-1}}), E_0\right)\right) \tag{2.24}$$

by iterating from the initial condition

$$Q_{dep_0} = Q_0,$$

where Q_0 is the initial charge stored in the sample. Using Eqs. 2.21 and 2.22, the TEY can be expressed as a function of deposited charge. This, along with our numerical approximation (Eq. 2.24) for deposited charge as a function of incident charge, finally allows us to relate TEY to incident charge.

This method for modeling the electron yield with incident charge is very similar to methods that Hoffmann developed. He used these methods because of problems he encountered with high-yield, low-conductivity materials. By measuring yield versus incident charge and fitting his model to the measured curve, Hoffmann was able to extrapolate to the initial yield with zero built-up charge (see Fig. 2.8). This yield at zero charge is termed intrinsic yield or σ_0.

Improvements to measurement and analysis methods, which will be discussed in Chapter 3, will allow for measurements using much smaller incident charge. This will allow for the direct measurement of σ_0 for materials with higher yields and lower conductivities than was previously possible. This will greatly simplify yield measurements due to the difficulty of using Hoffmann's approach.

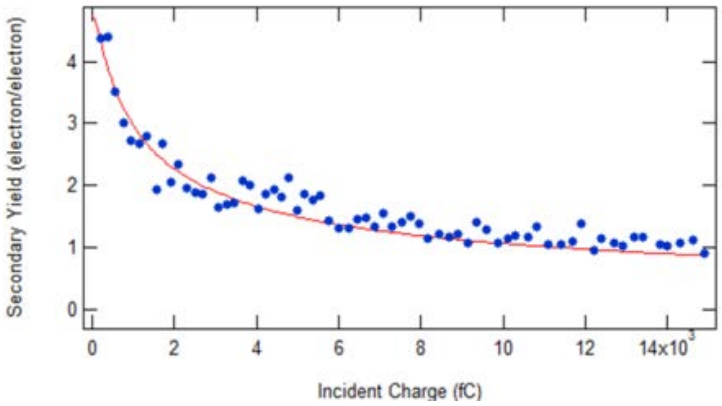

FIG. 2.8. SEY versus incident charge model. The Chung-Everhart model allows for modeling of the electron yield of insulating materials as a function of total incident charge. Graph shows yield decay curve of Al_2O_3 at an incident energy of 200 eV (Hoffmann, 2010).

CHAPTER 3

INSTRUMENTATION AND ENHANCEMENTS

This chapter begins with a description of the facilities and instrumentation used in these studies. It gives an explanation of the techniques used to minimize incident charge during measurements, as well as neutralize sample charge between measurements. The challenges, which have been encountered in the past, are explained. The software and analysis procedures are also discussed.

After explaining the system prior to the start of my research, the improvements are explained. These include physical improvements to the HGRFA and electronics, as well as new analysis methods. With each of these improvements, the expected enhancements to the test results are given.

Table 3.1 shows a list of instruments used in this study with labels that identify them in the text and figures throughout this thesis. When these instruments are mentioned in the remainder of this thesis, the accompanying symbol will be given for clarity.

3.1. Methods of Operation

3.1.1. Space Environment Effects Materials Test Chamber

To study how materials will interact with the space environment, the USU Materials Physics Group uses the Space Environment Effects Materials (SEEM) test chamber to simulate the conditions seen in space (working pressures of ~1×10^{-7} to 5×10^{-9} Torr) (see Fig. 3.1). The SEEM test chamber is equipped with electron guns (20 eV - 30,000 eV) (A, E), an ion gun, heaters and cryostat refrigerator (40 K - 400 K), and various sensors to simulate and measure similar ion fluxes and temperatures to what would be seen in space. The chamber also has a sample carousel (K) which holds nine material samples (J) at a time so multiple tests can be performed each time the vacuum is pumped down.

3.1.2. Electron Sources

There are two electron sources used for electron-yield measurements. The first is a low-energy (~10 eV - 5000 eV) (A), low-current (<100 nA) Staib Instruments electron gun (Model EK-5-S) (Staib-Instruments, 2002). The second, higher-energy (5 keV - 30 keV) (Kimball, Model EGPS-21B) electron gun (E) produces a beam of ~20 nA and beam spots between 0.5 mm to 2 cm diameter. This gun uses a LaB_6

Table 3.1. Thesis instrumentation labels.

Label	Instrument	Figures
A	STAIB Electron Gun	3.1
B	Flood Gun/ LED Feedthrough Box	3.1
C	HGRFA Feedthrough Box	3.1
D	Stage/Inner Grid Bias Box	3.1
E	HEED Electron Gun	3.1
F	Pulse Ammeter Box	3.1
G	Flood Gun Control Box	3.1
H	UV/LED Control Box	3.1
I	Sample Breakout/ DC Ammeter Box	3.1
J	Sample	3.1, 3.2
K	Sample Carousel	3.1
L	Faraday Cup	3.1
M	Liquid Nitrogen Reservoir	3.1
N	HGRFA	3.1, 3.2
O	UVLED	3.2
P	Flood Gun	3.2
Q	Collector	3.2
R	Bias Grid	3.2
S	Inner Grid	3.2
T	Drift Tube	3.2
U	Stage	3.2
V	Beam Aperture	3.6

filament, which runs at a lower temperature than the STAIB gun's W filament, which produces less thermal spread in the emitted electron energies (~ 0.2 eV versus ~ 0.3 eV). All of the studies done in this thesis were done with the Staib electron gun.

3.1.3. Sample Carousel

Samples are mounted inside the chamber on a rotatable sample carousel (K) with a capacity of nine samples (J). It also contains a Faraday cup (FC) (L), which is designed to capture all electrons that enter a ~5 mm diameter opening and allows for the measurement of electron beam shape and current density. The carousel can be programmatically raised or lowered in the chamber to place it in front of the various electron, ion, and photon sources, as well as for sample removal from the chamber. Lastly, the

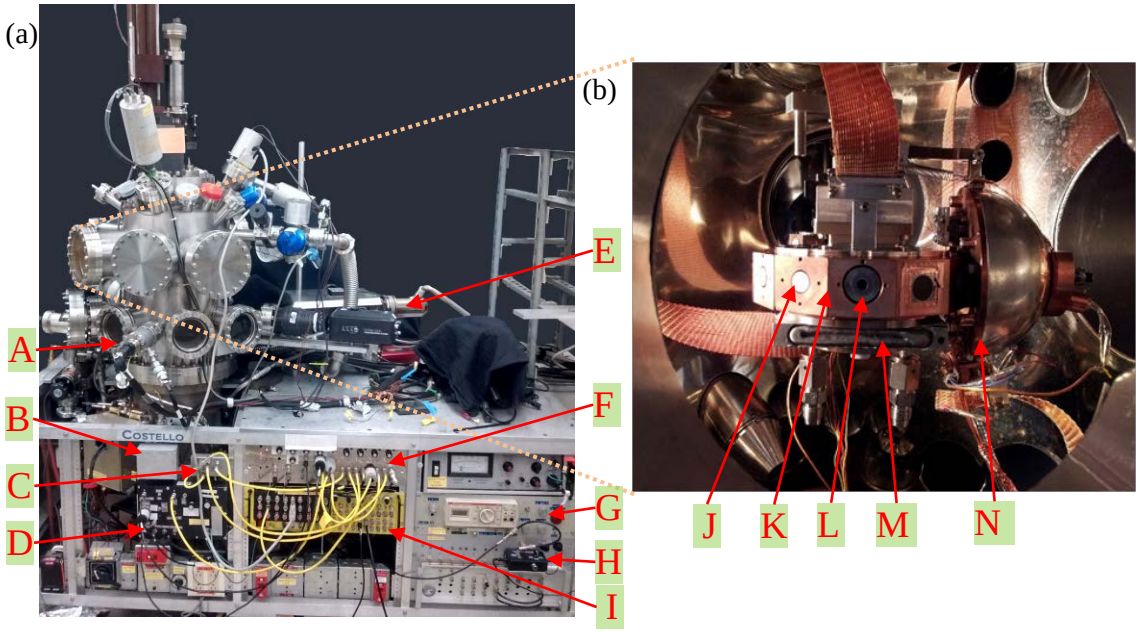

FIG. 3.1. USU SEEM test chamber. (a) The SEEM test chamber is used to produce pressures, temperatures, and electron, ion, and photon fluxes typical for the space environment. (b) Internal view from port window of sample carousel and HGRFA. Labels are defined in Table 3.1.

carousel has a liquid nitrogen reservoir (M), as well as internal sample heaters to allow for temperature-dependent studies to be performed.

3.1.4. Hemispherical-Grid Retarding-Field Analyzer

The hemispherical-grid retarding-field analyzer (HGRFA) (N) was designed to provide a method of accurate, absolute electron yield and emitted electron energy measurement (Chang, *et al.*, 1998; Nickles, 2002). This is accomplished by the complete enclosure of the sample inside the measuring apparatus to maximize electron collection; it also involves the use of voltage-biased grids to produce retarding potentials to measure electrons of various energies (see Fig. 3.2 and Fig. 4.11). The HGRFA is mounted on the sample carousel and is designed to move between samples under vacuum.

3.1.4.1. Absolute Yield Measurement

Yield measurements are made by directing an electron beam into the HGRFA through a 3 mm opening in the drift tube (T) opposite from the sample (J). This beam then impinges on the sample depositing some charge inside the material; emitted electrons are captured by a solid hemispherical

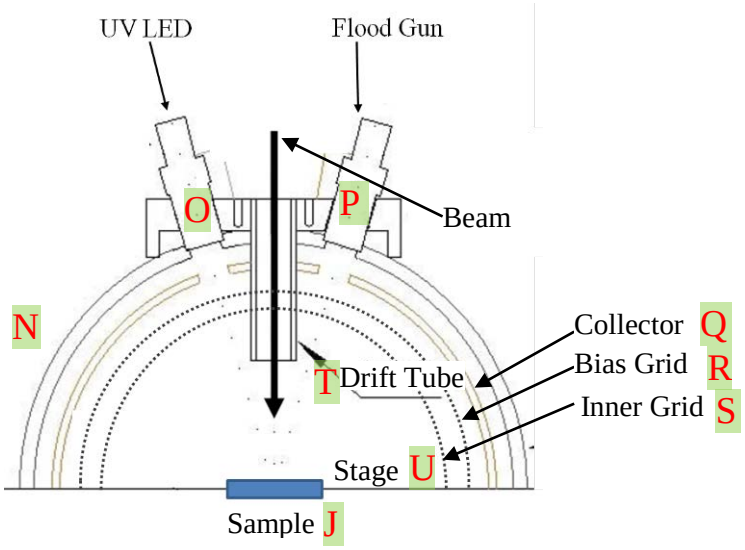

FIG. 3.2. Hemispherical-grid retarding-field analyzer.

collector (Q). Two concentric hemispherical retarding field grids allow for emitted-electron energy discrimination. The inner grid (S) is used to match the potential of the sample producing a region of zero electric field around the sample. This is meant to help keep electron trajectories from being modified by a charged sample or from emitted electrons being preferentially captured by more positive surface potentials. The outer grid (R) is then biased to a potential V_{bias} relative to the inner grid; this only allows emitted electrons with energy larger than V_{bias} to pass through to the collector and be measured.

The HGRFA was designed to almost completely enclose the sample being tested in order to capture nearly all of the emitted electrons from its surface. This allows for the direct measurement of both total incident and emitted charge with very small loss through the drift tube (T). Because the biasing grids are mostly transparent to electrons, most of the emitted electrons are measured by the collector with a small percentage depositing or scattering off of the grids and eventually depositing elsewhere (see Fig. 3.2) or being lost through one of a few openings in the HGRFA. This implies that the collector and other components have respective measurement efficiencies given by the relation

$$Q_{element} = \Gamma_{element} \cdot Q_{out}. \tag{3.1}$$

Adding the charge measured from all the HGRFA components and accounting for charge lost gives the total emitted charge

$$Q_{out} = Q_{coll} + Q_{grid} + Q_{stage} + Q_{IG} + Q_{lost} = \left(\Gamma_{coll} + \Gamma_{grid} + \Gamma_{stage} + \Gamma_{IG} + \Gamma_{lost}\right) \cdot Q_{out}$$

$$\rightarrow \Gamma_{coll} + \Gamma_{grid} + \Gamma_{stage} + \Gamma_{IG} + \Gamma_{lost} = 1. \quad (3.2)$$

The Γ_{lost} term is similar to the other efficiency terms. It is the fraction of emitted electrons that are not measured because they escape through the drift tube or through any other openings. This cannot be measured, but previous researchers have devised methods to calculate it using known angular distributions of SEs and BSEs with the geometries of the HGRFA (Nickles, 2002). Eq. 3.2 gives two methods for calculating emitted charge from measured charges: either as the sum of the individual charges accounting for lost charge, or by solving Eq. 3.1 for Q_{out} with any one of the elements. These two options give the following equations for measuring TEY

$$\sigma(E_0) = \frac{Q_{out}(E_0)}{Q_{in}} = \frac{(Q_{coll}+Q_{grid}+Q_{stage}+Q_{IG})/\Gamma_{HGRFA}}{Q_{Sample}+(Q_{coll}+Q_{grid}+Q_{stage}+Q_{IG})/\Gamma_{HGRFA}} = \frac{\cdot Q_{coll}/\Gamma_{coll}}{Q_{Sample}+(Q_{coll}+Q_{grid}+Q_{stage}+Q_{IG})/\Gamma_{HGRFA}}, \quad (3.3)$$

where $\Gamma_{HGRFA} = (1 - \Gamma_{lost})$ is the total efficiency of all the HGRFA components. For a full derivation of these equations, see Appendix G. The denominator is summed over all HGRFA elements, correcting for lost electrons, plus the sample because all incident charge either deposits in the sample or is emitted. If the sample is a conductor, then the deposited charge, Q_{Sample}, will flow from the sample through the ammeter to ground. If the sample is an insulator, then the deposited charge will cause a resulting flow of displacement current through the ammeter to the copper slug on which the sample is mounted in order to form an equivalent mirror charge. For a schematic of the HGRFA design and measurement electronics used, see Fig. 3.3.

For the efficiency method to be useful, the efficiency of the collector must be known. Methods to calculate and measure this efficiency correction factor have been developed by other researchers (Nickles, 2002). The method used to measure this collector efficiency in the past involves making TEY

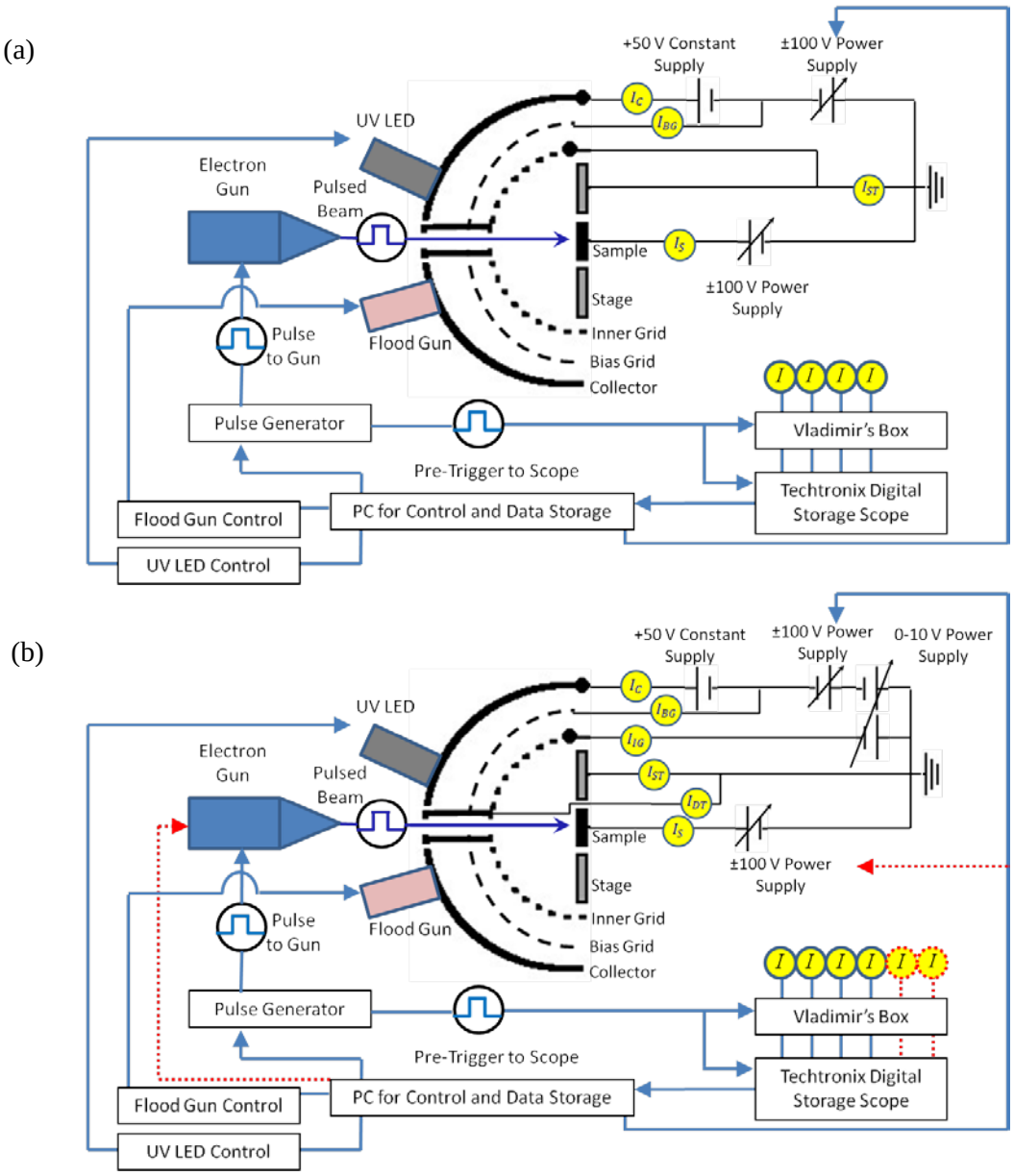

FIG. 3.3. HGRFA wiring diagrams. Block diagrams showing the various surfaces and biasing capabilities used for: (a) initial, and (b) upgraded pulsed-yield setup. Future upgrades are shown as red dashed lines.

measurements at incident energies (crossover energies, E_{cross}) where the sample current goes to zero (corresponding to a yield of 1). This gives

$$\sigma(E_{cross}) = 1 = \frac{{}^{1}/_{\Gamma_{coll}} \cdot Q_{coll}}{{}^{1}/_{\Gamma_{HGRFA}} \cdot (Q_{coll} + Q_{grid} + Q_{stage} + Q_{IG})},$$

which can be modified to give

$$\Gamma_{coll} = \frac{Q_{coll}}{{}^{1}/_{\Gamma_{HGRFA}} \cdot (Q_{coll}+Q_{grid}+Q_{stage}+Q_{IG})} \text{ at } E_{cross}. \tag{3.4}$$

This energy can be at either the first or second crossover point E_1 or E_2 (Thomson, 2005) discussed in Chapter 2. Since a yield of one corresponds to no charging, no charge should be deposited at the crossover energies leading to the sample current of zero, mentioned above. This is also why the sample charge does not appear in the denominator of Eq. (3.4).

Once this efficiency factor is known the resulting correction factor needed to convert the measured collector charge to total emitted charge is just the inverse of the efficiency. Thomson measured this correction factor to be 1.15±0.02 (Thomson, 2005), which corresponds to an efficiency of 0.87±0.02. His tests were conducted for a number of conducting materials with crossover energies ranging from 100 eV to 20 keV. This demonstrated that the HGRFA efficiency did not depend on incident energy, at least over this limited energy range. This experimental value from Thompson is in very good agreement with a theoretical value given by Nickles (2002) based on electron ray tracing.

Because of the accurate knowledge of the HGRFA's high collection efficiency, the total and backscattered yields can be measured on an absolute scale using the measured efficiency value for the collector. A collaborative effort between the USU MPG and three other international groups worked on determining a standard that could be used for this type of calibration (Dennison, *et al.*, 2016a). Further details of this study are given in Section 4.2.1.

To give a more concise definition of the two methods of measuring total electron yield and include the conversion of measured current pulses to incident charge, Eq. (3.3) can be written as σ_{eff} defined as

$$\sigma_{eff} = \frac{Q_{coll}/\Gamma_{coll}}{Q_{Sample}+Q_{HGRFA}/\Gamma_{HGRFA}} = \frac{(\int I_{coll}\, dt)/\Gamma_{coll}}{\int[I_{sample}+I_{HGRFA}/\Gamma_{HGRFA}]dt}, \tag{3.5}$$

and σ_{sum} calculated as

$$\sigma_{sum} = \frac{Q_{HGRFA}/\Gamma_{HGRFA}}{Q_{Sample}+Q_{HGRFA}/\Gamma_{HGRFA}} = \frac{\int I_{HGRFA}dt/\Gamma_{HGRFA}}{\int[I_{sample}+I_{HGRFA}/\Gamma_{HGRFA}]dt}, \tag{3.6}$$

where the integrals are over the duration of a single pulse, and the subscript $HGRFA$ denotes summing over all HGRFA components as in Eq. (3.3).

While earlier studies found that Γ_{coll} was consistent over incident energies of 100 eV – 20 keV, the extension of this study to lower energies found that the measured efficiency started to change at low energies. This was most likely due to increased beam widths at low energies, which caused SEs produced near the edge of the sample to be more likely to go under the new sample aperture (see Section 3.2.2.). Because of this, it was necessary to use Eq. 3.6 for TEY calculations. However, to make BSEY measurements, the only current used to measure the emitted charge is the collector, so Eq. 3.5 was used for these calculations using an efficiency factor (0.71) calculated by previous researchers using the measured angular distribution of BSEs, which determined the fraction of BSEs that escape through the beam drift tube (T), or scatter off the collector and grids (Nickles, 2002).

3.1.4.2. Energy Discrimination

The use of hemispherical grids to produce retarding fields produces forces, which are radially aligned with the sample and either parallel or anti-parallel to the emitted electron trajectories. The fact that the electron trajectories are, at least approximately, aligned with these radial retarding fields, allows measurement of the total electron energies; whereas, the use of flat grids would only measure the vertical component of the electrons' kinetic energies. The above argument, however, hinges on the assumption that all emitted electrons originate from a point source at the exact center of the HGRFA and that grids are perfectly hemispherical or concentric. The errors associated with these two assumptions produce a limit to the energy resolution of the HGRFA (Nickles, 2002).

An example of how this can be used follows. By biasing the bias grid to 10 V relative to the inner grid, all electrons with emitted kinetic energies less than 10 eV will be repelled by the bias grid once they reach the region between the inner grid and the bias grid. The only electrons that will make it through to the collector are those with emitted energies higher than 10 eV.

Once the electrons get through the bias grid and hit the collector, they can produce more SEs or BSEs through interactions with the collector surface. This has the potential to produce contaminating currents in the HGRFA. To minimize this problem, the collector is coated with Aquadag®, a disordered

graphite coating with a very low electron yield, to reduce the number of BSEs emitted from the collector. The collector is also biased to +50 V relative to the bias grid, so all secondaries (defined as emitted electrons with energy <50 eV) emitted by the collector will be reattracted by the collector. Therefore, the only electrons that can leave the collector are high-energy BSEs. Since the BSEY of Aquadag® is extremely low ($\eta \leq 0.2$ for $E_0 > 200\ eV$ and $\eta \leq 0.3$ for $50\ eV < E_0 < 200\ eV$) (Dennison, *et al.*, 2001), this produces very little loss from the collector.

Because backscattered electrons have been operationally defined as electrons with energies above 50 eV, the backscattered yield can be measured by biasing the bias grid to -50 V. This also allows for secondary electron yield to be measured by subtracting the backscattered yield from the total yield. Similarly, by doing a series of measurements with increasing grid biases, the energy distribution of emitted electrons can be found by taking the derivative of the collector current versus bias energy curve.

3.1.4.3. Neutralization

If the sample being tested is an insulator, there are a few ways that charging can affect the measured yield values (see Fig. 3.4). If the sample charges positively ($\sigma > 1$), low-energy secondary electrons will be reattracted to the positively charged sample and will not reach the collector (see Fig. 1.2 and Fig. 2.7). This will result in a drop in the measured total and secondary yields, as illustrated in the positive charging region of Fig. 3.4 by the difference between measured TEY and SEY and the predicted

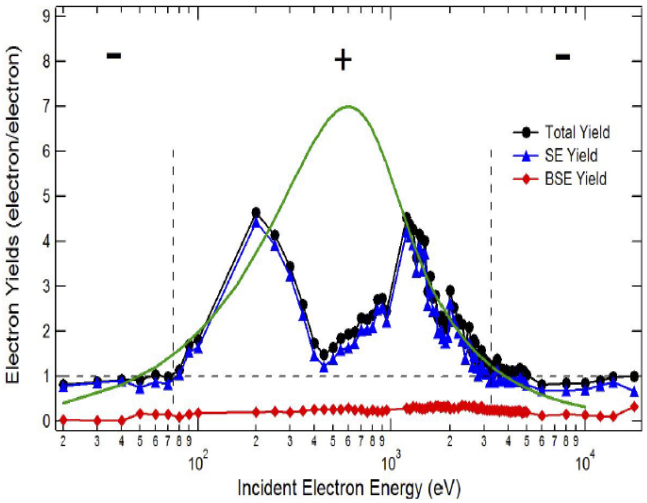

FIG. 3.4. Charging effects in yield curves of high-yield, low-conductivity Al_2O_3. Measurements by Hoffmann (Hoffmann, 2010).

intrinsic yield curve shown in green (Hoffmann, 2010). This positive charge will also accelerate the incident electrons, which are coming toward the sample, giving them a larger landing energy than they started with as they left the electron gun. This is most significant at low incident energies when the resulting percent error in PE landing energy due to sample biasing is the greatest. Both of these effects will produce yield measurements that are not correct and trend away from the true value towards $\sigma = 1$.

Similarly, if the sample charges negatively ($\sigma < 1$), incident electrons will be slowed down by the sample causing either a reduced landing energy leading to a yield of 1 for $E_0 > E_2$, or in extreme cases, completely repelling incident electrons (for $E_0 < E_1$).

Another adverse effect of negative charging appears in the measurement of BSEY. If the sample is charged negatively to about -50 V or more, then emitted low-energy secondaries will be repelled by the negatively charged sample reaching the inner grid with energies greater than 50 eV, and this added energy will allow them to get through a -50 V biased retarding grid, thereby being counted as BSEY (see Fig. 3.5). Therefore, in order to obtain correct BSEY measurements, the sample cannot be charged negatively (Hoffmann, 2010).

Another way to see this effect of sample charging is in the effect it has on the emission energy spectra. While a negative bias slows down the incident PEs, they are accelerated back to their initial energy as they leave the sample resulting in negligible change in the BSE contribution to the emitted electron energy distribution. However, because SEs originate within the sample, they are accelerated as they go from the sample to the grounded inner grid resulting in a shift of the SE emission peak. This shift will be toward higher emission energies for negatively biased samples and toward lower emission energies for positively biased samples (see Section 4.2.6). Therefore, if the sample is biased to -50 V or more, all secondary electrons will be shifted above the designated 50 V cutoff so that $\delta \to 0$, and the BSEY measurement will be equal to the TEY. High-energy yields in Fig. 3.5 show an abrupt increase in BSEY and decrease in SEY with no change in TEY above E_2 due to a sample charged negatively to $\leq 50\,V$.

Efforts made by Hoffmann greatly improved capabilities of insulator TEY measurements; however, positive charging still occurred at very high yields, and the UV LED used did not have enough energy for negative charge neutralization. To expand upon his work and overcome both negative and

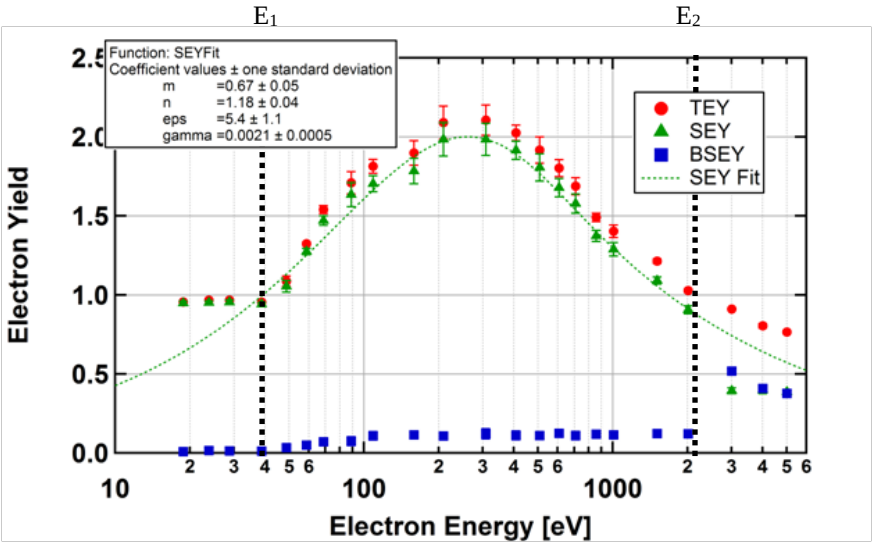

FIG. 3.5. Yield of quartz with BSEY modification at high energies, $E_0 > E_2$, and SEY/TEY at low energies, $E_0 < E_1$.

positive charging caused by the process of making yield measurements, methods using small pulsed-beam measurements have been made to minimize deposited charge, while charge neutralization methods have been improved upon to remove stored charge between pulsed measurements. A low-energy electron flood gun attached to the HGRFA is used to neutralize positive charge by depositing low-energy electrons onto the surface of the material. To neutralize negative charge, a high-energy UV LED is also attached to the HGRFA to dissipate negative charge from the sample via the photoelectric effect and RIC.

3.1.5. Electronics

As was seen in Fig. 3.3, the need for multiple simultaneous current measurements along with different voltage biases on various elements of the HGRFA has resulted in a very elaborate electronics setup for current measurements and biasing of the various detector elements. The main principle behind each current measurement is simple, however. To measure the current deposited in one element of the HGRFA, a floating ammeter is placed in series with that element before any connections are made between that element and another element. Most commercially available picoammeters have slower response times than our application requires; they also require current measurements straight to ground. Because the elements require variable biasing relative to one another, our application requires faster measurements, as well as the ability to float the potential of the picoammeters. The ammeters used (Thomson, *et al.*, 2003)

use optically isolated operational amplifiers to boost the response time and lower the noise in measured currents. These picoammeters have an adjustable gain between $2\times10^{6}\ V/A$ and $1\times10^{8}\ V/A$, and a rise time, increasing with increasing gain, of about 1-8 μs.

3.1.6. Software

A LabView VI (Yield Pulse v4.vi) is used to run the data collection process, which controls the sequencing and duration of beam pulsing, current measurements, and charge neutralization. This program was also designed to do preliminary integration analysis of the data to determine the total integrated charge for each oscilloscope current trace ($I_{coll}, I_{sample}, I_{grid}, I_{stage}$), and average yield of each pulse (see Appendix D). A similar program was also written to do DC electron spectra measurements (DC Spectra.vi). Details of the older data acquisition VIs are given in Nickles' Appendix D (Nickles, 2002).

3.2. Improvements

While the methods discussed above have proven to be very successful (Hoffmann, 2010), there were still some problems. Most of the problems had to do with inadequate charge neutralization from both the electron flood gun and UV LED for extremely high-yield, low-conductivity materials (see Fig. 3.4). Some of the other problems related to noise reduction, bad electrical connections or shorts, data analysis, and inner grid biasing. Section 3.2 describes specific problems identified, instrumentation and software enhancements developed to resolve them, and measurements designed to validate and quantify these improvements. Upgrades, their predicted effects, and tests to validate and quantify these effects are given in Table 3.2.

3.2.1. Charge Neutralization

Both charge neutralization methods have been recently improved as new technologies produced electron sources with lower work functions, as well as UV LEDS with higher-energy and higher-intensities (see Fig. 3.6).

The previous design of the electron flood gun had problems with frequently broken or shorted electrical connections. It was also very difficult to assemble the gun without breaking the expensive electron source filament. The design was modified to reduce strain and wear on the wires, as well as

Table 3.2. Planned improvements to electron emission measurements of insulators.

Relevent Sections	Initial Capabilities	Improved Capabilities	Predicted Effects of Improvement	Tests for Validation and Quantification of Improvements
4.3.3	Use ~5 μs pulses	Use <3 μs pulses.	Yields for <60% of previous incident charge and optimal pulse shape.	Measure length of pulse. Test whether conductors give the same results for different length pulses.
4.2.4 4.2.5 4.2.6	Grounded inner grid	Variable bias inner grid, with bias grid and collector floating on the inner grid bias.	Improved detection for high surface potentials.	Bias Au to simulate charged sample and test the effectiveness of the inner grid biasing. Compare full energy spectra for different bias settings. Do multiple tests of insulators with different biasing and compare to get best results.
3.3.2	Flood gun and UV driver circuit share ground with HGRFA	Externally grounded flood gun and UV driver circuit to reduce noise.	Signal-to-noise ratio reduced two to five times.	Measure the signal-to-noise ratio in oscilloscope data and compare to previous data.
4.3	UV LED (low intensity, ~290 nm)	UV LED (high intensity, ~255 nm).	Improved negative charge neutralization.	Do yield measurements with and without UV flooding and use different flooding time intervals to see what time interval is needed to neutralize accumulated charge.
4.3	Tungsten flood gun filament	Tantalum disk flood gun filament.	Improved positive charge neutralization. More stable emission current for lower noise and incident energies.	Measure flood gun emission current with Faraday cup and quantify flux density with different gun settings. Show stability at lower energies by acquiring yields at energies down to 10-20 eV.
4.3.3	Integrated charge calculation of yields	Point-wise yield calculations.	Yields for <5% of total incident charge.	Use point-wise yield method to observe intrinsic yield plateau and other features predicted by the charge model. Point-wise yield measurements of Au should show no charging and agree with pulsed and DC values. Do two tests: one with a longer pulse and one with a higher beam current to verify we are getting the same results per incident charge. Also compare these tests to results of several consecutive smaller pulse tests.
5.2.1	Labview data collection VI	Improved Labview VI including point-wise yield data, and enhanced flood gun control and grid biasing.	Computer control of improvements.	Compare to previous data collection methods to verify similar results.

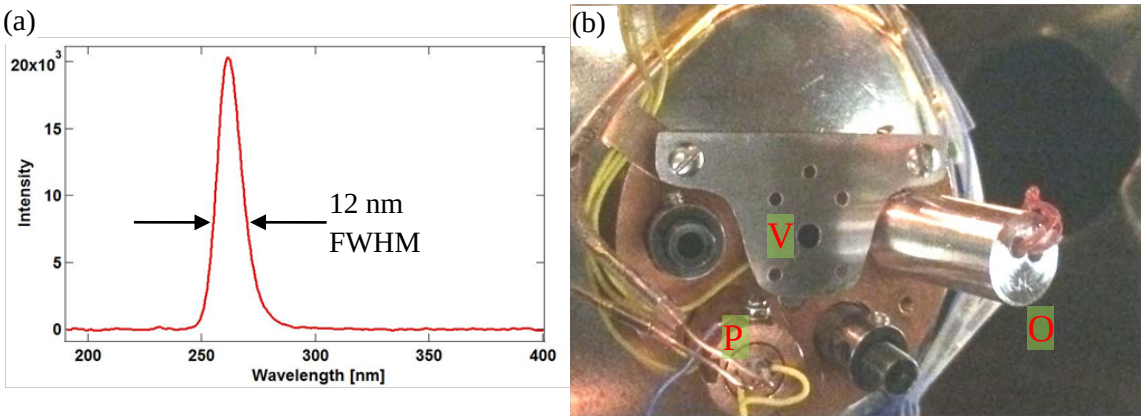

FIG. 3.6. UV LED and flood gun upgrades. (a) Emission spectra of the UV LED peaking at ~255 nm and spanning ~ 250-275 nm. (b) Modifications made to the HGRFA. These include changes to the electron flood gun (P), UV LED (O), and beam aperture (V).

decrease the chances of damaging the filament. The flood gun hairpin W filament was switched to a tantalum disk filament for better durability. New settings were determined for optimal functionality of the flood gun (see Appendix B for details of flood gun upgrades and new settings).

To validate that the floodgun is working, the HGRFA is put over a Faraday cup on the sample carousel and emitted current is measured using DC picoammeters in the yellow patch panel. It is currently extremely difficult, if not impossible, to measure the coverage of the flood gun because we cannot currently scan a Faraday cup through the beam. Future work will make this possible by adding a movable FC to the inside of the HGRFA to do these types of measurements.

The new UV LEDs used were made by Sensor Electronic Technologies, Inc. (SETi.) They produce an emission spectrum with a peak wavelength of ~255 nm or 4.86 eV and a ~12 nm FWHM (see Fig. 3.6(a)) The manufacturers QC inspection report for these LEDs showed a maximum optical output of 480 µW ±10% and an emission angle of 120°.

In order to incorporate these new UV LEDs into our system, the controlled current output from the commercial LED driver (SETi, model) was sent through a relay (International Rectifier, PVR1300N) switched on and off using a computer TTL signal controlled by the LabView VI. The same TTL signal is wired to both the flood gun and LED relays (see Appendix E). When this was first developed, the LED relay drew too much current, which did not allow the TTL voltage from the DAQ card (National Instruments, BNC 2110) to rise high enough to actuate the flood gun relay. To remedy this, a potentiometer

was wired in series with the LED relay and adjusted so that the flood gun relay could get the correct voltage (see Appendix E). In the future, it would be a good idea to use separate TTL signals from the DAQ card to control the UV LED and flood gun independently.

The UV LEDs also stopped functioning quite regularly, which proved to be an expensive problem since each LED cost about $350. After consulting with the manufacturer, it was determined that these failures were most likely caused by electrostatic discharge (ESD) from nearby charged insulators in the chamber, or from insufficient ESD-safe handling.

To remedy these problems, a few changes were made to the power supply, as well as the LED mount on the HGRFA. The first modification added two Zener diodes across the outgoing leads of the LED driver box (see Appendix E). The Zener diodes act like large resistors unless the voltage rises above their voltage rating (30 V) in which case their resistance drops dramatically letting current flow. This acts like a reusable fuse protecting the LED from large voltage spikes. A floating BNC connection was also added to allow for current monitoring of LED. The second UV LED modification was to build a special mount for the LED, which completely shielded it from stray electrons in the chamber (see Fig. 3.6(b)). This was also designed to act like a quick connect making LED replacement very simple.

To minimize the chance of charging and arcing through the LEDs, special precautions were taken to protect them. First, when handling them, special ESD-safe gloves were worn and wrist grounding straps used to prevent static buildup on the handler. The leads of the LED are always shorted using a grounded wire with clips on each end until it is connected appropriately to the HGRFA. Lastly, even when the HGRFA is installed in the chamber, the LED feedthrough pins are shorted using a wire. Subsequent work has replaced this wire with a grounding switch (see Appendix E). To test that the UV LED is working, the grounding wire is removed from the vacuum feed through pins, a +5 V signal is sent into the UV LED relay connection, and the LED driver box is switched on. By turning off the room lights and rotating the sample carousel so that the HGRFA faces one of the chamber port windows, a purple light is visible looking down the beam drift tube. To make it more visible it is a good idea to put the HGRFA over a white, or reflective sample. With these modifications, we have now run over a year without destroying an LED.

The AC/DC power supply that came with the LED driver and was initially installed as part of the system was found to add noise to the yield measurements through electromagnetic induction. This was removed and replaced with a 12 V 7.2A-hr rechargeable battery supply (Belkin, BU3DC001-12V) to remove alternating noise contamination.

3.2.2. Beam Aperture

There was some concern that, because of the small distance between the pulsed electron gun and the HGRFA, the electron beam might not be adequately collimated. This could cause the incident beam to hit the drift tube, producing secondary electrons, and causing error in the measured yield values. Similar problems with beam focusing have been encountered by other researchers at low beam energies (Andronov, *et al.*, 2013). To fix this problem, a special 3 mm aperture was designed to sit over the opening of the drift tube (~7 mm inner diameter) and cut the beam size down (Fig. 3.6(b)). This addition was expected to make it easier to find appropriate electron gun settings for each beam energy, because the beam would not need to be focused as tightly. This would also make it possible to produce a very uniform current flux density in the part of the beam that was passed through the aperture and incident on the sample being tested. In addition to this modification, the drift tube was electrically insulated from the rest of the HGRFA and a wire was connected to it so that any current incident on the beam drift tube could be measured externally.

3.2.3. Sample Aperture

There were repeated problems with the sample carousel shorting to ground making the stage current measurement impossible. To overcome this problem, a plate with an aperture (~1 cm diameter) to allow the beam to hit the sample was added to the HGRFA to replace the function of the stage. This plate was machined and installed in the HGRFA so it would sit as close to flush with the surface of the sample (~1 mm) as possible without touching it or shorting to the carousel. This was necessary because any gap between it and the sample poses a threat for SEs to hit the plate and not reach the collector. Assuming that all emitted electrons from the sample originate at a point source in the center of the sample, this limits the emission angles that reach the collector to ~79 degrees off of the surface normal vector. The sample aperture was also coated in Aquadag® to make it as absorbent as possible to electrons. Assuming a cosine

distribution for SEs, the fraction of SEs that are cut off by this plate is 3.8%. BSEs, however, are much more tightly emitted so almost none are cut off. To mount this plate, it was sandwiched between the inner grid and the stage using insulating spacers to keep it electrically isolated. Finally, a designated wire was attached allowing for the external measurement of the current deposited in the sample aperture. This current replaced the previous current, which was used for the stage. As discussed in Section 4.2.5, this stage plate can and should be biased along with the inner grid to match the sample surface potential. By doing this, the region between the sample and inner grid will have no electric fields and emitted electrons will travel in straight radial trajectories away from the sample.

3.2.4. Inner Grid Bias

In an attempt to improve measurement capabilities for beam energies where positive charging occurred, the electronics for the inner grid were modified so it could be biased positively or negatively to match the potential of the charged sample. Because the sample potential is difficult to measure, a variable voltage battery pack has been designed, which allows for the inner grid to be biased relative to the stage with up to seven rechargeable AA batteries (~ +9.8 V). Future work should add capabilities for negative biasing. This was done in order to hopefully produce a region of zero electric field around the sample to keep low-energy secondary electrons from being reattracted to the charged sample. A second battery pack also puts an equivalent voltage bias on the inner shielding of the triaxial cables to keep small, but measureable, currents from flowing between the signal wires and the shield wires. These modifications made to the inner-grid wiring are also beneficial because they allow for the separate measurement of the inner grid, and sample aperture (stage) currents for troubleshooting purposes.

3.2.5. Noise Reduction

Bad wiring connections and ground loops were found on a few of the electrical connections to the HGRFA. The most notable of these was a short between the grounded electron gun shell and the HGRFA, which caused a lot of 60 Hz noise in the stage and saturated our signal. There was also a connection between the grounded braided ribbon cable and the HGRFA where the two were connected. To fix these,

the flood gun was isolated from the HGRFA using Kapton tape and the braided ribbon cable shielding was cut and pulled back away from the HGRFA (see Fig. 3.7).

Also, as is mentioned in Section 3.2.1 above, noise from the DC power supply caused 60 Hz noise in the yield measurements. Replacing this power supply with a 12 V DC battery supply fixed the problem. However, if the battery supply is plugged in and charging during measurements, it still introduces noise into the measurements through its AC connection. Therefore, it should be unplugged as part of the experiment setup procedures.

3.2.6. Pulse Width

To reduce the amount of charging that occurred per pulse, the pulse width was reduced from 5 to 3 μs; however, the cabling and current amplifier circuitry seems to have some inductive/capacitive resonance evident by overshoot and ringing in the oscilloscope traces, which gives a minimum measureable peak width of about 3 μs to 4 μs. See Section 5.2.1 for future work on this subject.

3.3. Analysis Methods

Various programs and analysis techniques are used to extract information from the collected data. Previous work developed techniques to analyze DC and pulsed yield data (Thomson, 2005; Hoffmann, 2010). All methods have the goal of determining the amount of charge incident and emitted from the sample, in order to find the yield as described by Eq. (2.1).

3.3.1. DC Yield Method

The analysis necessary to calculate DC yield is probably the most simple to do (Nickles, 2002). Because conductors discharge so quickly (near the speed of light) as long as they are connected to ground, they can be approximated as uncharged (unless a specific sample bias is applied) (Thomson, 2005; Hoffmann, 2010). All of the surfaces in the HGRFA collect a steady current, which can be measured over relatively long times to enhance the signal-to-noise ratio. Because current is just charge per unit time, all of the currents are proportional to the amount of charge being measured. Therefore, the charges in Eq. (2.1) can be replaced by the measured current, which effectively provide a time-averaged charge over extended

time periods (that is, 1 sec instead of 5 μs). Also, since charge moves freely, there is no displacement current for conductors. For DC yield measurements,

$$\sigma_{DC} = \frac{I_{out}}{I_{in}} = \frac{(I_{coll}+I_{stage}+I_{grid})/\Gamma_{HGRFA}}{(I_{coll}+I_{stage}+I_{grid})/\Gamma_{HGRFA}+I_{sample}} = 1 - \frac{I_{sample}}{(I_{coll}+I_{stage}+I_{grid})/\Gamma_{HGRFA}+I_{sample}}. \quad (3.7)$$

3.3.2. Integrated Pulsed Method

To analyze the measured data, the current versus time traces measured with the fast current amplifiers and digital storage scope (see Fig. 3.7) are integrated from the beginning (t_i) to the end (t_f) of the pulse to determine the amount of total charge per pulse.

$$\sigma_{pulsed} = \frac{\int_{t_i}^{t_f} I_{out}\,dt}{\int_{t_i}^{t_f} I_{in}\,dt} = \frac{\left(\int_{t_i}^{t_f}(I_{coll}+I_{stage}+I_{grid})\,dt\right)/\Gamma_{HGRFA}}{\int_{t_i}^{t_f}([I_{coll}+I_{stage}+I_{grid}]/\Gamma_{HGRFA}+I_{sample})dt}$$

$$= 1 - \frac{\int_{t_i}^{t_f} I_{sample}\,dt}{\int_{t_i}^{t_f}([I_{coll}+I_{stage}+I_{grid}]/\Gamma_{HGRFA}+I_{sample})dt}. \quad (3.8)$$

However, this only works if the currents in the oscilloscope traces are correctly zeroed before the integration takes place. Previous analysis methods did an averaging of oscilloscope current data before and after the pulse in order to remove a constant baseline current from the data before analysis. New techniques allow the user to also do a linear background subtraction plus a sine fit to remove oscillating background

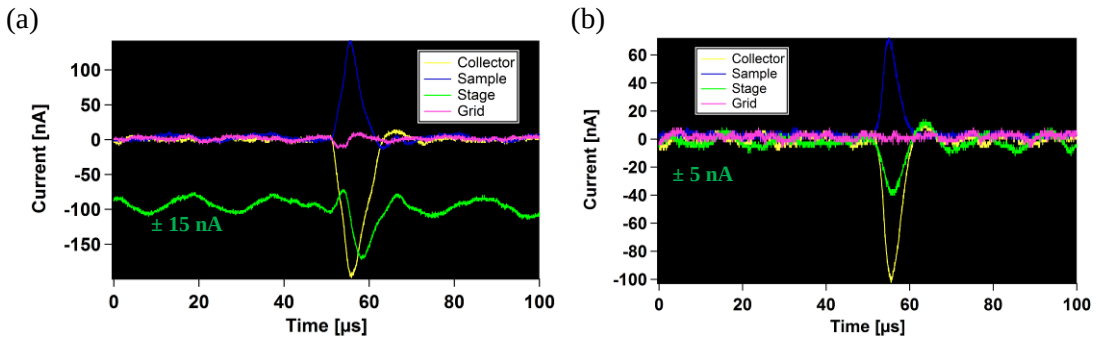

FIG. 3.7. Sample oscilloscope traces of pulsed current data. Oscilloscope traces of Au at 200 eV incident energy. Data were taken before (a) (2015), and after (b) (2017) improvements to the system. In good pulse data, the regions before and after the pulses are flat. One problem, which has not been fully resolved, is the ringing that occurs when the signal should drop back to zero. This ringing is largest in the stage signal.

current from the collected data (see Fig. 3.8). By doing this, the curves are adjusted so that the data before and after the pulse are closer to zero (see Fig. 3.8).

3.3.3. Point-wise Pulsed Method

The point-wise analysis method was developed to see how the measured yield values changed throughout the course of a single pulse. This point-wise pulsed method effectively conducts a set of N_p successive yield measurements without charge neutralization. The upper bound of N_p is set by the number of oscilloscope readings taken during a single pulse. For a 4 μs pulse, with oscilloscope data taken at 0.04 μs intervals, this upper bound on N_p is 100 measurements. A more realistic set of measurements uses currents smoothed using a moving boxcar average over ~5 oscilloscope readings, such that $\overline{N_p} \sim 20$ measurements. This technique is similar to the DC yield method in the fact that it used the average current values to calculate the yield at each oscilloscope point (or set of points) in the pulsed yield data. The yield calculation for this method has the form

$$\sigma_{pt-wise}(t) = \frac{\overline{I_{out}}(t)}{\overline{I_{in}}(t)} = \frac{\left(\overline{I_{coll}}(t)+\overline{I_{stage}}(t)+\overline{I_{grid}}(t)\right)/\Gamma_{HGRFA}}{\left(\overline{I_{coll}}(t)+\overline{I_{stage}}(t)+\overline{I_{grid}}(t)\right)/\Gamma_{HGRFA}+\overline{I_{sample}}(t)}$$

$$= 1 - \frac{\overline{I_{sample}}(t)}{\left(\overline{I_{coll}}(t)+\overline{I_{stage}}(t)+\overline{I_{grid}}(t)\right)/\Gamma_{HGRFA}+\overline{I_{sample}}(t)}, \tag{3.9}$$

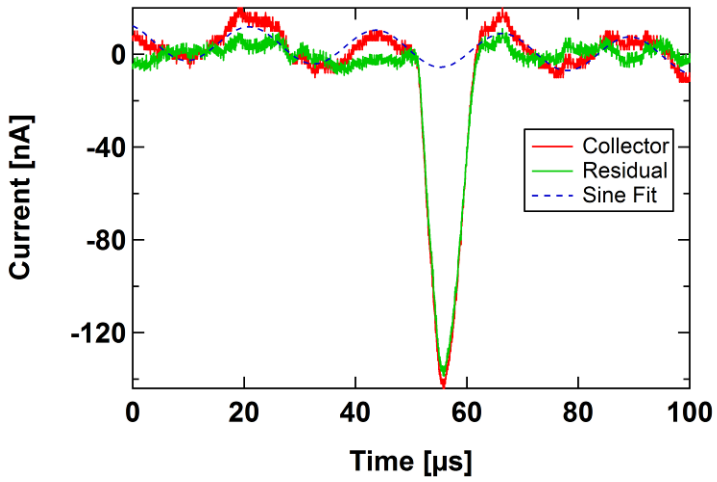

FIG. 3.8. Typical example of oscillating noise removal. An example of the sine fit (blue dashed) that is performed to remove oscillating noise from the measured signals (red). This decreases the noise level in the final curve (green) by a factor of ~2 to 3.

where the currents $\bar{I}$ are moving boxcar averages over neighboring oscilloscope measurements.

In order for this method to work, there needs to be high confidence that all of the noise has been removed from the data and that the data being analyzed reflect the true currents at each point in time. Figure 3.9 shows both the pulsed current traces, as well as the calculated point-wise yield trace. Note the drift in the point-wise yield over the course of the pulse. Such a drift is what would be expected if charging were occurring. If no charging is occurring, a constant trace should be seen over the pulse interval. In regions to the left and right of the pulse, the signal-to-noise ratio becomes large, which causes the error in the point-wise yield method to become very large. This can be understood better by considering the case where incident charge approaches zero and emitted charge is nonzero. This will cause the point-wise method to have an asymptote at this point, as indicated in Fig. 3.9 by the vertical lines.

To understand the value of this point-wise, pulsed method, consider the integrated charge used for the method. For a typical integrated pulse method measured prior to this thesis work, pulses were ~ 5 μs in duration with average current of 100 nA during the pulse and total incident charge of 500 fC or 3.1×10^6 electrons per pulse. This current was incident over ~ 2.3 mm^2 area, providing ~217 fC/mm^2 or ~ 1.36×

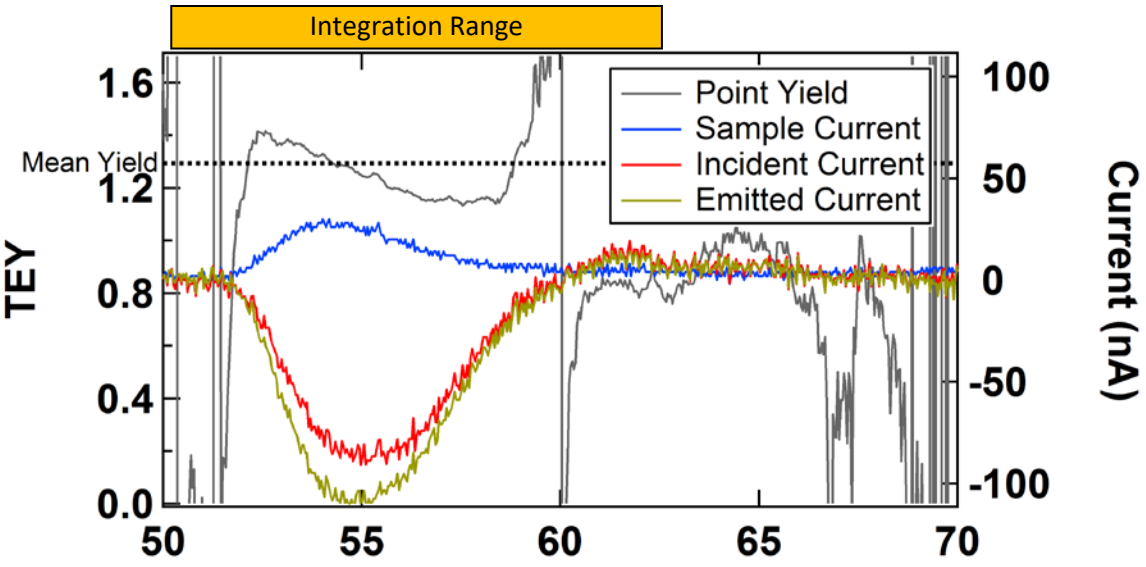

FIG. 3.9. Point-wise yield method. Point-wise yield (gray) of gold is shown along with incident (red), emitted (yellow), and deposited sample (blue) current pulses. The horizontal dashed line shows the average yield calculated by integrating incident and emitted charges over the range specified.

$10^6\ e^-/mm^2$ per pulse. After improvements to the integrated pulsed method detailed in this thesis, typical pulses were 3 μs in duration at currents of 100 nA during the pulse. Average beam width covered ~$12\ mm^2$with total incident charge of 300 fC or 2×10^6 electrons per pulse and total incident charge densities of 23.9 fC/mm^2 or $1.5\times10^5\ e^-/mm^2$ per pulse. The amount of charge per measurement after the thesis improvements was ~ 60 % of that prior to the thesis improvements.

3.4. Validation Tests

To validate and quantify the improvements that were made for this work, a series of tests were planned (see Table 3.2). Some of the tests were not performed because they were either deemed not necessary or replaced with more useful tests. Actual tests performed are found in Chapter 4, along with their results, and a summary table of these results is given in Chapter 5.

CHAPTER 4

INSTRUMENTATION CHARACTARIZATION AND VALIDATION

In this chapter, the tests used to quantify improvements and validate changes are explained and the results of these tests are presented. This includes tests to characterize the incident electron beam, demonstrate the effectiveness of neutralization methods, quantify noise levels, characterize biasing effects, improve analysis methods, and extend to lower energy yield measurements.

4.1. Beam Characterization

In order to ensure that the only variable from one yield measurements to the next is beam energy, it would be ideal to have identical beam fluxes and shapes for all beam energies. However, difficulties were encountered at low energies where the beam was too wide and at high energies where the beam was too narrow (see Fig. 4.1). These result from the limits of focusing capabilities of the electron gun used. Since high-yield values amplify the measured currents and have the potential to saturate the ammeters, smaller incident currents were needed for high-yield energies; however, larger incident currents were needed to get good measurements for low-yield energies. Because of these facts, we were not able to find one beam width and current density that worked for all energy measurements. This was assumed to be acceptable in our situation, because yield only deals with the ratios of incident and emitted charge and not with incident current. There can be small effects on yield due to enhanced charging rates of insulators for higher beam current densities. This can be partially offset by increased radiation-induced conductivity effects at the higher beam current densities. Hoffmann took a different approach, trying to find settings that produced uniform beam current densities over a more limited range of incident energies (Hoffmann, 2010).

4.1.1. Beam Shape

To measure the beam flux distribution, a Faraday cup (FC) was scanned through the beam and the measured current versus FC position traces were recorded. These tests had some difficulties, however, because the STAIB electron gun being used was designed to work at energies from 100-5000 eV and produce beams with widths from (10^{-6} to 10^{-3} m). Since energies down to 10 eV and widths of ~5 mm were desired, this was difficult. Also, since the FC had a diameter of 5 mm and the beam shape was a 2D

Gaussian, perfect deconvolution of the signals was not readily performed. Using the ideas of convolution did, however, give some information about the beam shape. The measured current in the FC positioned at position *s* can be approximated by a one dimensional convolution using

$$M(s) = \int_{-\infty}^{\infty} f(z) * U(z-s)dz, \tag{4.1}$$

where f(z) is the actual beam shape, and *U*(*z*-*s*) is a boxcar function that describes the measurement response of the FC centered at position *s*. A more accurate method would be to use a two-dimensional beam profile, and response curve; however, if the beam or FC is much smaller than the other, the one dimensional approximation is valid. Figure 4.1 shows the results and trend of narrower beam with higher energies. By reducing the problem of convolution to one dimension and assuming that the FC has a square response curve, the measured beam profiles for various width Gaussian distributions can be calculated, as shown in Fig. 4.1(c). By performing the convolution described above the measured data were analyzed and

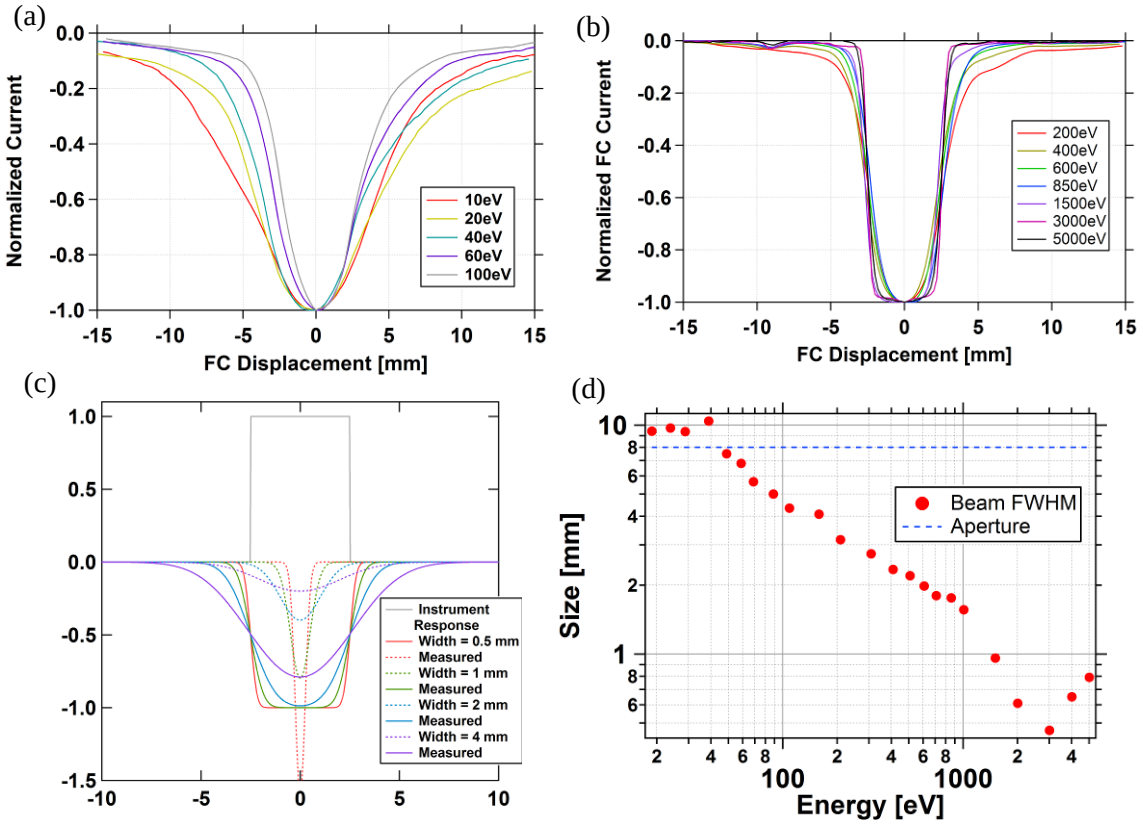

FIG. 4.1. Staib gun beam profiles. (a, b) Beam profiles are shown for different beam energies. (c) Convolution model of expected beam profiles for Gaussian beams of varying widths. (d) Beam width results from 1D convolution fitting of data. Energies are adjusted to correct values (see Section 4.1.2). The projected diameter of the beam aperture is also included for comparison (blue dashed line).

beam widths were estimated (see Fig. 4.1(d)).

A more physically correct convolution would consider a 2D Gaussian beam convolved with a circular FC response function. Using the same function names as in Eq. (4.1), this gives

$$f(x,y) = {}^{A}/_{2\pi \cdot \sigma_{width}}\, e^{-\frac{(x^2+y^2)}{2\sigma_{width}^2}}, \tag{4.2}$$

$$U(x,y) = \begin{cases} 1, if\ x^2 + y^2 < r^2 \\ 0\ \ otherwise \end{cases}, \tag{4.3}$$

$$M(s) = \int_{-\infty}^{\infty} \int_{-\infty}^{\infty} f(x,y) * U(x, y-s) dx\, dy, \tag{4.4}$$

where *r* is the radius of the FC. This should give results similar to Eq. (4.1) when the beam is much smaller or larger than the FC. However, when the two are of similar size there will be modest differences due to the rounded edge of the FC. To quantify the effect of using the 2D method versus the 1D method, 1D convolution fits were done to 2D convolutions of varying beam widths (see Fig. 4.2). The $\sigma_{width} = 0.25$ tests showed very good agreement while the $\sigma_{width} = 4.5$ test showed agreement within ~1.3%, which is also sufficient. Therefore, the 1D convolution fits can be done to get values within ~2 %, as long as the FC diameter is held constant at the correct value.

4.1.2. Beam Energy

The power supply for the Staib Instruments electron gun used in these tests displays the beam energy down to 10 eV increments, with uncertainty of ±5 eV. In order to get more precise measurements of the accelerating potential supplied to the gun, the power supply was modified to have an output BNC, which could be used to measure this voltage. A multimeter was added in order to improve the voltage sensitivity to ±0.5 eV. To validate the beam energies at these low accelerator voltages, tests were done to measure the emission spectra at low incident energies. By determining the location of the backscattered electron peak, the beam energies could be verified and the distribution could be quantified.

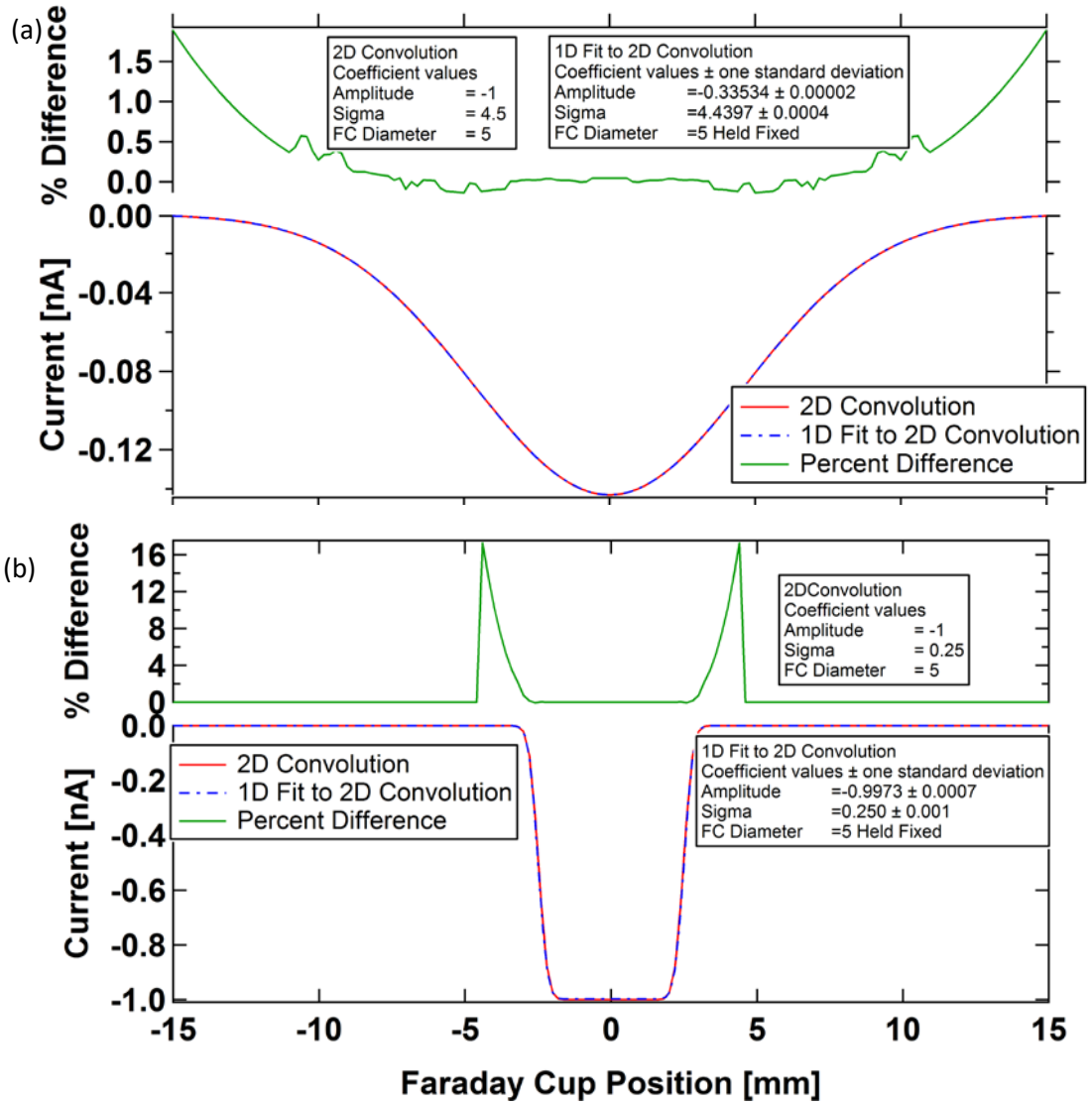

FIG. 4.2. 1D/2D beam profile convolution comparison. 1D convolution fits were done on simulated 2D convolutions of (a) $\sigma_{width} = 4.5$, and (b) 0.25 Gaussian beams. The two models showed good agreement (0.4%) of beam width for small beams (b), and slightly worse (1.3%) for the wider beam.

Figure 4.3 shows the results of these tests for Au. Note the discrepancy between the location of the high-energy BSE peak (71 eV) and the expected beam energy (60 eV). A similar energy offset effect was seen for all distributions (see Table 4.1). The two curves were taken using different gun settings. The pulsed spectra were taken using the same pulse settings as were used for pulsed yield measurements in this thesis. To mimic a DC signal, the pulse generator was put in gated mode, which sends out pulses at a steady rate determined by the Period setting on the pulse generator. This is seen by the DC ammeters as a DC current and can be used the same way. The DC curve was taken by stopping the pulse generator and turning

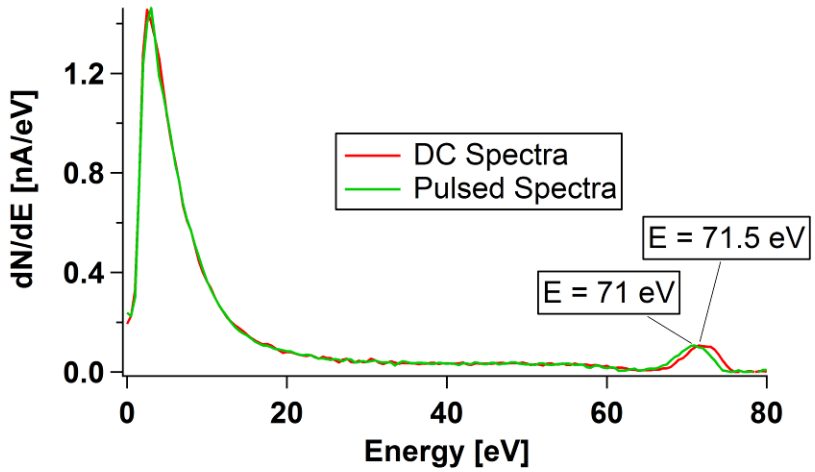

FIG. 4.3. Au energy spectra for 60 eV incident energy. Note the ~11 eV systematic error in incident energy.

the Grid setting down on the Staib gun supply box until the gun started to emit current, which could be seen in the ammeters. Both of these curves were performed starting with the same initial current measurement, which produced peaks of almost identical size.

Table 4.1 gives the results of Gaussian peak fits to the measured backscattered peaks. These results are also displayed in Fig. 4.4. The linear fit shown in Fig. 4.4(a) shows an extremely linear behavior with a reduced chi squared value of 0.45. While current biasing capabilities only allow us to measure spectra up to ~100 eV, this fit suggests that the offset of 8.8±0.3 eV might reasonably be extended up to higher energies. This offset has been applied to all curves in the thesis, except where noted.

Table 4.1. Staib gun measured elastic peak for $E = 10 \rightarrow 80\ eV$.

Displayed Energy [eV]	BSE Peak Energy [eV]	Offset [eV]	FWHM [eV]
10.0±0.5	18.54±0.04	8.54±0.5	3.03±0.09
15.0±0.5	24.38±0.02	9.38±0.5	2.80±0.06
20.0±0.5	29.84±0.02	9.84±0.5	3.22±0.06
30.0±0.5	39.46±0.03	9.46±0.5	3.96±0.08
40.0±0.5	49.59±0.06	9.59±0.5	4.1±0.2
50.0±0.5	60.0±0.2	10±0.5	3.5±0.5
60.0±0.5	70.9±0.2	10.9±0.5	3.5±0.6
80.0±0.5	90.4±0.5	10.4±0.7	4±1
Average		9.8±0.7	3.5±0.5

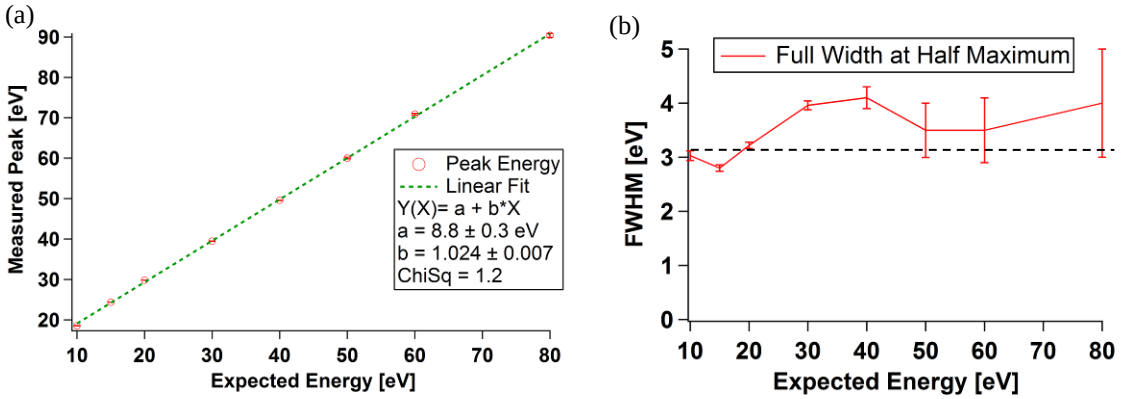

FIG. 4.4. Results of Gaussian fits to BSE peaks. (a) Measured BSE peak energy versus metered Staib gun energy. (b) Full width at half maximum of Gaussian peak fits to BSE peaks. The dashed line shows the average FWHM.

Figure 4.4(b) shows the full width at half maximum of the Gaussian fits as a function of incident energy. There appears to be no trend for higher beam energies. Since the thermal spread of emitted electrons is expected to be ~0.3 eV the size of the BSE peaks suggests an estimate of the HGRFA resolution at ~ ±1.7 eV. Nickles has attributed this to the asphericity of the HGRFA and finite beam spot size (Nickles, 2002).

4.2. Conductor Yield Tests

Because of its chemical inertness, Au is often used as a calibration standard for electron-yield measurements (Dennison, *et al.*, 2016a). Also, because it is a conductor, measurements can be performed using both DC and pulsed methods to demonstrate that both methods give the same results. Figure 4.5 shows the measured TEY versus incident energy using both the DC and pulsed methods. These tests showed good, but not excellent, agreement overall. At low energies, $<200\,eV$, they agree to within uncertainties in the measured yields. But for higher energies, the DC method gave lower values than the pulsed method. This difference is most likely due to the increase in carbon contamination that occurred in the time between when the two data sets were taken (see Section 4.2.3). This makes sense because at low incident energies the electrons do not penetrate all the way through the carbon layer; however, at high energies the SEs excited from the Au have to travel through the carbon layer so absorption by a thicker carbon layer would reduce the height of the Au yield.

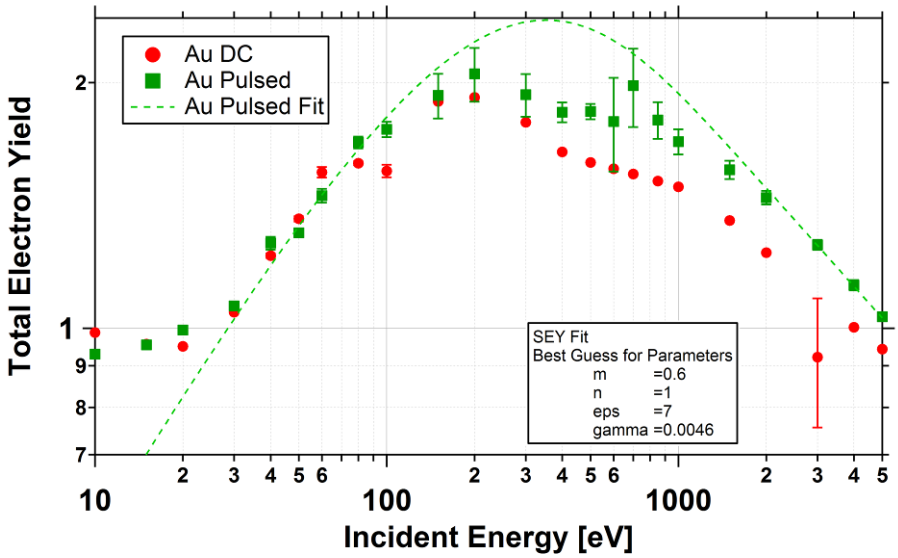

FIG. 4.5. Comparison of DC to pulsed TEY measurements on Au.

4.2.1. Au Standard

DC and pulsed-yield measurements were performed on Au because it is a conductor and chemically inert. The Au sample (25 μm thick 6N high purity Au foil) used was chemically cleaned and baked out along with several other Au samples at USU. These were distributed among several international research groups as part of a collaborative effort to compare yield measurement methods and to determine the best calibration standard for TEY measurements (Dennison, *et al.*, 2016a). Figure 4.6 shows the results of these round robin Au tests. Figure 4.6(a) displays the measured yield versus energy graphs, which were taken by each group. Figure 4.6(b) shows reduced yield curves, σ/σ_{max} versus E_0/E_{max}, on a log-log graph displaying the relative effect of carbon contamination, manifest in the variable size of the lower energy peak. Table 4.2 shows results of σ_{max}, E_{max}, E_1, and E_2 from each facility. When comparing the results from each study, it was found that many of the yield curves had two peaks, one at ~200 eV and another at ~700 eV. While the relative maximum yields differed, the energies were consistent. This was theorized to be caused by varying amounts of carbon contamination, which was built up on the surfaces of the samples. Surface contamination has been discussed by many other researchers to have a large effect on yield measurements, because most emitted SEs originate within the top few nm of a material (Seiler, 1983; Chang, *et al.*, 2000; Dennison, *et al.*, 2016a). This could have resulted from a problem with the cleaning

process, or from carbon deposition in the vacuum chambers enhanced by the incident electron beam (Davies and Dennison, 1997; Chang, *et al.*, 2000). The reduced-yield curves showed very good agreement with the shape $E > E_{max}$; however, there was much less agreement for $E < E_{max}$.

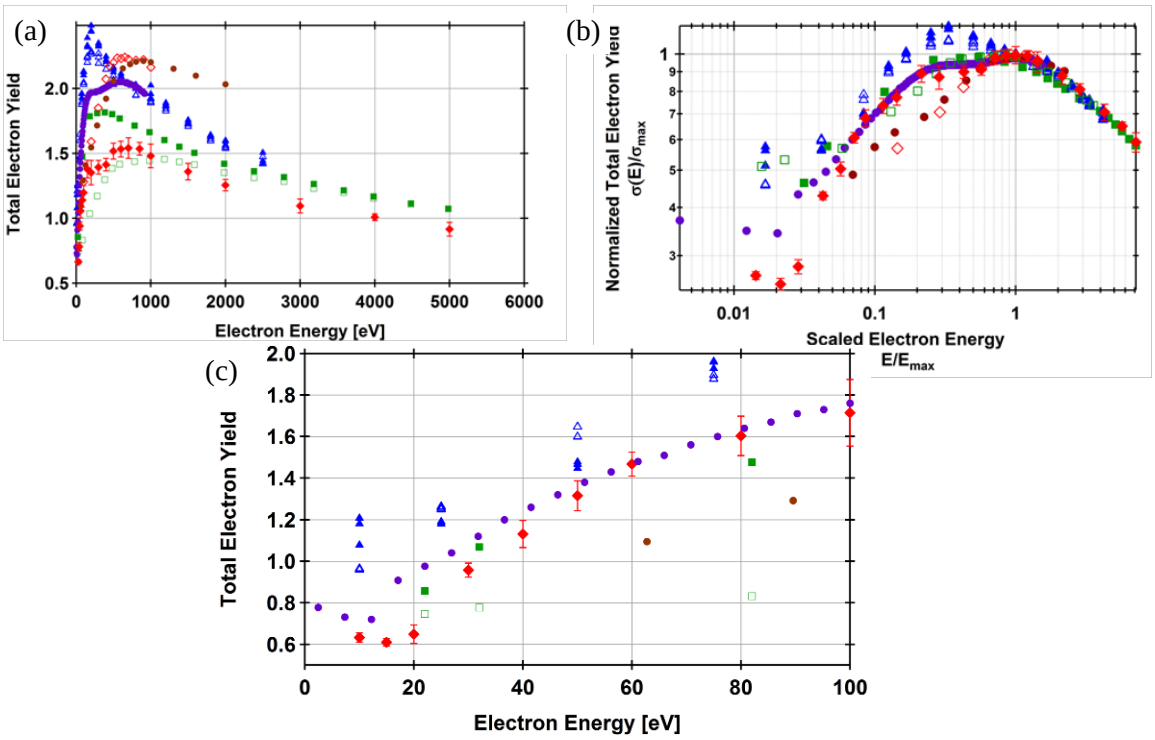

FIG. 4.6. Round robin tests on Au by research groups in four countries. (a) Linear plot of the total yield versus energy. (b) Log-log graph shows normalized yield (σ/σ_{max}) versus scaled energy (E_0/E_{max}). (c) Expanded version of (a) showing detail at low energies (Dennison, *et al.*, 2016a).

Table 4.2. Round robin Au results.

Symbol	Facility	Refs.	Measured Values			
			σ_{max}	E_{max} (eV)	E_1 (eV)	E_2 (eV)
●	CSIC SEY Facility (contin.)	1-3	2.06±0.02	600±20	24±1	NA
■	Onera—DEESSE Facility	4-5	1.81±0.03	360±20	28±1	~6000
□	Onera—DEESSE (Etched)	4-5	1.46±0.03	1250±50	NA	~6000
▲	LaSeine—TEY Facility (March 2)	6-7	2.48±0.03	200±20	NA	NA
Δ	LaSeine—TEY Facility (March 6)	6-7	2.3±0.1	240±30	12±2	NA
♦	USU—SEEM Facility (pulsed)	8-9	1.54±0.08	700±30	55±3	4000±200
◊	USU—SEEM Facility (contin.)	8,15	2.24±0.02	650±50	NA	NA
	Round Robin Average Values		2.0±0.4	600±460	24±9	5000±1000
●	Standard: Thomas & Pattinson	11	2.21±0.02	900±30	50±10	NA

4.2.2. HOPG Tests

Another test, which was done as part of the round robin project, was a comparison of yield measurements for highly oriented pyrolytic graphite, or HOPG. This material is a synthetic version of graphite with large in-plane crystal size of ~1 μm and excellent alignment of the graphite basal planes (Chung, 2002). It is also a nice material to test, because of the ease of cleaning using the standard scotch tape method to peel off the top layer of graphite and expose a fresh new layer beneath (Dennison, 1985).

Figure 4.7 and Table 4.3 show the compared results for HOPG, which were in much better

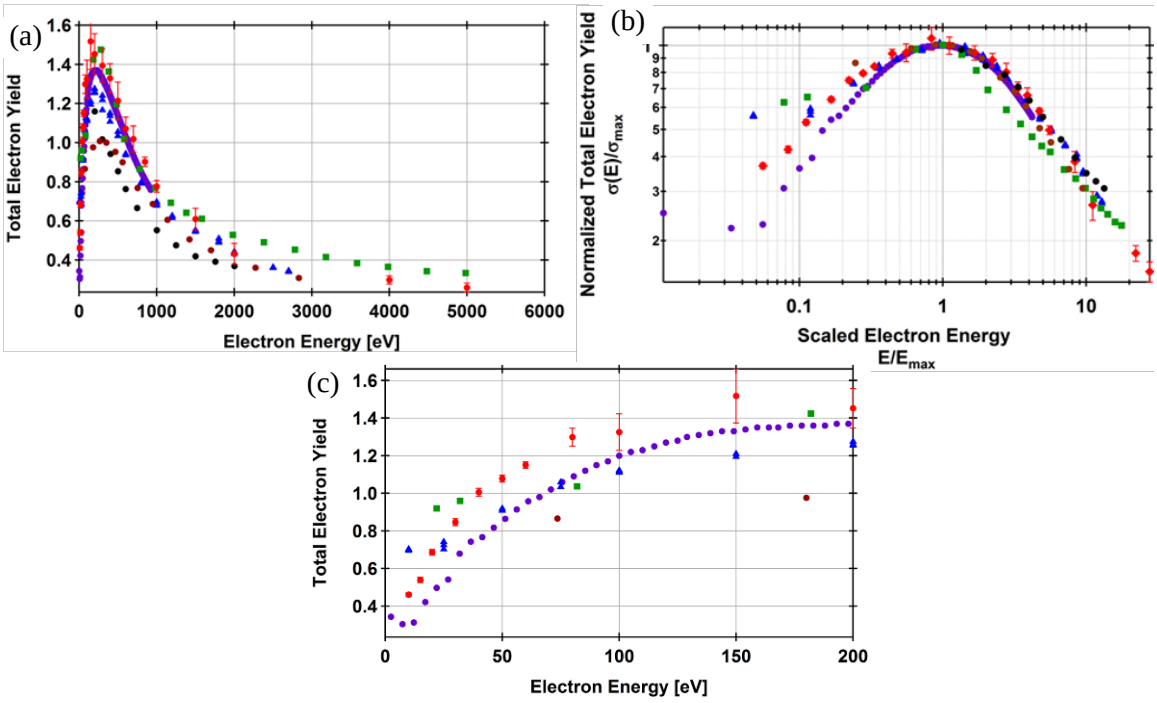

FIG. 4.7. Round robin tests of HOPG. (a) Linear graphs of the total yield versus energy. (b) Log-log graph of normalized yield versus scaled energy. (c) Enlarged version of (a) showing details at low incident energy (Dennison, 2016).

Table 4.3. Round robin HOPG results.

Symbol	Facility	Refs.	Measured Values			
			σ_{max}	E_{max} (eV)	E_1 (eV)	E_2 (eV)
●	CSIC SEY Facility	1-3	1.38±0.02	215±5	68±1	629±10
■	LaSeine—TEY Facility	4-5	1.48±0.05	270±20	60±2	610±40
▲	Onera—DEESSE Facility	6-7	1.28±0.05	190±10	69±1	552±20
♦	USU—SEEM Facility (clean)	8,9,15	1.4±0.1	200±30	40±2	895±20
	Round Robin Average Values		1.39±0.08	220±36	59±13	670±150
●	Standard 1: Whetten	12	1.01±0.01	300±20	250±30	350±20
●	Standard 2: Wintucky	13	NA	NA	NA	330±20

agreement than for Au, both in σ_{max} and E_{max}. This suggests that HOPG would be a better calibration standard. Also, these tests are what led to the theory of carbon contamination for the Au tests, because of the location of the peak for these tests, as well as previous work, which demonstrated carbon contamination in the vacuum chamber (Davies and Dennison, 1997; Chang, *et al.*, 1998)). The graph in Fig. 4.8 shows fits using Eqs. 2.15, 2.19, and their sum to the most recent USU SEY, BSEY, and TEY measurements on HOPG.

4.2.3. Carbon Contamination Over Time

As was briefly discussed in Section 4.2.1, there was evidence of a carbon contamination layer growing on the Au samples used in the round robin tests. To further study this, TEY measurements were made on the same Au sample over the course of ~10 months in the USU SEEM chamber. These measurements are shown in Fig. 4.9.

One way to understand what is happening with a contamination layer over the sample is to look back at the models discussed in Chapter 2. At low energies the beam does not penetrate very deeply into the layered material and the yield measured is mostly due to the carbon. If the carbon does not completely

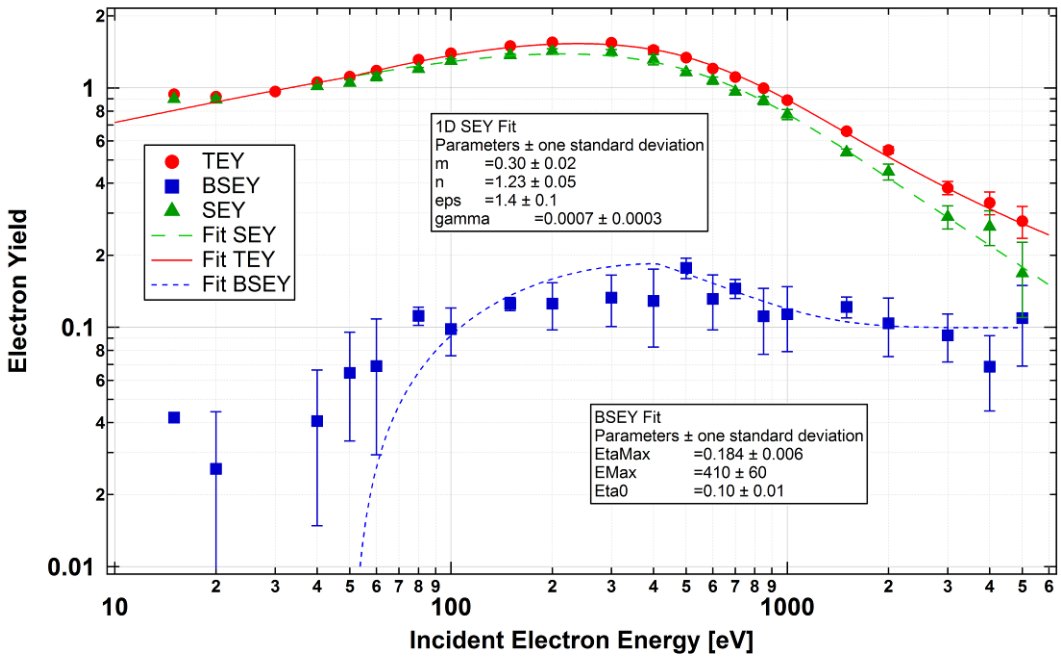

FIG. 4.8. Yield fits of highly ordered pyrolytic graphite.

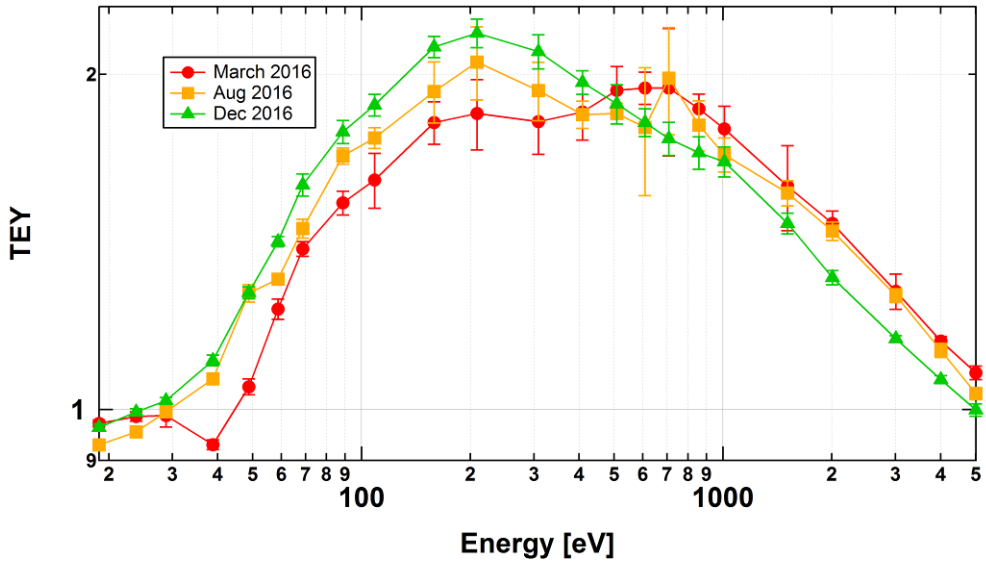

FIG. 4.9. Au contamination tests. Measurements taken over ~10 months suggest growth of a C contamination layer on a Au sample. These show an increasing C peak at ~ 200 eV and a decreasing Au peak at ~ 600 eV.

cover the Au, then the measured SEY will be an average of the two independent materials weighted by the percent areal coverage of the carbon. Over time, it should be expected that both the carbon layer thickness, as well as the percent coverage, will increase producing a yield at low energies that more closely matches the yield of disordered carbon by itself (Davies and Dennison, 1997; Chang, *et al.*, 2000).

At higher energies, once the range of incident electrons starts to penetrate through the carbon to the Au, the yield will transition to reflect the behavior of the pure Au yield curve. The biggest difference between the measured yield at high energies and the yield of pure Au at high energies is determined by the drop in yield caused by Au SEs losing energy as they travel through the carbon layer before escaping into the vacuum. This is also expected to cause a drop in the Au peak with increasing carbon coverage and thickness. From the data shown in Fig. 4.9, both of these effects can be seen as the carbon peak grows and the Au peak shrinks over time. The Au peak also should shift to lower energies as incident energy is lost going through the C layer before it reaches the Au.

4.2.4. Biased Au

To mimic the effects of charging in an insulator, tests were done while biasing Au to various potentials. These tests are similar to those done by Hoffmann (Hoffmann, 2010) using the instrumentation

before the enhancements made for this thesis. The objective was to see how this modified the yield curve relative to the unbiased measurements discussed above; they would provide information about how positive and negative charging modifies the measured yield values.

All tests were done with a 208 eV beam; the Au sample was biased positive to 2, 3, and 4 V. The incident energy of 208 eV was picked because it had the largest yield for Au of $\sigma_{max} = 2.1 \pm 0.2$. As predicted by the model, increased sample voltages led to a reduction in the measured total yield values (Hoffmann, 2010). The first points in Fig. 4.10 show the results of these tests with 0 V inner grid bias. As is expected, the measured yield value is lower because low-energy SEs are reattracted to the sample with increasingly positive sample bias. Since the TEY is just under one for a sample bias of +4 V, it can also be estimated that a floating Au sample would charge up to about +4 V before it would reach equilibrium. These tests are consistent with the ideas expressed in Fig. 2.7 showing the shaded area under the electron emission curve, representing low-energy SEs, which are reattracted by a positively biased sample.

4.2.5. Biased Grids

While doing the biased sample tests, the feasibility of biasing the inner grid to create a constant potential region around the sample—and thus a zero electric field region—was studied. It was not known at

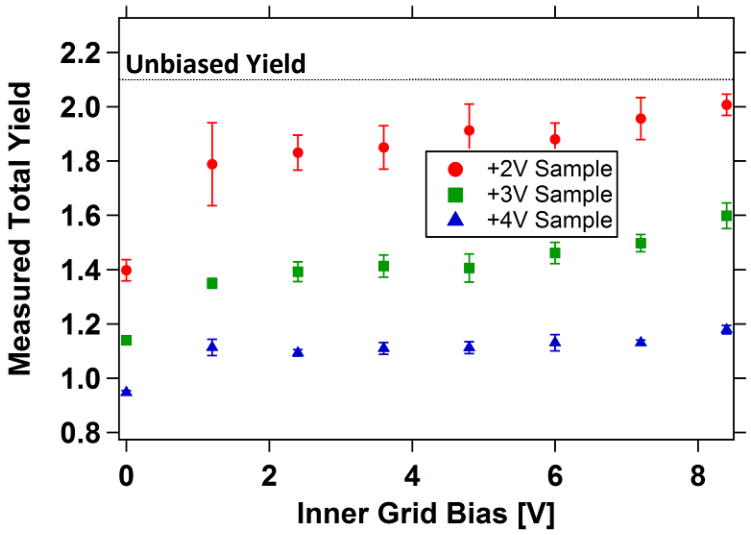

FIG. 4.10. Au sample bias tests. TEY measurements made on Au sample biased to +2, +3, and +4 V with varying amounts of inner-grid biasing.

the time of these tests whether the sample aperture should also be biased or left at chamber ground. For these tests, the sample aperture was left grounded and only the inner grid was biased. Figure 4.10 shows the measured yield values with various sample and inner grid biasing. It was expected that for a given sample bias the same bias would be necessary on the inner grid in order to recover the unbiased yield measurement of $\sigma_{max} = 2.1 \pm 0.2$. This was not the case, however, as is evidenced by the decrease in yield with higher sample voltages for all tests.

To further study the effect of different HGRFA biasing schemes on electron trajectories, simulations were performed in SimIon 8.1 (see Fig. 4.11). The bias schemes used for each of these tests are found in Table 4.4. Figure 4.11(a) shows the trajectories of 2.5 eV electrons emitted from a +3 V biased sample. Notice that all of the electrons are reattracted to the sample. While SEs have a distribution of energies, and in the real world some higher energy SEs would be able to escape, a large fraction of SEs have energies less than +3 eV, so a sample potential as small as +3 V has a large effect on the measured yield.

Figure 4.11(b) shows the result of biasing the inner grid to +3 V. This allows some of the electrons to escape the sample; however, fringe effects from the grounded stage plate cause SEs with shallow emission angles to be sent back to the sample. The grounded stage also acts to redirect other SEs once they escape the sample, causing their trajectories to leave their initial radial directions. These results suggest that removing fringe fields close to the sample should help to maintain radial trajectories. These fringe fields may explain the failure of the inner grid bias tests to compensate for sample voltage.

To remove these fringe fields, the stage should be biased along with the inner grid to help produce a nearly equipotential volume inside the inner grid. The next figure, Fig. 4.11(c), shows the results of this biasing scheme. Because this produces a very uniform potential around the sample, the electric field in that region is nearly zero. This can be seen by the very straight trajectories close to the sample. With this scheme the largest source of error is caused by fringe fields close to the grounded beam drift tube. A future modification may allow the possibility of biasing the drift tube.

Because of the difficulty in knowing the precise sample potential we should also look at the effect of having a stage/inner-grid bias larger and smaller than the sample potential. Using a bias that is higher

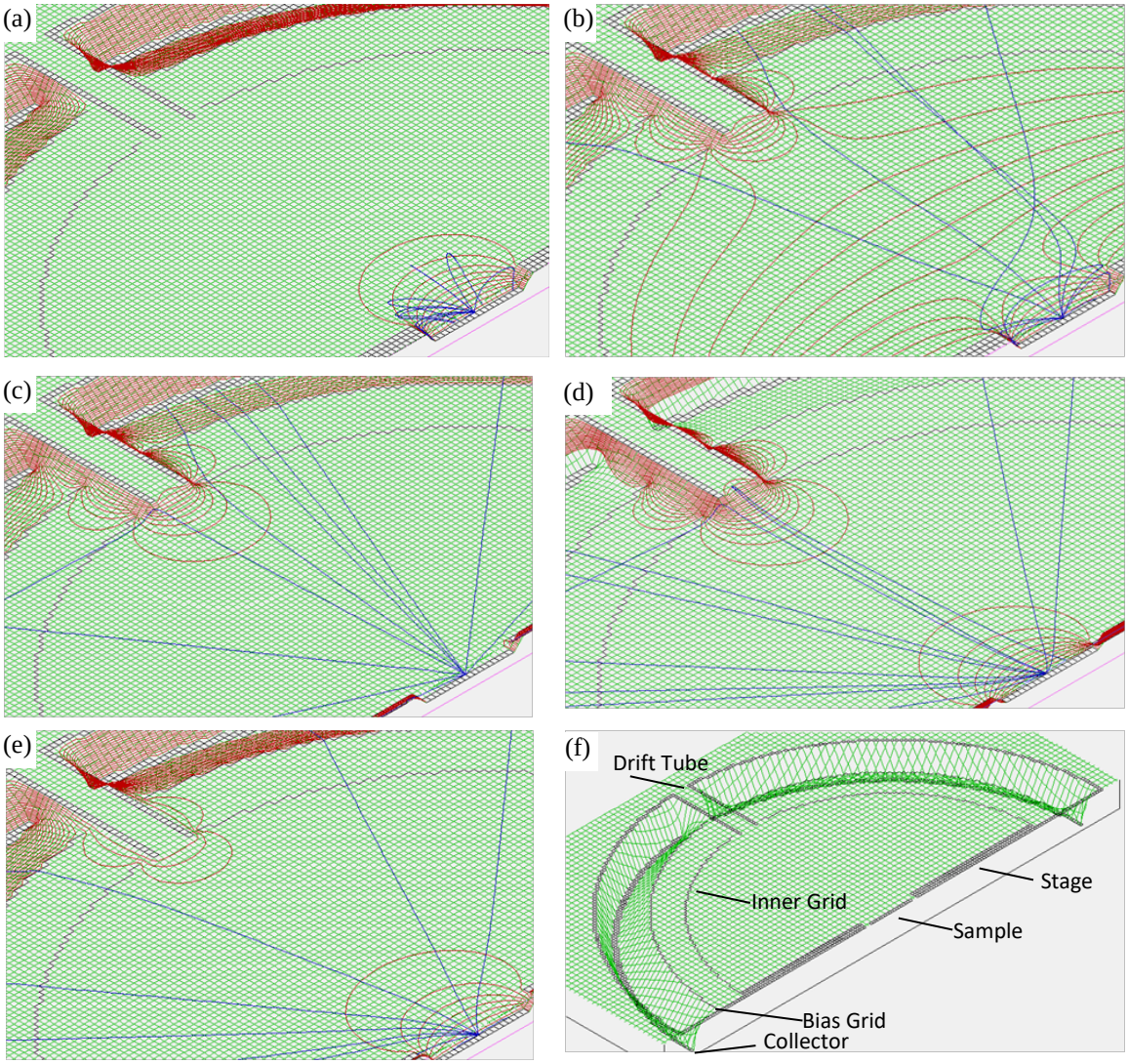

FIG. 4.11. SimIon HGRFA electron trajectory simulations. Figures (a)-(e) show the effects of various HGRFA bias schemes on low-energy SE trajectories (blue). Potential contours (brown) help to visualize the forces on the electrons. Table 4.4 shows voltages used for each figure. Figure (f) shows labels for each of the HGRFA components for reference.

than the +3 V sample (+6 V) as in Fig. 4.11(d), the resulting trajectories are very similar to those in Fig. 4.11(c). Again, fringe fields around the drift tube and at the edge of the sample cause electrons that pass through these regions to deviate from their radial trajectories. Lastly, using a bias that is smaller than the sample potential, as in Fig. 4.11(e), the effect of the sample-edge fringe fields is still much smaller than using no bias.

Table 4.4. SimIon bias voltage simulation.

Figure	Sample (V)	Inner Grid (V)	Stage (V)	Bias Grid (V)	Collector (V)
4.11(a)	3	0	0	0	6
4.11(b)	3	3	0	3	6
4.11(c)	3	3	3	3	6
4.11(d)	3	6	6	6	10
4.11(e)	3	1	1	1	6

These tests suggest that the only way to maintain a region of zero electric field around the sample while biasing the inner grid is to bias both the inner grid and the stage to the same surface potential as the sample. However, if the inner grid and stage are biased close to the same potential as the sample, then the trajectories of emitted electrons are only slightly affected.

4.2.6. Emission Spectra

The emitted energy spectra were measured for both neutral and biased Au samples to further study how biasing of various HGRFA components affected the emitted electron energies. All tests were done without changing the electron gun settings so that the size of the peaks could be compared, as well as the relative positions along the energy axis. The resulting shifts in the energy distribution peak energies provided information about where the electrons originated, as well as how various biasing schemes affect the shape of the energy distributions.

The first spectra were measured for a neutral and ±5 V biased Au sample (see Fig. 4.12). The theory for how sample charging affects the emitted electrons (Section 2.3) predicts that, as a sample charges, it develops a surface voltage, which shifts the emitted secondary electron peak by the same amount of electron volts. After this shift, any part of the spectrum that has negative energy will not be able to escape the sample. Figure 4.12(a) shows the results of +5 V sample bias. Notice that the biased SE peak in this figure appears to be much smaller than the unbiased SE peak. Also interesting is the lack of any shift in the BSE peak. The BSE peak does not change with sample biasing, because the electric forces that accelerate the incident electrons to higher energies as they come into the sample lower the emitted energies by the same magnitude as they leave. The shifted unbiased peak data shows very good agreement with the

(a)

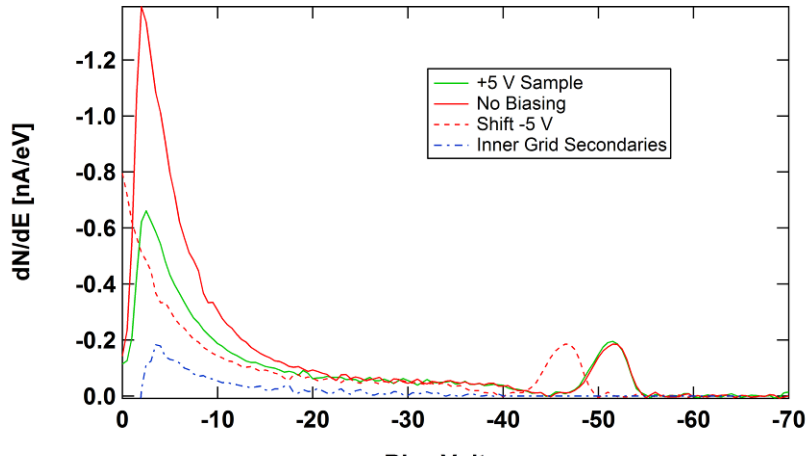

(b)

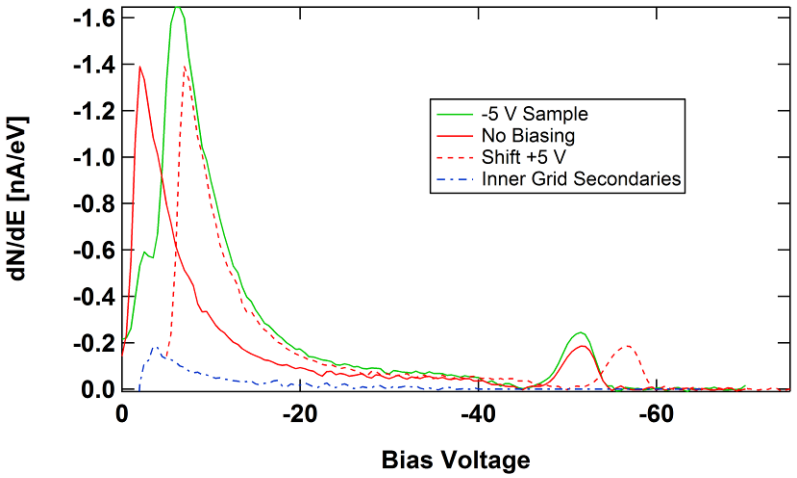

FIG. 4.12. Emission energy spectra of biased Au. Comparison of spectra of unbiased Au to (a) +5 V, and (b) -5 V Au sample. The incident beam has an energy of about 51 eV. A ±5 V shifted copy of the unbiased data (dashed red) is included to demonstrate the concept of the yield versus charge model. Blue dashed curve shows approximate shape of the emission spectra of SEs created through electrons colliding with the inner grid (~14%) of measured secondaries.

shape of the -5V biased spectra; however, the shifted peak is too small in the +5 V biased spectra. The reason for this discrepancy is most likely due to extra secondary electrons, which are generated by the inner grid, as a small fraction of BSEs collide with the grid on their way to the collector (Hoffmann, 2010). The energy distribution is approximated in the dashed blue curves added to both graphs. This approximation was calculated by finding the difference between the measured shifted curve and the theorized dashed red shifted curve. SEs from the inner grid are not shifted by the sample potential and the only fields they must overcome if they are emitted toward the collector are those between the inner grid and the bias grid.

Because they are not affected by sample bias, these electrons are the cause of the low-energy shoulder on the SE peak in the -5 V biased spectra.

The next tests were done to investigate the effects on the emission spectra when biasing the inner grid and sample aperture to various potentials leaving the sample grounded (Fig. 4.13). These peaks looked very similar to the previous tests. This makes sense, because the fields around the sample depend on the difference in the potential between the sample, and the inner grid and sample aperture. The shapes of the SE peaks, therefore, should be identical if the difference of the HGRFA potentials are the same. The big difference between the inner grid bias tests and sample bias tests are the effect on the BSE peaks. Because the electron gun and sample are both at zero potential for these tests, the PEs have no cumulative change of

(a)

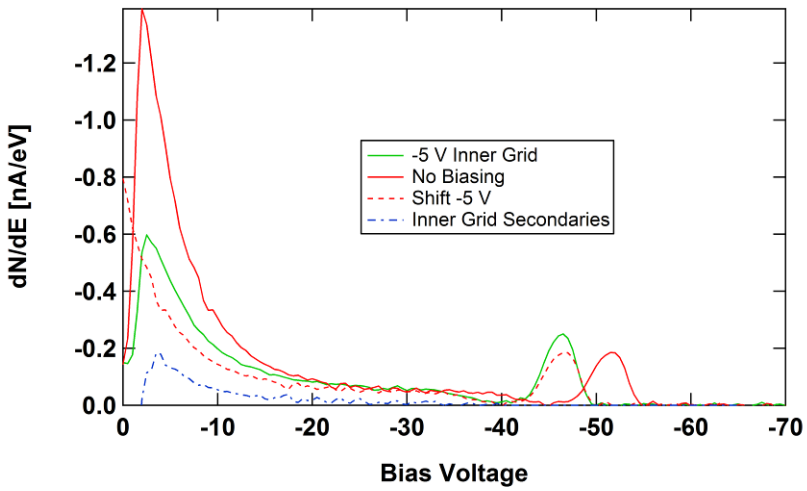

(b)

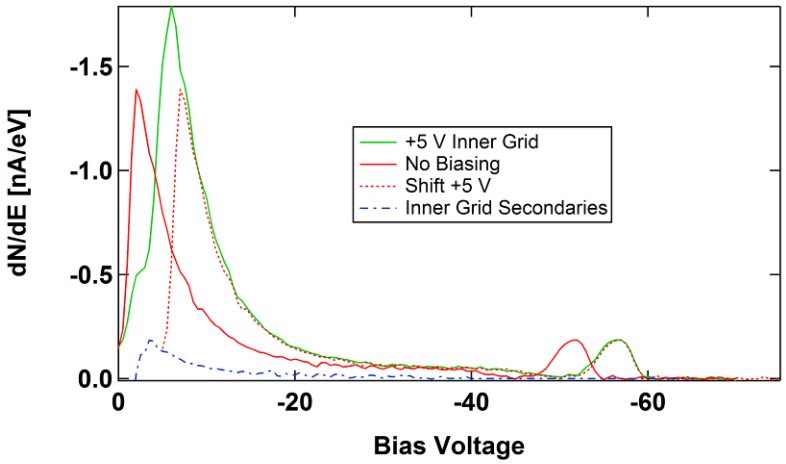

FIG. 4.13. Au emission spectra with inner grid bias. Graphs compare unbiased Au spectra with (a) -5 V and (b) +5 V inner grid biasing. The incident beam has energy of about 51 eV. A shifted copy of the unbiased data (dashed lines) is included to demonstrate the validity of the yield versus charge model. Blue dashed curves show the approximate distribution of SEs generated through electron collisions with the inner grid.

energy between the gun and the sample; however, the BSEs see a change in potential as they move from the sample to the inner grid. By comparing the shifted spectra to the biased spectra, both the SEs and BSEs experience a shift in energy when the sample is grounded and the inner grid is biased. The approximate energy distribution of SEs from the inner grid is also included in these graphs to explain the discrepancies in measured versus theorized curves at low emitted energies.

The last spectra tests done compared unbiased spectra to spectra that had both the sample and inner grid biased to the same potential (see Fig. 4.14). Because the difference in sample and inner grid potentials was zero, this should produce an area of zero electric field around the sample, which should mimic the unbiased SE spectra. This produced the same size and location for the SE peaks as seen in Fig. 4.14. There is some slight variation in their shape, which is most likely caused by small lingering fringe fields in the HGRFA, as well as modifications to the yield due to changing the landing energy of incident electrons. These tests validate the ideas developed in Section 4.2.5 on biasing the inner grid and the sample aperture to the same potential as the sample.

4.3. Neutralization Tests

The next group of tests was designed to study different aspects of our charge neutralization methods. Figure 4.15 shows yield measurements made by Hoffmann (Hoffmann, 2010) on Al_2O_3. Regions

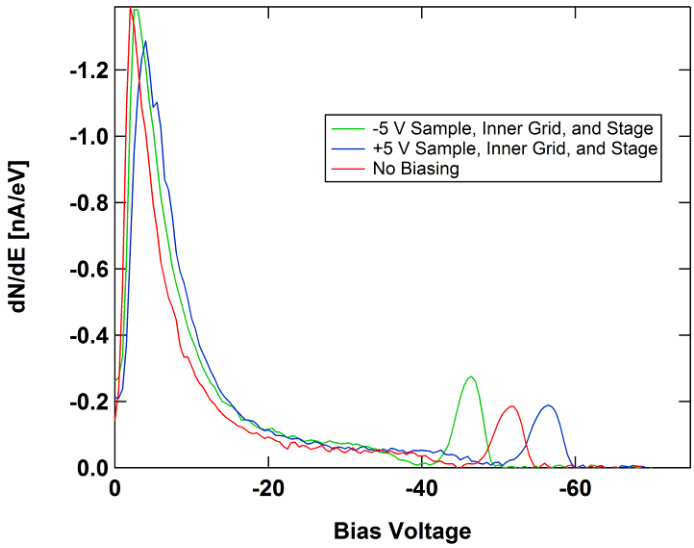

FIG. 4.14. Au emission spectra with equal sample and inner grid bias. Graphs compare unbiased Au spectra to spectra using equal sample and inner grid bias. The incident beam has energy of about 51 eV.

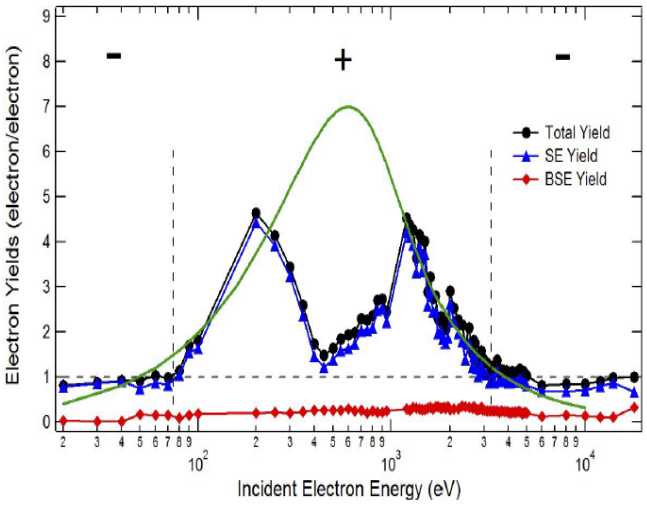

FIG. 4.15. Goals for neutralization improvement (Hoffmann, 2010). This graph shows regions of negative and positive charging in data taken before this work on Al_2O_3.

of negative and positive charging were still visible despite the novel techniques he developed. After making the improvements discussed in Chapter 3, the following aspects of charge neutralization were tested:

- Negative charging.
- Positive charging.
- Electron flood gun settings.
- Necessary flood duration.
- UV effectiveness on large band gap materials.

4.3.1. Neutralization Duration

Each pulse deposits a certain amount of charge in the sample, and the neutralization techniques are expected to discharge the samples at a certain rate. Therefore, it was necessary to determine how long the sample should be flooded with electrons and UV light between each incident electron pulse in order to completely neutralize the samples. The yield versus pulse curves are expected to have slower variations over time for inadequate neutralization relative to the initial yield versus charge tests; and the yield should remain at the uncharged value for flood durations longer than what is necessary. These results are also expected to vary from one material to another depending on how efficient UV neutralization is on each material.

Figure 4.16 shows how measured yield of Kapton® with 208 eV incident electrons changed from pulse to pulse as the sample voltage changed with incident charge. For this test, only electron flooding was used. The red curve shows how TEY changed from pulse to pulse without any neutralization between pulses. Between this and other multi-pulse data sets, complete neutralization was attempted by flooding the sample with UV and electrons for a few minutes; however, none of the other tests started with as high of a TEY measurement as the first, zero flooding, run. For flooding durations less than five seconds, the slope was negative, which indicates insufficient neutralization. For five second flooding, the curve began with a negative slope; however, it changed to positive during the run. This is assumed to be due to instability fluctuations in the flood gun output. This suggests, however, that five seconds of flooding is close to the amount necessary to remove the deposited charge. Above five seconds, the slope was more positive, indicating that the sample was being discharged.

4.3.2. Yield Versus Charge Build Up

Tests were planned to measure how the yield of an insulator changes as the yield measurements caused charge to build up in the material. Because of the lower amount of charge per measurement (~150 fC/mm^2) we are able to use, there should now be much better resolution in the yield versus charge buildup graph that Hoffmann used (Fig. 1.2). His model also predicts a plateau at very small sample potentials indicative of the intrinsic yield, which we hoped to see with these new measurements. These measurements

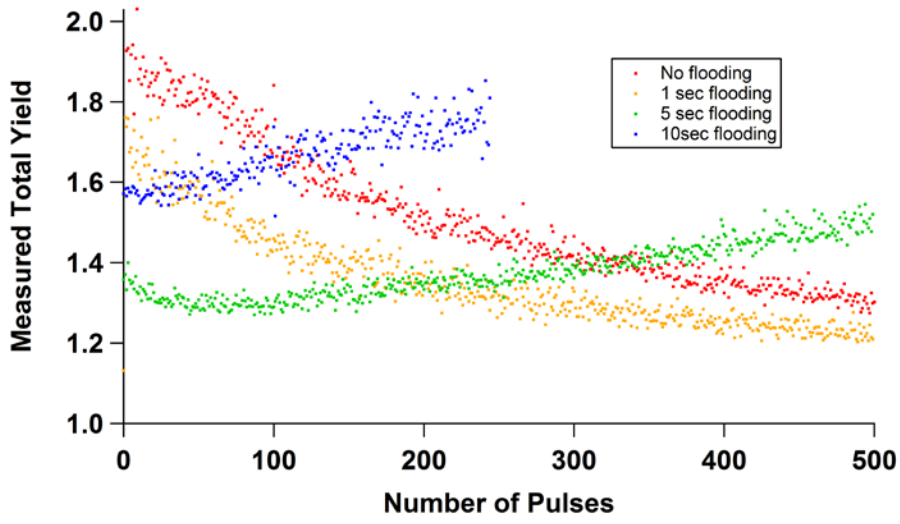

FIG. 4.16. Flood duration tests.

will also provide information about modeling yield as insulators charge up. It was theorized that UV neutralization would work better on samples with low enough band gaps to absorb UV photons. For these tests Kapton® was used because of its relatively low band gap of ~ 2.3 eV compared to that of our peak UV LED emission (4.86 eV).

Figure 4.17 shows the results of the yield versus charge tests done on Kapton® HN. The axes of the graph are in logarithmic form to help display details in the data over all ranges of incident charge. The red curve shows consecutive TEY measurements made without neutralization between pulses. For these data, we saw that there was a plateau at low incident charge, which confirms the model developed by Hoffmann. Data from Hoffmann's work is also included to demonstrate improvement due to enhanced instrumentation, and to show the eventual approach to a yield of unity. The figure also shows tests done with 10 *s* of flooding between each pulse. The first two sets (blue and green curves) were taken right after the nonflooding data, and the sample had not been flooded long enough to return it to its original uncharged state. It is interesting, however, to note that the yield slowly drifted upward during each data set suggesting that more charge was being removed than deposited over time. Finally, after discharging the sample overnight with UV and heat lamps through the chamber windows, data were taken starting with an uncharged sample showing that ten seconds of electron and UV flooding was long enough to maintain the yield at the uncharged value of ~2.4. Flooding tests were done using 200 pulses with flooding between each. The no flooding data were taken using 500 consecutive pulses. Data from Hoffmann's thesis is also included (purple) for comparison. When shifted by a factor of 100 (black), it lines up well with the tail end of the no flooding data (red), and displays the eventual approach to a yield of one.

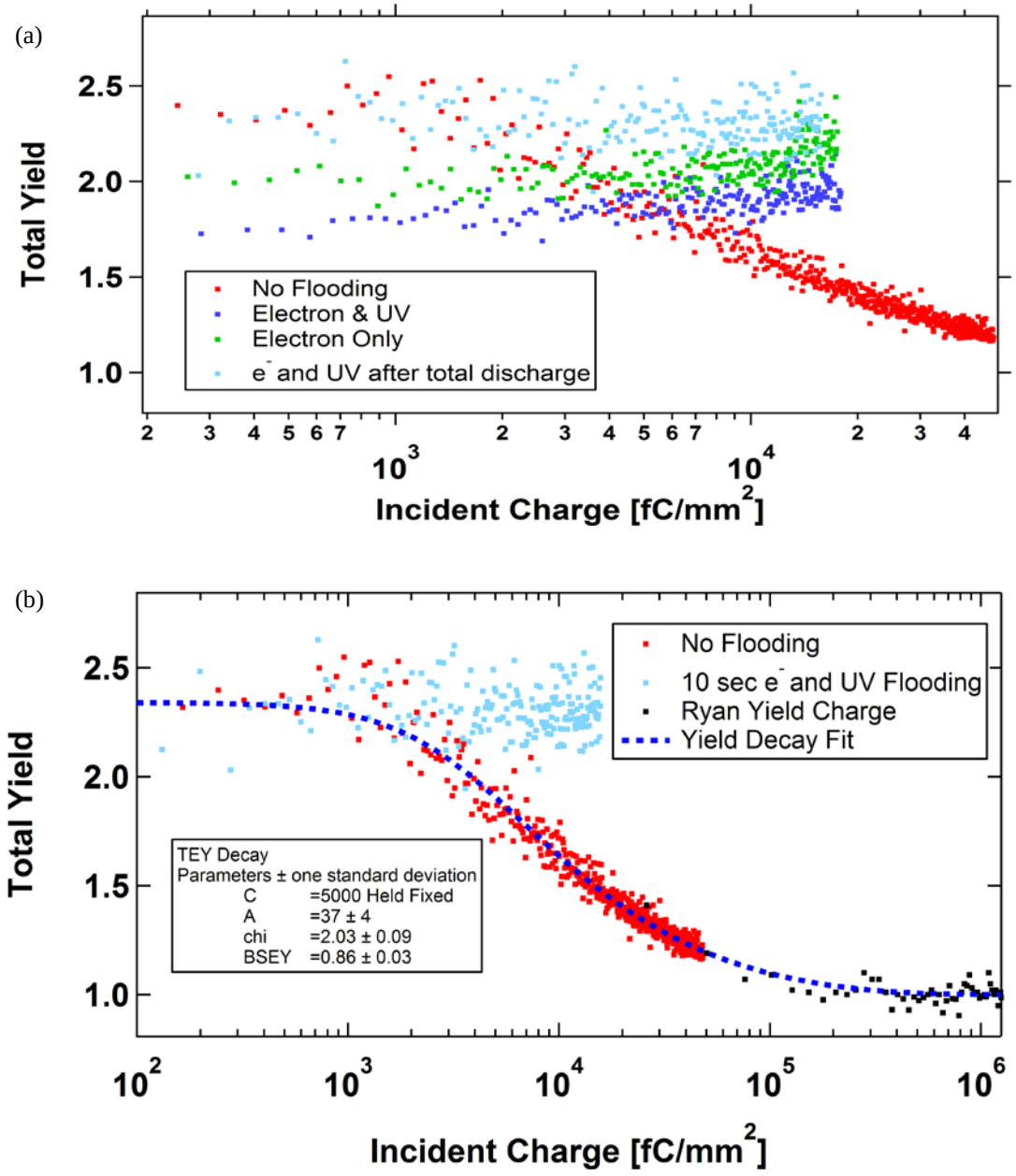

FIG. 4.17. Kapton HN yield decay curve. Change in measured yield of Kapton® with 408 eV incident electrons from pulse to pulse as the sample voltage changed with built-up charge. Figure (a) compares the effects of various neutralization techniques, and (b) shows reduction in incident charge from previous neutralization attempts. Curves are of data taken with no flooding (red), 10 *s* of electron/UV flooding starting partially charged (blue), electron flooding starting partially charged (green), and electron/UV starting completely discharged (cyan). Data taken by Hoffmann (Hoffmann, 2010) are also included for comparison (black).

4.3.3. Point-wise Method Tests

The point-wise method was expected to show a drift in the yield value over the course of one pulse for insulators, and to be constant for conductors. To determine whether it was working, point-wise tests were done on Au (see Fig. 4.18), to hopefully show a flat yield value over the course of the pulse. The horizontal dashed line shows the value of the yield calculated using the integrated pulse method. Comparing the point-wise method to this value shows that the point-wise yield method is not fully working correctly yet. To estimate the uncertainty of this method, the analysis was limited to only regions where currents are appreciable and well above current noise (area of point-wise curve enclosed in vertical lines). This gives a linearly decreasing TEY from ~1.35 to ~1.20, a ~12 % drop, or ~±4% difference from the average (integrated current) value. A few possible reasons for this could be time delay in some of the signals due to time-of-flight, delay due to cabling, or overshoot and ringing due to collection circuit and electrometer inductance and capacitance. Alternatively, this modest change could be due to charging of the contamination layer observed on Au samples (see Section 4.2.3).

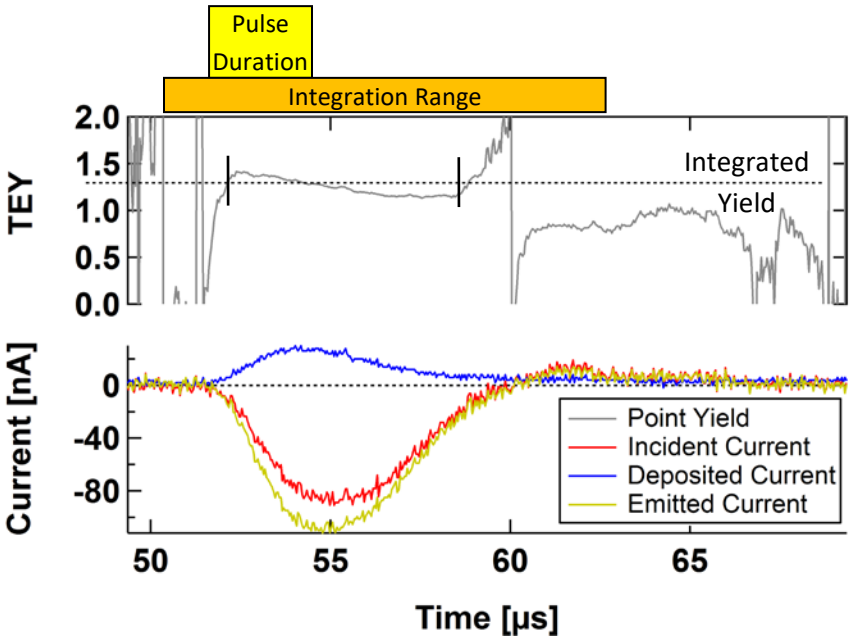

FIG. 4.18. Point-wise yield results. Point-wise yield (gray) of Au using 2000 eV electrons is shown along with incident (red) emitted (yellow), and deposited sample (blue) current pulses. The dashed line shows the average yield (1.29±0.02) calculated by integrating incident and emitted charges over the range specified. Vertical bars show the time span of interest for point-wise analysis.

Calculations were made to determine if the drift in point-wise data over the course of a pulse could be due to time-of-flight delay between the various HGRFA elements. This was done simply by using the equations

$$\Delta T_{ToF} = distance/velocity,$$

$$velocity = \sqrt{2\times Energy/_{mass}} = \sqrt{\frac{2E}{m_e}}, \tag{4.5}$$

for a scattered electron of energy, *E*. Figure 4.19 shows the result of this calculation for the time required to travel 4.5 cm from the sample to the collector. The dashed line is the temporal spacing (ΔT_{ToF}= 0.04 μs) between oscilloscope data points for comparison. For all the incident energies that we used, the delay from time of flight for the electrons is smaller than the spacing between data points. In fact, even for energies as low as 3 eV the delay only amounts to one oscilloscope data point time increment. This is not enough to produce the drifting problems, which are seen in conductors.

After closer inspection of Fig. 4.18, it was noted that the oscilloscope pulse traces had a width

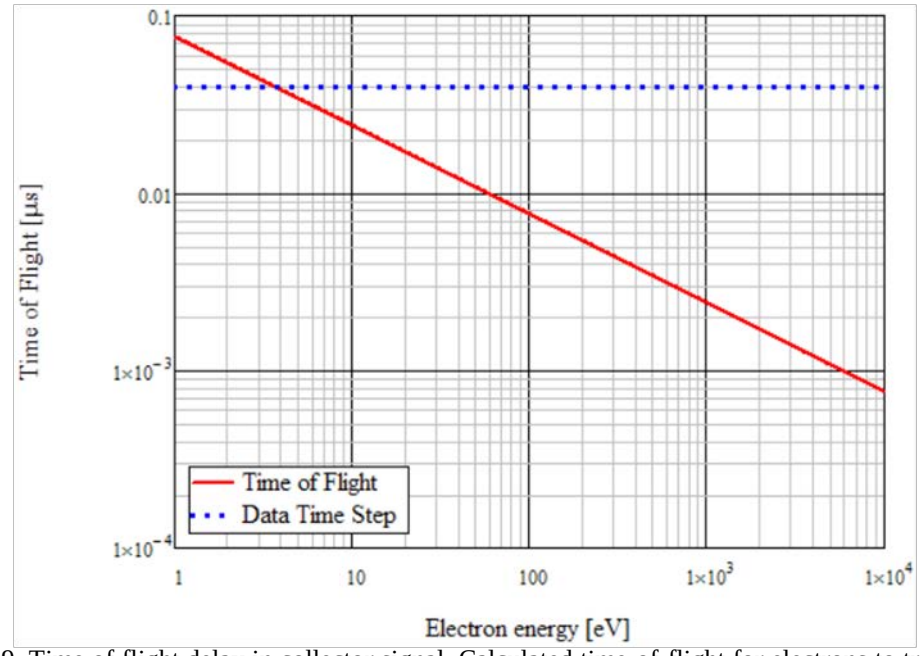

FIG. 4.19. Time of flight delay in collector signal. Calculated time-of-flight for electrons to travel from the sample to the collector (a distance of ~ 4.5 cm is assumed) as a function of electron energy, using Eq.(4.5). This shows that for nearly all energies of interest, the time-of-flight delay is smaller than the measurement spacing of ΔT_{ToF}=0.04μs (blue dashed line).

much larger than the 3 μs that was expected (~7 μs excluding ringing). The yellow shaded rectangle above Fig. 4.18 shows the approximate length of the actual electron pulse hitting the sample. The shape of the oscilloscope pulse traces can be understood by factoring in the rise/fall times of the electrometers (~ 4 μs). The leading edge of each peak shows the length of the actual pulse. Because the rise time is longer than the pulse duration, the voltage output of the picoammeters rises until the pulse ends, not quite reaching equilibrium. When the pulse ends the output voltage of the picoammeters begins to fall and approaches zero in ~ 4 μs. This gives a measured pulse length of ~ (3 + 4) μs = ~ 7 μs, which agrees well with our results. This also gives a possible explanation for the drifting in the point-wise TEY data if the various electrometers have slightly different rise/fall times.

4.3.4. Insulator Tests

After performing the various validation tests listed above, a few other low-conductivity materials were selected for testing. This was done to see how other yield curves compared to previous data taken, as well as to more accurately determine the intrinsic yield values of these materials. These tests also emphatically demonstrate the enhanced research potential made possible by the improvements in instrumentation and analysis. At the end of this chapter, Table 4.5 shows TEY parameters for each of these materials, as well as information about conductivity and band gap energy for each. Along with Table 4.5 is Fig. 4.27, which shows the optical transmission spectra of the materials in this section. This also demonstrates a rough estimate of the band gap of these materials by the abrupt transition from mostly transparent to opaque with photon energies above the band gap. These are included to compare the relative charging effects in the various samples and to help explain the effectiveness of UV neutralization.

4.3.4.1. Sapphire (Al_2O_3)

Yields were measured for a single crystal Al_2O_3 sapphire sample; the sample (UQC Optics, WSR-101) was 1 mm thick with a conductivity of $3\pm1\cdot10^{-16}$ $(\Omega \cdot cm)^{-1}$. Al_2O_3 was one of the more difficult materials for Hoffmann to measure, as it exhibited such a high yield and low conductivity. The tests done on Al_2O_3 also showed some difficulty with charging due to these properties (see Fig. 4.20(a)) as evidenced by the nonpower law (linear on a log-log axis) behavior at high incident energies. However, a similar E_{max}

value of ~700eV was measured, which Hoffmann determined by extrapolating from his data with the SEY model. Figure 4.20 (b) shows a new yield decay curve, which was measured with a 608 eV beam.

One difference between this decay curve and previous ones discussed in this thesis is that TEY is graphed versus deposited charge rather than incident charge. This is calculated by summing the sample

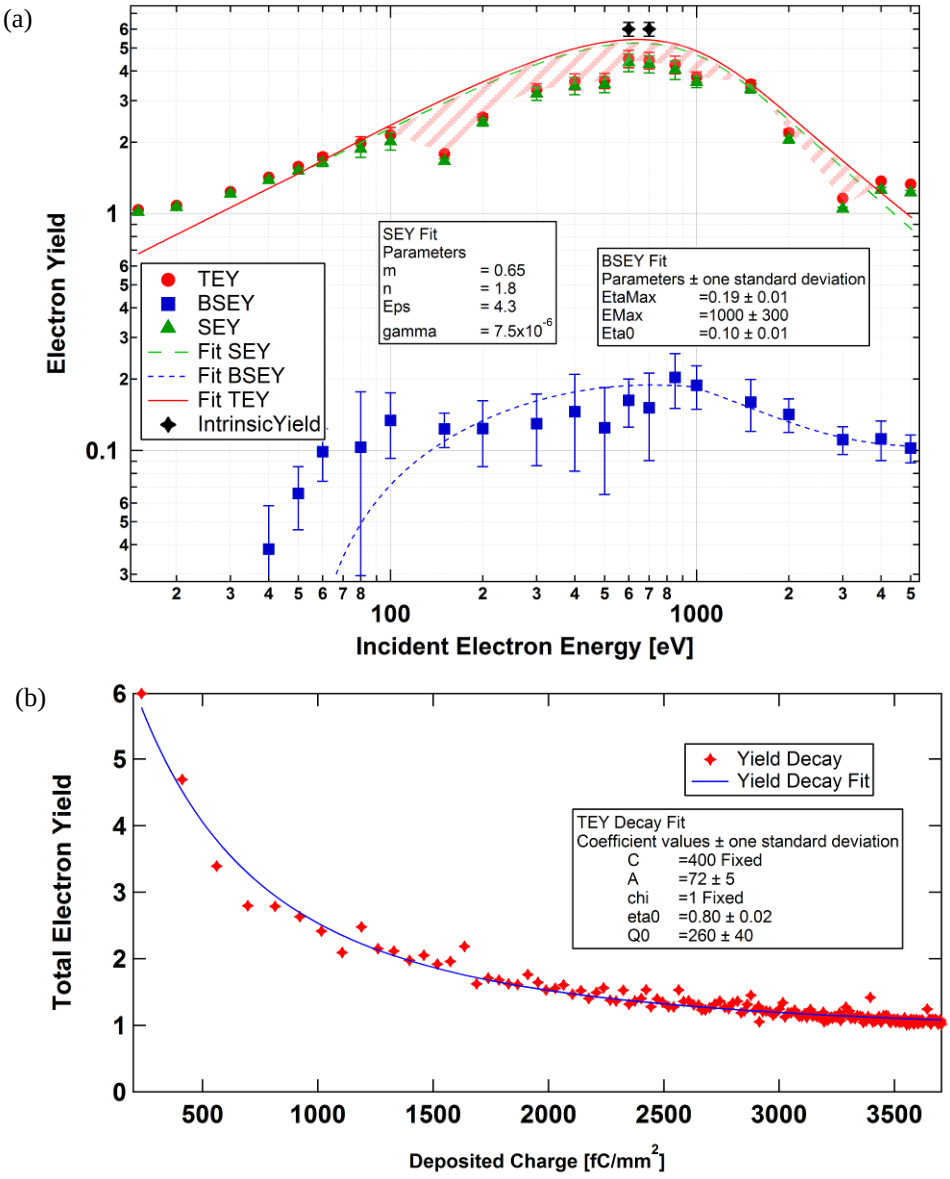

FIG. 4.20. Sapphire yield electron emission measurements. (a) Measured yield curve of sapphire with added best guess fit using the SEY model (Eq. 2.15) and a least squares fit using the BSEY model (Eq. 2.19). Shaded region shows the decrease in measured values from the expected intrinsic yield values. (b) TEY decay measurements, which were made with a 608 eV beam giving a maximum yield value of ~ 6.0±0.5. This value has been added to figure (a). Yield decay fit was performed using Eqs. 2.21 and 2.22.

charge for each measurement and assuming that no charge is dissipated over the duration of the tests. This is contrasted against a yield versus incident charge curve in Fig. 4.21.

When graphed versus incident charge, the TEY data asymptotically approaches one for large amounts of incident charge. On the other hand, when graphed versus deposited charge the horizontal spacing of the data points gets smaller and smaller as the yield approaches one because the amount of net charge deposited gets smaller. Because the sample is a very good insulator, it acts more like an ideal capacitor with no leakage current through the sample. This gives a set surface voltage for a given amount of incident charge, and it produces a graph, that is shaped very similar to the data collected during a DC spectra test. The biggest difference, however, is that TEY versus deposited charge graphs never cross the yield of one because they reach an equilibrium state where no more charge is deposited. In DC spectra tests, the collector current (which is proportional to TEY) is measured with progressively increasing grid bias voltages.

Hoffmann's yield versus incident charge model uses the emission spectra of the sample to determine what the yield would be after a certain amount of charge is deposited. However, Fig. 4.20(b) suggests that the reverse is also true; that is, it should be possible to use the yield versus deposited charge

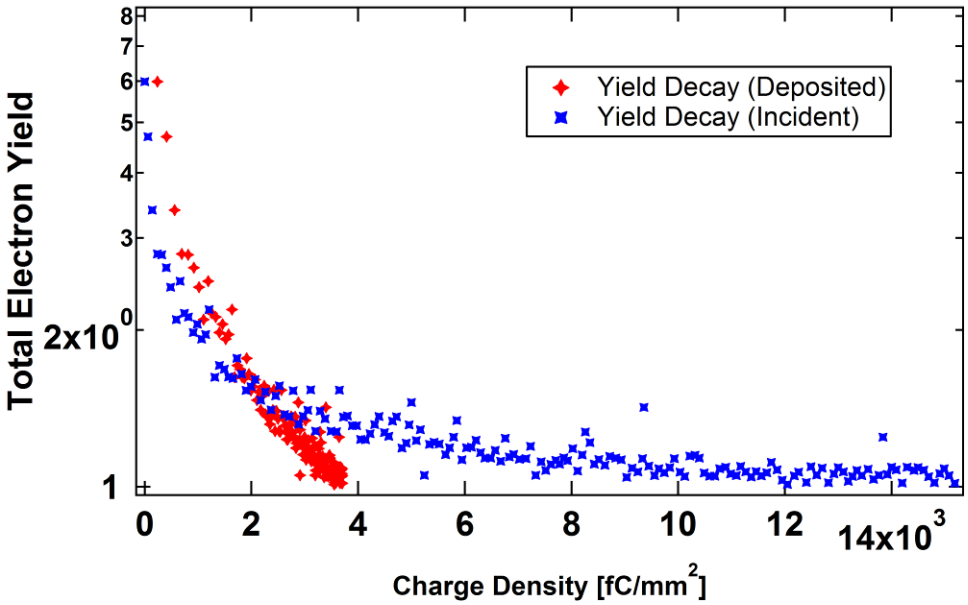

FIG. 4.21. Comparison of yield decay for incident and deposited charge. TEY for sapphire with a 608 eV incident beam is graphed versus incident (blue) and deposited (red) charge.

data to determine the emission spectra if the capacitance of the material is known. The resulting maximum yield (6.0±0.5), measured with the decay curve, has been added to Fig. 4.20(a) and the displayed fit has been adjusted to follow a better estimate of what the graph should look like.

Comparing these TEY data with Hoffmann's Al_2O_3 data shows some of the problems with each (see Fig. 4.22). On the low-energy, increasing end of the yield curves data the two sets of data disagreed on the slope of the curve. Hoffmann's data showed negative charging effects for incident electron energies $\leq 80\ eV$. In the positive charging region (~100 eV to 1500 eV) of both data sets there was also evidence of inadequate positive charge neutralization as evidenced by the added SEY fit using Eq. (2.15). Finally, the high-energy end of the data shows much better agreement. While the SEY fit is only physically related to SEY (δ), TEY (σ) is just the sum of δ and BSEY (η). Therefore, as long as $\eta << \sigma$ (which it is), then $\sigma \sim \delta$ and the model can still be used. The added fit is included as a best guess for what the intrinsic SEY values should be.

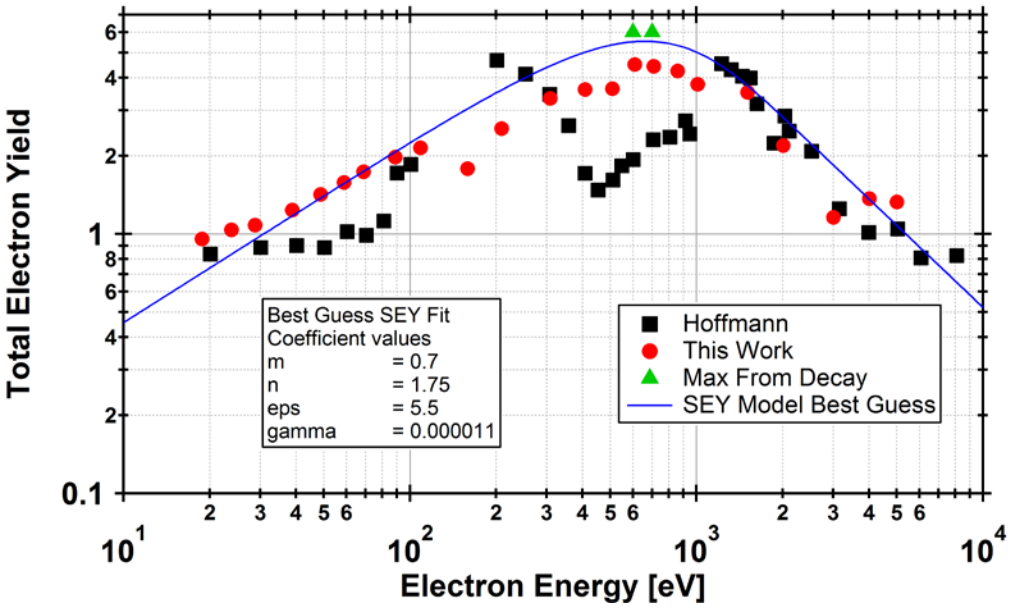

FIG. 4.22. Sapphire total electron yield comparison. Comparison of data taken here compared to previous data for sapphire (Hoffmann, 2010). A best guess of the SEY model is included with the model parameters. Shaded region shows the decrease in measured values from the expected intrinsic yield values.

4.3.4.2. Quartz (SiO_2)

Figure 4.23 shows the measured yield curve for a 2 mm thick quartz (SiO_2) sample (UQC Optics, FQW-102). This figure was graphed with linear yield and logarithmic energy axes. This demonstrates one

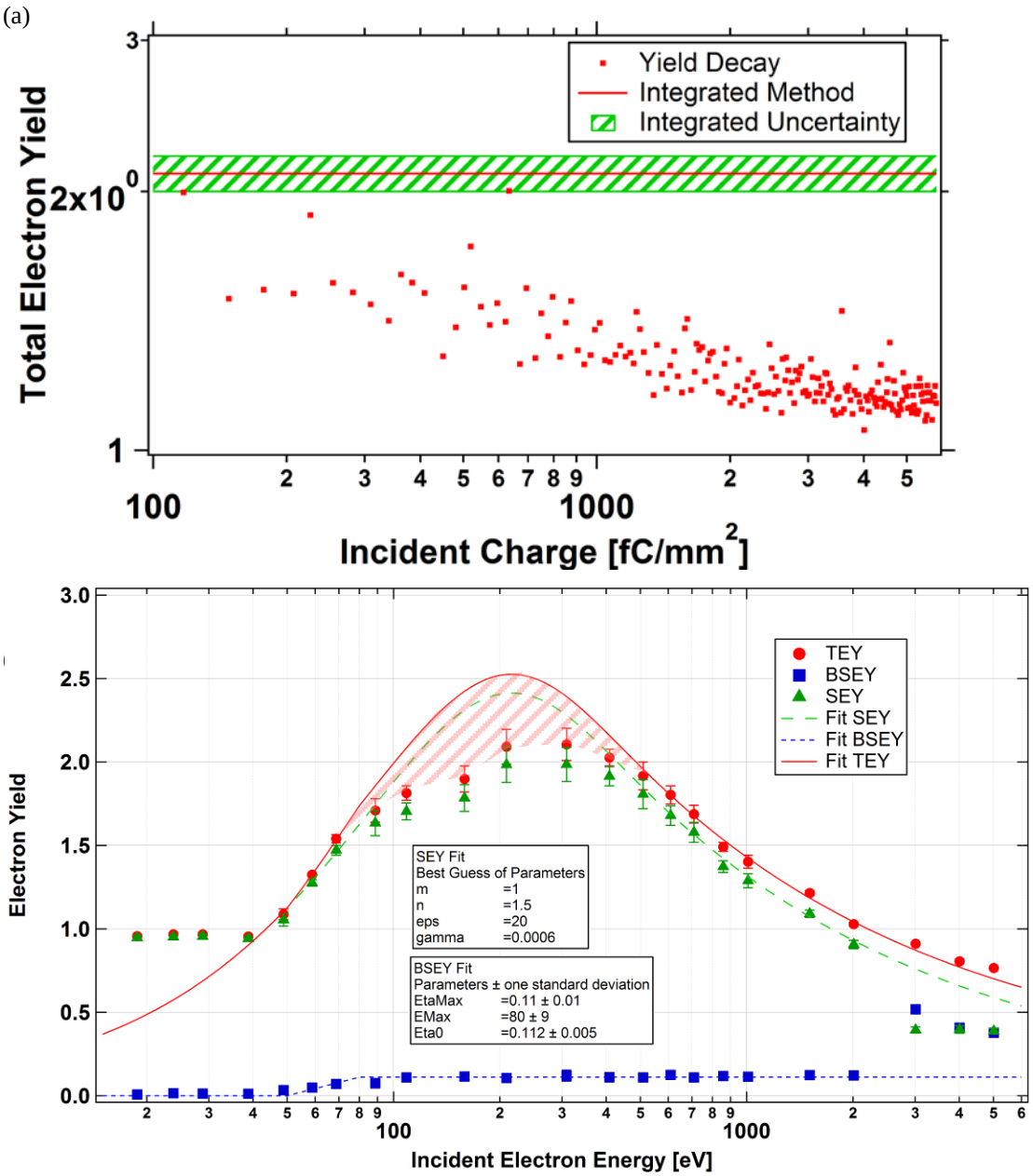

FIG. 4.23. Quartz yield results. (a) A yield decay curve for quartz SiO_2 with 308 eV incident electrons with added best-guess fit using the SEY model (Eq. 2.15) and a least squares fit using the BSEY model (Eq.2.19). (b) Lin-Log graph of quartz yield versus incident energy. It shows some evidence of negative charging at low and high energies. Shaded region shows the decrease in measured values from the expected intrinsic yield.

other way to portray yield curves. However, because the yield axis no longer uses logarithmic scale, the yield curves will not approximate straight lines in the low and high incident energy extremes. Using a linear yield axis also shows how small the BSEY measurements are compared to SEY and TEY. Below the first crossover of ~ 40 eV, there is evidence of negative charging resulting in a yield of unity. Also, above the second crossover of ~ 1500 eV, there is evidence of negative charge shifting some of the SE peak past the 50 eV definition point, abruptly reducing the SEY and increasing the BSEY measurements. To determine whether charging was occurring during the positive charging section of the curve, a yield decay curve was measured at 308 eV (see Fig. 4.23(a)). These data were taken with 10 *s* of UV and electron flooding between each pulse. As such the model described in Section 2.4 could not be used to model it. Because the curve still decays down to a constant value lower than the initial measurements, we conclude that there was some charging going on. The TEY value along with its standard deviation from Fig. 4.23(b) is included for comparison with the decay curve. The intrinsic yield plateau was not visible through the noise for these data, so it was difficult to tell how far below the true intrinsic yield value our measurements were.

4.3.4.3. PEEK (Polyether Ether Ketone)

When the yield tests were done on PEEK, at first, the resulting curves were hard to interpret (see Fig. 4.24(a)) due to apparent positive charging in the TEY curve. To get a better idea of what the maximum yield was, decay tests were done at 208 eV to try and see what the intrinsic yield was in the middle of the charged region of the graph (see Fig. 4.24(b)). Interestingly, the intrinsic yield plateau was easily seen in the decay graph. The first ~ 20 measurements were combined to give an average yield with a standard deviation at 208 eV. The expected SEY value was then calculated by subtracting the BSEY at 208 eV. Finally, a best guess for the intrinsic SEY curve was plotted, choosing coefficients that matched closely with uncharged regions of the yield curve and going through the intrinsic SEY point at 208 eV. Again, there was some charging at high energies, which lowered the SEY and increased the BSEY values. The amount of negative charging in this region must be very modest, since ~ 30-50 % of SEs have been given enough energy to penetrate through the ~ 50 V retarding field. Likewise, SEY at $E_0 < 50$ eV shows only modest charging indicated by the fact that low-energy yield do not return fully to unity.

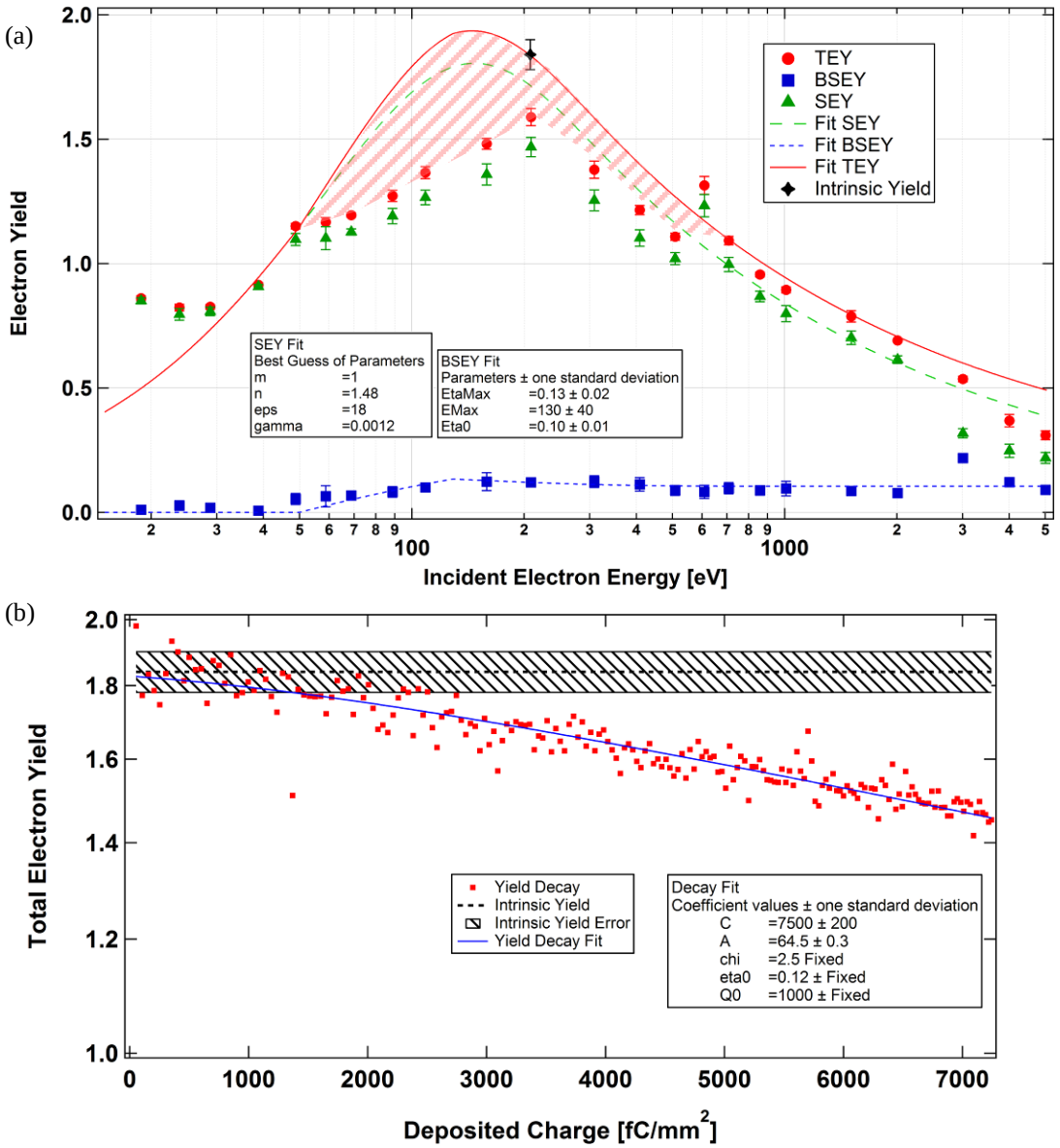

FIG. 4.24. PEEK yield results. (a) Measured yield curves for PEEK, with added best guess fit using the SEY model (Eq. 2.15), a least squares fit using the BSEY model (Eq.2.19), and the intrinsic yield values from the yield decay test. Shaded region shows the decrease in measured values from the expected intrinsic yield values. (b) Results from the yield decay analysis with 208 eV incident electrons. The shaded area is the average and standard deviation (1.84±0.06) of the first ~20 yield measurements before the curve starts to drop due to charging. The decay fit was done with Eqs. 2.21 and 2.22.

4.3.5. Low-Energy Yields

Since low-energy electrons are much more sensitive to sample charging, the final tests on charge neutralization examine how well the neutralization methods work on energies from 10 - 30 eV (see Fig. 4.25). These tests compare yield curves for BN (boron nitride) taken before (2013) and after (2015), the

improvements made in this work. There are two major differences between how these two data sets were collected and analyzed. First, the older data were taken before improvements were made to neutralization techniques and signal noise problems. Second, older data were analyzed using the LabView routines, which did not remove oscillating noise; while the newer data was analyzed using the sine fit noise removal discussed in Section 3.3.2. The biggest improvements in the data are seen in negative charging regions of the curves at low and high energies. This is especially true for energies below E_1. Before the improvements were made, the uncertainty at these low energy points was ~±30%, whereas afterwards it was reduced to better than ±10 %. Also, charging that occurred in the old data caused the yield values to be incorrectly measured as ~1 below E_1 and above E_2, while later data showed measurements as low as 0.35 at 20 eV. The data taken in 2015 had an anomalous data point at 300 eV that consistently occurred independent of material being measured. It was later determined to be caused by poor electron gun settings. Better settings were found and this problem was eliminated in subsequent tests. This graph also does an excellent job at demonstrating the decline in our yield measurement capabilities between Hoffmann's work (Hoffmann, 2010) and the beginning of this work. Most of this decline was caused by poor maintenance of the SEEM

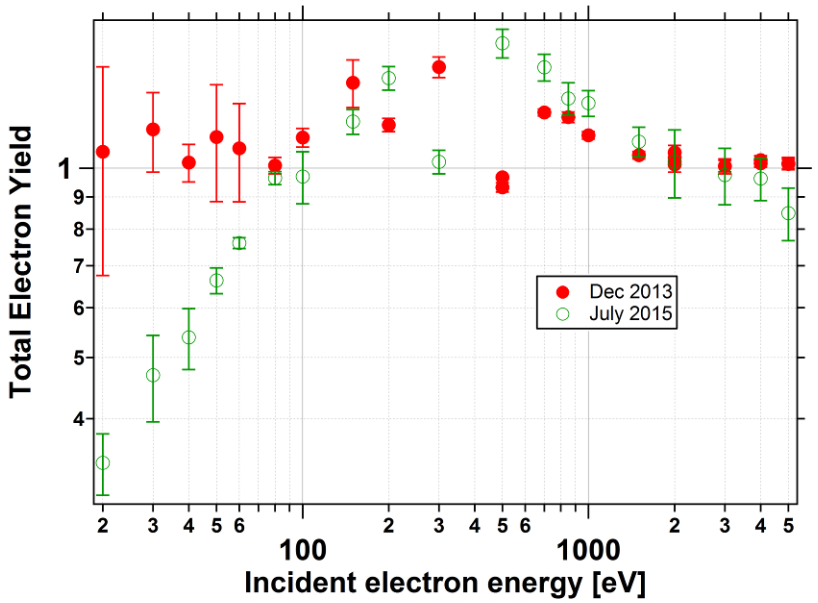

FIG. 4.25. BN yield curve comparison. BN TEY data taken before (2013) and after (2015) improvements were made to the system. Note differences at low energies. Also, these data were taken before the 8.8 eV offset was discovered.

test chamber and wear that comes with use over time.

4.4. Material Properties

This section summarizes important properties of the materials tested in this chapter. These properties are included to help understand some of the differences that were seen in yield measurements earlier in this chapter, as well as to summarize the results of the various yield tests. These properties include: measured yield parameters (E_{max}, σ_{max}, E_1, and E_2), band gap, conductivity, and electron range parameters (see Table 4.5, Table 4.6, and Figs. 4.26 and 4.27).

The band gap is important to these studies because it is assumed that UV neutralization will only work for materials where the band gap is lower than the photon energy of 4.9 eV. Figure 4.26 shows optical transmission spectra for some of the samples studied in this thesis. These spectra show a rough estimate of the band gap of the material when the transmission drops for photon energies greater than the band gap. Conductivity affects the time necessary for a charged sample to discharge without neutralization techniques.

Table 4.5. Measured material properties.

Material	Band Gap (eV)	Conductivity $(\Omega\cdot cm)^{-1}$	σ_{max}	E_{max} (eV)	E_1 (eV)	E_2 (eV)	References
Au	0	$4.4\cdot10^{5}$	2±0.2	700 ±30	45 ±3	6000 ±500	
HOPG	≤ 0.05	$2\cdot10^{4}$ (interplanar) $2\cdot10^{1}$ (intraplanar)	1.39 ±0.08	220 ±40	59 ±10	700 ±100	(Corbridge, 2003)
Polyimide	2.3	$8\pm3\cdot10^{-20}$	2.3 ±0.2	300 ±50	30 ±2	1200 ±50	(Gillespie, 2013)
PEEK	3.4	$5\pm2\cdot10^{-20}$	1.8 ±0.1	140 ±50	41 ±3	750 ±20	(De Albuquerque, *et al.*, 2007; King, 2017)
h-BN (hexagonal)	6.8	$2\cdot10^{-17}$	1.6 ±0.2	350 ±50	90 ±5	250 ±30	(Carpenter and Kirby, 1982; Frederikse, *et al.*, 1985)
Al_2O_3(Sapphire)	8.7	$3\pm1\cdot10^{-16}$	6.0 ±0.5	650 ±50	28 ±2	4000 ±500	(Hoffmann, 2010)
SiO_2(Quartz)	8.9	$6\pm2\cdot10^{-14}$	2.2 ±0.1	250 ±50	45 ±3	2100 ±100	(Strehlow and Cook, 1973; Dennison, *et al.*, 2016b)

Table 4.6. Range parameters for tested materials. Coefficients correspond to Eq 2.9.

Material	$b_1 \cdot 10^{-2}$ [μm/eV]	n_1	$b_2 \cdot 10^{-7}$ [μm/eV]	n_2
Au	2.63 ± 0.01	-0.957 ± 0.006	3.54 ± 0.02	1.5426 ± 0.0006
BN	2.28 ± 0.01	-0.944 ± 0.007	3.096 ± 0.006	1.6972 ± 0.0002
HOPG	1.86 ± 0.01	-0.942 ± 0.008	2.849 ± 0.005	1.7000 ± 0.0002
Kapton	1.24 ± 0.01	-0.93 ± 0.01	3.182 ± 0.005	1.7247 ± 0.0002
PEEK	1.28 ± 0.01	-0.93 ± 0.01	3.135 ± 0.005	1.7309 ± 0.0002
Quartz	2.80 ± 0.02	-0.949 ± 0.008	3.94 ± 0.01	1.6589 ± 0.0003
Sapphire	3.41 ± 0.01	-0.953 ± 0.005	3.128 ± 0.009	1.6516 ± 0.0003

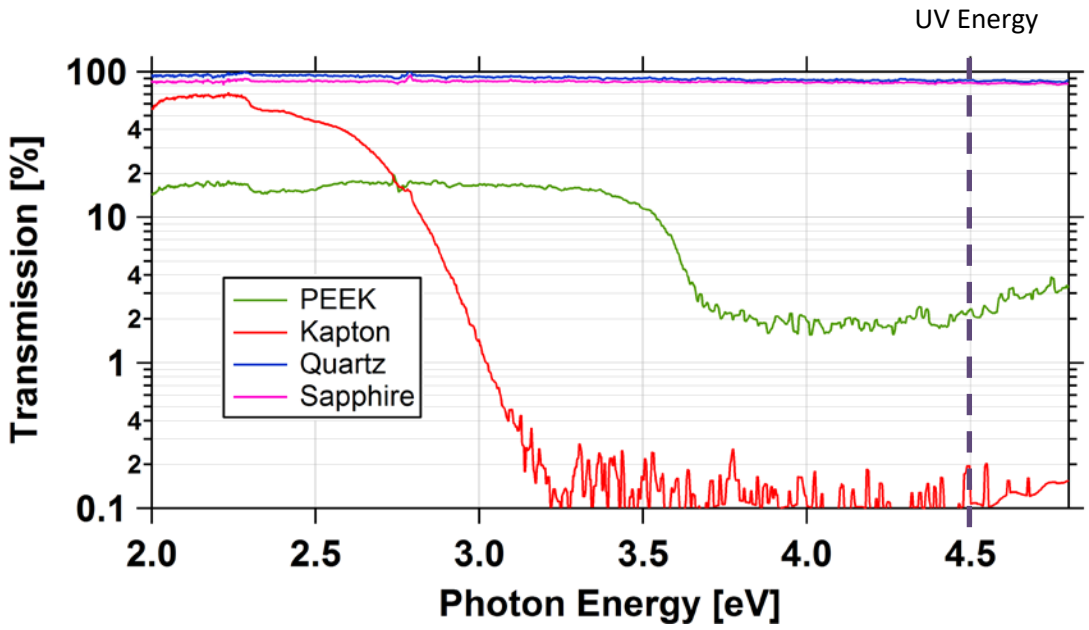

FIG. 4.26. Transmission spectra of materials. Transmission curves demonstrating the approximate band gap energies of materials studied in this thesis. Band gaps above the energy of our UV photons are expected to have more problems with negative (and possibly positive) charge neutralization.

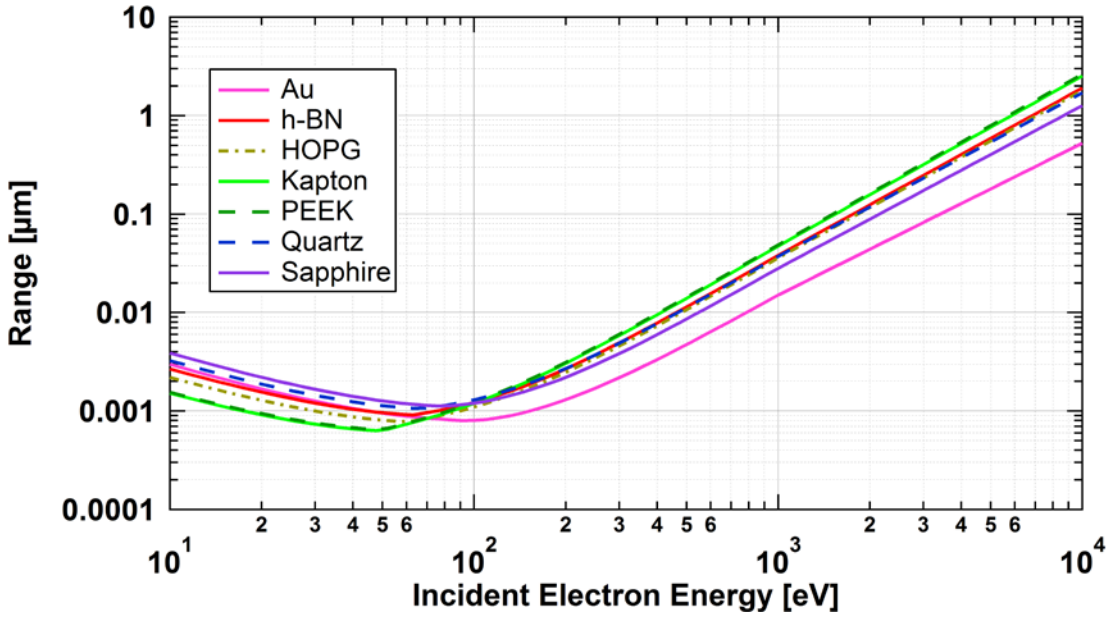

FIG. 4.27. Electron range curves for studied materials. Predicted range versus incident electron energy curves were found using Wilson's range model (Wilson and Dennison, 2012).

CHAPTER 5

CONCLUSIONS AND FUTURE WORK

In this chapter, the main points of this work are summarized, potential applications of the findings are discussed, and future work is proposed. In the summaries section, the improvements that this work has provided to our understanding of electron emission processes are discussed, as well as interesting findings and problems that were encountered. In the future work section, instrumentation upgrades are suggested, as well as topics that would be interesting to study further with the added capabilities developed. This section also explains how the results of this study may apply to other areas of physics and technology.

5.1. Summary of Work

The goal of this work was to validate and quantify the changes and upgrades that have been made to the USU MPG insulator yield-measurement system. These modifications included noise reduction, lower charge measurements, improvements to electron flooding and UV charge neutralization method, and higher quality analysis methods. Results of these improvements are summarized in Table 5.1.

Noise Reduction

Because of the intricate electronics needed to run the system, there were many possible sources of noise. This was made more challenging by the use of custom low-current, high-speed amplifiers (Thomson, 2005) and the versatile open architecture of the multi-sample carousel. Some of these noise sources were found to be caused by accidental grounding loops, intermittent shorts, loose wiring, and using instruments that created electromagnetic induction in other parts of our system. Because of these findings, upgrades were made to UV LED and flood gun grounding and mounting (see appendices B and E and Section 3.1.4.3), as well as other electrical connections to the HGRFA (see Section 3.2.5). These instrumentation upgrades lowered the worst-case system noise levels such that precision of typical individual yield measurements was reduced from about 30% to 10% (see Section 3.3.2). Averaging of 10-20 independent yield pulses at a given energy results in lowering the SDOM from ~10% to ~3%.

Table 5.1. Effects of measurement and analysis modifications.

Improvement Topic	Improvement	Predicted Effects of Improvement	Results
Pulse Duration	Pulse duration decreased from 5 μs to 3 μs.	Yields for <60% of previous incident charge and optimal pulse shape.	While it was possible to reduce the pulse duration, the rise time of the ammeters was not fast enough to see the correct width with the gain settings used.
Inner Grid Biasing	Inner grid biasing capability was added, with bias grid and collector floating on the inner grid bias.	Improved detection for high surface potentials.	Simulations and tests showed that to overcome sample surface voltage due to charging, an equivalent voltage bias is required on the inner grid and the sample aperture (stage). However, when the sample aperture is grounded, fringe fields between it and the sample modify the measured emission current and energies and no level of inner grid biasing can compensate for it.
HGRFA Ground Loops	Externally grounded flood gun and UV circuits reducing noise.	Signal-to-noise ratio reduced two to five times.	Noise levels were reduced from a worst case of ~30% to ~10% or by a factor of ~3.
UV Neutralization	UV LED wavelength reduced from 290 nm to 255 nm. Higher intensity UV LED used.	Improved negative charge neutralization.	For materials with small band gaps, the UV LED sped up the charge neutralization rate. However, its placement on the HGRFA illuminated only part of the sample because of the beam drift tube shadow. Measurements made on many materials showed much less negative charging below E_1 and above E_2. Most effective neutralization is limited to materials with band gaps below the UV energy of 4.9 eV.
Electron Flooding for Positive Charge Neutralization	Replaced W filament with Ta disk flood gun filament.	Improved positive charge neutralization. More stable emission current for lower noise and incident energies.	10 s of flooding was found to be adequate for discharging most materials. Yields $\sigma < 2.5$ were measured without too many charging problems. However, above this, electron flooding did not remove enough charge to keep up with the rate of charging.
Yield Calculation Method	Created analysis methods to remove oscillating noise and perform point-wise yield calculations.	Reduce noise level and measure yields for <1% of total incident charge.	The intrinsic yield plateau was not able to be measured using this method due to the picoammeters lacking the short response time necessary for this. This is seen in point-wise yield measurements of Au, which exhibited fluctuations over the course of a pulse and should not happen. Note: Might be contamination.
LabView Data Collection VI	Fixed a few LabView VI bugs to produce more useable data.	Better data for low charge measurements.	A few bugs were fixed with the LabView VI. This allows for more accurate incident charge measurements for the first pulse sent to the sample.
Yield Decays Extrapolated to Zero Deposited Charge	Reduced the amount of charging per measurement.	Direct measurement of intrinsic yield plateau in data.	For Kapton and PEEK, the intrinsic yield plateau was observed and measured. For quartz and sapphire, too much charging still occurred for direct measurement.

Further studies were performed to characterize the pulsed electron beam. The beam energy settings were found to produce beam energies 8.8±0.3 eV higher than expected (see Section 4.1.2). Therefore, all data were adjusted to account for this energy offset. The beam widths were then measured for all electron gun settings to determine the settings that produced the best beams for our measurements (see Section 4.1.1).

Lower Incident Charge Measurements

By reducing the pulse length from ~ 5 μs to ~ 3 μs, noise from ~ 30 % to 5 %, and using fast low-current measurement techniques, we are not only able to measure extremely small currents (25 nA - 150 nA reached using a gain of 2×10^7 V/A), but on very small time scales (4 μs rise times). The picoammeters used for these tests have a range of gain settings ($2\times10^6\ V/A$ - $1\times10^8\ V/A$), which have response times between ~ 1 μs - 8 μs. The gain settings that were used were chosen because they gave the best response time without sacrificing too much gain. This limits how brief the electron beam pulses can be. Because the picoammeter response has to do with the resistance, capacitance, and inductance of each current path, any differences due to biasing batteries, cable length, etc. will produce different rise times and can also produce the ringing we saw in some of the signals. This makes it very hard to do the point-wise tests discussed in Sections 3.3.3 and 4.3.3.

Improved Charge Neutralization

Because of recent improvements in electron source (higher emission current and more uniform beam distribution) and UV LED (higher energy and greater intensity photo emission) technology (see Section 3.2.1), we can more efficiently neutralize charged insulators allowing us to measure the intrinsic electron yield of many high-yield, low-conductivity materials (see Section 4.3). This has allowed us to directly measure total electron yields as high as ~6 (increased from ~4.5 (Hoffmann, 2010)) on materials with resistivities as high as $5\ \cdot\ 10^{19}\Omega$cm.

Some materials have been shown to still produce difficulties with negative charging. Most of these are materials (e.g., Al_2O_3, SiO_2) with band gaps that are too large (>4.5 eV) for the UV photons to excite appreciable numbers of electrons into the conduction band or be photo emitted. The reasoning for this

conjecture is that charge dissipation will occur since: (i) UV light neutralizes negatively charged samples by giving bound electrons enough energy to overcome the electron affinity (band gap + work function) of the material through the photoelectric effect (photons with less energy than this will not deposit enough energy for excited electrons to escape and they will remain confined to the material), or (ii) UV light will excite valence electrons into the conduction band, initiating photoconductivity, which allows charge transport to dissipate accumulated charge.

It has also been found that for some materials, the use of UV flooding is adequate for neutralizing both negative and positive charge, and electron flooding is not needed. Our current explanation for why UV flooding might work for positive charge neutralization is that metal surfaces in the HGRFA release low-energy electrons through the photoelectric effect when subjected to UV radiation; this, then, would act like the low-energy flood gun electron source, sending electrons all over the HGRFA, which would be attracted by a positively charged sample. This is, however, still conjecture, and there is not yet evidence to confirm this explanation. It could also be caused by increased photoconductivity.

Improved Analysis Methods

New analysis techniques have also been implemented that allow for removal of linear and oscillating signal noise from the data (see Appendix C). It also allows large data sets to be processed in just a few minutes rather than hours; therefore, more data can be acquired and stochastic error can be reduced by combining the results of many tests. These analysis techniques reduced the noise levels even further to a worst case of ~ 5% precision for typical single pulse-yield measurements.

Also, switching from linear and semi-log plots to log-log plots has made it much easier to determine where problems with charging are occurring in the data. It has also made it easier to interpolate and predict the true intrinsic yield in regions where charging occurs (see for example, Figs. 4.20 and 4.24).

5.2. Future Work

5.2.1. Instrumentation Upgrades

Plans are already underway to make many upgrades to the systems that have been used in this work. The most exciting is the design and construction of a new HGRFA, which will utilize some design

changes to avoid—or at least minimize—many of the problems that have been discussed. The most notable differences in the new HGRFA design include:

(i) less potential for electrical problems with more robust electrical connections and better wire containment,

(ii) repositioning the flood gun and UV LED for better line-of-sight sample irradiation,

(iii) the ability to access internal parts of the HGRFA without completely dismantling it,

(iv) reducing grid asphericity, thereby improving the energy resolution,

(v) incorporate an *in situ* surface voltage probe,

(vi) implementation of capabilities for optical and photo-yield measurements, and more robust methods for making electrical connections to the various internal components (Wilson, 2017).

Because the sample carousel hangs on a rod suspended from the top of the chamber, weight imbalances and tension in attached cables cause the carousel to be pushed off of the center axis of the chamber. Plans have also been made to improve alignment issues by securing the carousel to the top and bottom of the chamber with a custom alignment fixture. This will make it easier to keep the HGRFA centered in front of the electron beam. Future work should also add capabilities to automate sample biasing (see Fig. 3.3a).

By removing system noise, better characterizing the fast picoammeters (e.g., rise/fall times), better controlling beam settings and pulse duration, and the use of analysis techniques to filter out problems caused by overshoot and ringing in the circuitry, the possibility of doing point-wise yield measurements within a single oscilloscope pulse trace may be possible. Further work into fast, low-current measurements is also underway to improve upon the picoammeters used in this thesis. This may lead to the ability of point-wise total yield measurements to reduce the effective amount of charge used per measurement by a factor of ~25 (~3 *fC* to 18 *fC*). The electrometers used for data collection are currently being redesigned to have more sensitivity and faster response times. Cabling is being redesigned to minimize capacitance. New electron guns have been ordered, which have more flexibility in beam pulsing, with pulses from ~20 ns to 100 µs. Taken together, these changes will allow much shorter and better controlled beam pulsing.

This has the potential to allow yield measurements with incident charges small enough to see the low-charge yield plateau for difficult high-yield, low-conductivity materials such as quartz (SiO_2) and

sapphire (Al_2O_3) (see Section 4.3.4), which is predicted by our yield versus incident charge model (Hoffmann, 2010) and has been measured for lower resistivity materials. This will allow the direct measurement of the intrinsic (uncharged) yield of these difficult insulators. While there are still some problems with overshoot in the oscilloscope traces that prevent this method from producing true results, the software is in place to make these kinds of measurements once ringing in the current versus time oscilloscope trace data is accounted for.

Many of the difficulties encountered in this thesis were caused by the fact that sometimes (especially in academic research), you have to make do with what you already have. An example of this is that the electron gun, which was used for these measurements, was not designed to work at such low energies, nor was it meant to produce wide beams at large energies. Because of the high interest that exists in low-energy yield measurements, a lower energy electron gun would allow the USU MPG to stay on top of the field. Future work into automating the electron gun would also vastly improve our measurement capabilities, enhance sample throughput, and improve measurement precision.

5.2.2. Future Applications

By gaining a better understanding of how material properties affect electron yield, new materials can be created to meet design requirements for these types of studies. For example, low-yield materials are good for situations when you want to absorb stray electrons such as in particle accelerators and microwave communications or multipactor applications (Olano, *et al.*, 2017), while high-yield materials are great for applications such as photomultiplier tubes.

5.2.3. Proposed Experiments with the HGRFA

Since SEs and BSEs can be defined through their origin (either in the sample or the beam), or by their energy (less than or greater than 50 eV, respectively), for incident energies less than 50 eV there can be confusion over how to define them (Kite, 2007). Experiments measuring the emission energy spectrum for low incident energies would be very interesting and useful. Multipeak fits to energy spectra may produce better models that preserve the definition of true BSEs below 50 eV and better validate both SE and BSE models for these low energies, since measured SEY values are calculated using the BSEY.

Other applications include:

- Experiment more with IG bias and the *in-situ* surface voltage probe to improve the field-free region around the sample.
- Study the effects of sample bias on yield.
- Use simultaneous yield and surface voltage measurements.
- Measure the intrinsic yield plateau to confirm Hoffmann's model.
- Mount the HGRFA on a cold stage to study temperature effects on yield.
- Extend MPG SEY database with yield information of more materials.
- Make higher energy resolution and lower incident energy measurements for the study of multilayer and contaminated material yields.

REFERENCES

Andronov, A. N., A. S. Smirnov, I. D. Kaganovich, E. A. Startsev, Y. Raitses, and V. I. Demidov, 2013, CERN Yellow Report CERN-2013-002, p.161-163.

Carpenter, L., and P. Kirby, 1982, "The electrical resistivity of boron nitride over the temperature range 700 degrees C to 1400 degrees C," J. Phys. D **15**, 1143.

Chang, W., J. Dennison, J. Kite, and R. Davies, "2000, Effects of evolving surface contamination on spacecraft charging," in *Proceedings of the 38th American Institute of Aeronautics and Astronomics Meeting on Aerospace Sciences*, Reno, NV.

Chang, W., N. Nickles, R. Davies, and J. Dennison, 1998, "Utah State University ground-based test facility for study of electronic properties of spacecraft materials," in *6th Spacecraft Charging Technology Conference*, Air Force Research Laboratory Science Center, Hanscom Air Force Base, MA.

Chen, Y., T. Kouno, K. Toyoda, and M. Cho, 2011, "Total electron emission yield measurement of insulator by a scanning small detector," Appl. Phys. Lett. **99**, 152101.

Chung, D., 2002, "Review Graphite," J. Mater. Sci. **37**, 1475-1489.

Chung, M., and T. Everhart, 1974, "Simple calculation of energy distribution of low-energy secondary electrons emitted from metals under electron bombardment," J. Appl. Phys. **45**, 707-709.

Corbridge, J., 2003, "Secondary electron emission study of annealed graphitic amorphous carbon," Senior thesis, (Utah State University).

Davies, R., and J. Dennison, 1997, "Evolution of secondary electron emission characteristics of spacecraft surfaces," J. Spacecraft and Rockets **34**, 571-574.

De Albuquerque, J., E. Tavenner, M. Curry, R. Giedd, and P. Meredith, 2007, "Determination of thermal and optical properties of ion implanted polyetheretherketone films by photothermal spectroscopies," J. Appl. Phys. **101**, 054506.

Dennison, J., 1985, "(e, 2e) Spectroscopic Investigations of the Spectral Momentum Densities of Thin Carbon Films," Ph.D. dissertation (Virginia Tech).

Dennison, J., A. Chang, C. Thomson, J. Kite, J. Corbridge, and C. Ellsworth, 2001, "Final Report Part III: Additional Materials Reports," NASA Space Environments and Effects Program Grant.

Dennison, J., *et al.*, 2016a, "Absolute Electron Emission Calibration: Round Robin Tests of Au and Polyimide," in *14th Spacecraft Charging Technology Conference*, Noordwijk, The Netherlands.

Dennison, J., J. Corbridge Gillespie, A. Andersen, A. Evans Jensen, G. Wilson, J. Dekany, A. Sim, and R. C. Hoffmann, 2016b, "Synergistic models of electron emission and transport measurements of disordered SiO_2," in *14th Spacecraft Charging Technology Conference*, Noordwijk, The Netherlands.

Dionne, G. F., 1975, "Origin of secondary-electron-emission yield-curve parameters," J. Appl. Phys. **46**, 3347-3351.

Frederikse, H. P., A. Kahn, A. L. Dragoo, and W. Hosler, 1985, "Electrical resistivity and microwave transmission of hexagonal boron nitride," J. Am. Ceram. Soc. **68**, 131-135.

Gillespie, J., 2013, "Measurements of the temperature dependence of radiation induced conductivity in polymeric dielectrics," Master's thesis (Utah State University).

Gineste, T., M. Belhaj, G. Teyssedre, N. Balcon, and J. Puech, 2014, "A novel experimental setup for the measurement electron backscattering yield," Meas. Sci. Technol. **25**, 085601.

Hastings, D., and H. Garrett, 1996, *Spacecraft-environment interactions*, (Cambridge University Press, Cambridge, UK).

Hoffmann, R. C., 2010, "Electron-induced electron yields of uncharged insulating materials," Master's thesis (Utah State University).

Jensen, A. E., 2014, "Modeling the defect density of states of disordered SiO_2 through cathodoluminescence," Master's thesis (Utah State University).

Katz, I., D. Parks, M. Mandell, J. Harvey, D. Brownell Jr., S. Wang, and M. Rotenberg, 1977, "A three dimensional dynamic study of electrostatic charging in materials," Technical Report NASA CR-135256.

King, D., 2017, "Measuring and modeling the conductivity of highly insulating materials," Senior thesis (Utah State University).

Kite, J., 2007, "Secondary electron production and transport mechanisms by measurement of angle-energy resolved cross sections of secondary and backscattered electron emission," Ph.D. dissertation (Utah State University).

Lane, R., and D. Zaffarano, 1954, "Transmission of 0-40 keV electrons by thin films with application to beta-ray spectroscopy," Phys. Rev. **94**, 960.

Lin, Y., and D. C. Joy, 2005, "A new examination of secondary electron yield data," Surf. Interface Anal. **37**, 895-900.

Mandell, M. J., V. A. Davis, D. L. Cooke, A. T. Wheelock, and C. Roth, 2005, "Nascap-2k spacecraft charging code overview," in IEEE Transactions on Plasma Science **34**, 5, p. 2084-2093.

Montero, I., L. Aguilera, L. Olano, M. E. Dávila, V. Nistor, L. Galán, J. Dennison, and G. Wilson, 2016, "Extremely Low Secondary Electron Emission from Metal/DielectricParticulate Coatings," in 14th Spacecraft Charging Technology Conference, Noordwijk, The Netherlands

Nickles, N. E., 2002, "The role of bandgap in the secondary electron emission of small bandgap semiconductors: Studies of graphitic carbon," Ph.D. dissertation (Utah State University).

Olano, L., I. Montero, M. E. Dávila, and J. Dennison, 2017, "Dynamic secondary electron emission in dielectric/conductor mixed coatings," International Workshop on Multipactor, Corona and Passive Intermodulation (MULCOPIM), ESA/ESTEC **9**.

Seiler, H., 1983, "Secondary electron emission in the scanning electron microscope," J. Appl. Phys. **54**, R1-R18.

Staib-Instruments, 2002, *Instruction Manual Electron Gun Model Ek-5-S*, Staib Instruments, Williamsburg, VA.

Strehlow, W., and E. Cook, 1973, "Compilation of energy band gaps in elemental and binary compound semiconductors and insulators," J. Phys. Chem. Ref. Data **2**, 163-200.

Terrill, H. M., 1923, "Loss of velocity of cathode rays in matter," Phys. Rev. **22**, 101.

Thomson, C., V. Zavyalov, and J. Dennison, 2003, Instrumentation for studies of electron emission and charging from insulators," in *8th Spacecraft Charging Technology Conference*, NASA Marxhall Space Flight Center, Huntsville, AL.

Thomson, C. D., 2005, "Measurements of the secondary electron emission properties of insulators," Ph.D. dissertation (Utah State University).

Viatskin, A., and A. Makhov, 1958, "Retardation of electrons in some metals and semiconductors," Sov. Phys. Tech. Phys. **3**, 690-696.

Whiddington, R., 1912, "The transmission of cathode rays through matter," in *Proceedings of the Royal Society of London. Series A, Containing Papers of a Mathematical and Physical Character* **86**, 360-370.

Wilson, G., 2017, "Hemispherical Grid Retarding Field Analyzer Redesign for Secondary Electron Emission Studies," in *23rd Annual Fellowship Symposium Utah NASA Space Grant Consortium*, Weber State University, Ogden, UT.

Wilson, G., and J. Dennison, 2012, "Approximation of range in materials as a function of incident electron energy," IEEE Transactions on Plasma Science **40**, 291-297.

Young, J., 1956, "Penetration of electrons in aluminum oxide films," Phys. Rev. **103**, 292.

APPENDICES

APPENDIX A

STAIB GUN PULSED BEAM SETTINGS

When trying to determine the appropriate STAIB gun control settings, it was found that the beam was not being completely blanked between pulses. While the current was much smaller between pulses, the amount of time between pulses made the deposited charge large enough that it would cause sample charging. Using information in the STAIB gun manual under the pulsed-mode section, it was determined that the grid settings we were using were too low (Staib-Instruments, 2002).

The pulsed mode of the STAIB electron gun works in the following manner. Normally the amount of electrons that are let out of the gun is controlled by adjusting the grid voltage. Higher grid voltages suppress more electrons, until at some point the grid voltage is set above a specific cut-off voltage and virtually no electrons pass through the grid. A 5 V TTL signal from a pulse generator to the STAIB gun controller triggers the power supply to drop the grid voltage by a specific amount. This voltage drop is not adjustable, so the grid voltage needs to be set at a value above the cut-off voltage, but low enough that when a pulse trigger comes into the controller, this drop brings it to the desired voltage and allows appreciable current to be emitted.

Procedure

To characterize the beam, a Faraday cup (FC) was placed in front of the gun and the collected currents were measured by the picoammeters in the yellow patch panel. Details of the FC design and use are given in Hoffmann (Hoffmann, 2010). The pulse generator (Tektronix Type 115) was put in gated mode with a 5 V bias from a power supply (Agilent E3647A) going into the + GATE IN, BNC connection. The gated mode sends a constant stream of pulses with a set period (typically 100 μs period for these tests) between each pulse; the shape of each pulse is determined by the pulse-width setting and rise and fall time settings of the pulse generator. To estimate the best settings, the following steps were taken:

1. Start with best guess of beam settings over the FC.
2. Center the beam over the FC by adjusting the deflection knobs on the STAIB gun control box until the FC current is maximized.

3. Adjust focus to maximize the FC to tertiary current ratio. (This makes the beam smaller.)
4. Check the grid settings to make sure that current goes to zero between pulses.
    a. Turn pulse generator mode switch to Burst.
    b. Turn switch on STAIB controller unit to Internal.
    c. Clear graph and reset offset on the LabVIEW program (IESBD_DC Profiler v1.6.vi).
    d. While switching back and forth between Internal/External modes on the Staib gun controller, no change in FC current should be noticed. This can be a little tricky to see because of the noise in the ammeters which causes the currents to fluctuate a little bit. A good method is to switch between Internal/External every 4 s to produce a regular pattern of ups and downs in the signal, which can be distinguished over the random fluctuations created by the noise.
    e. If the beam is not being blanked completely between pulses, increase the grid voltage until no fluctuation occurs while switching between Internal/External.
5. Double check that the LabVIEW offset settings are correct by blanking the beam and pressing Offset, under the functions tab.
6. Take beam profile data to record settings and results.

Figure A.1 shows plots of the filament current, grid voltage, focus voltage, and resulting beam width, all as a function of beam energy. Note that the X- and Y- deflection settings vary for different sample positions. The deflections, as listed, are small and these deflections are even smaller after the addition of the carousel positioning rod. The results from these tests and the settings used throughout this thesis are given in Table A.1.

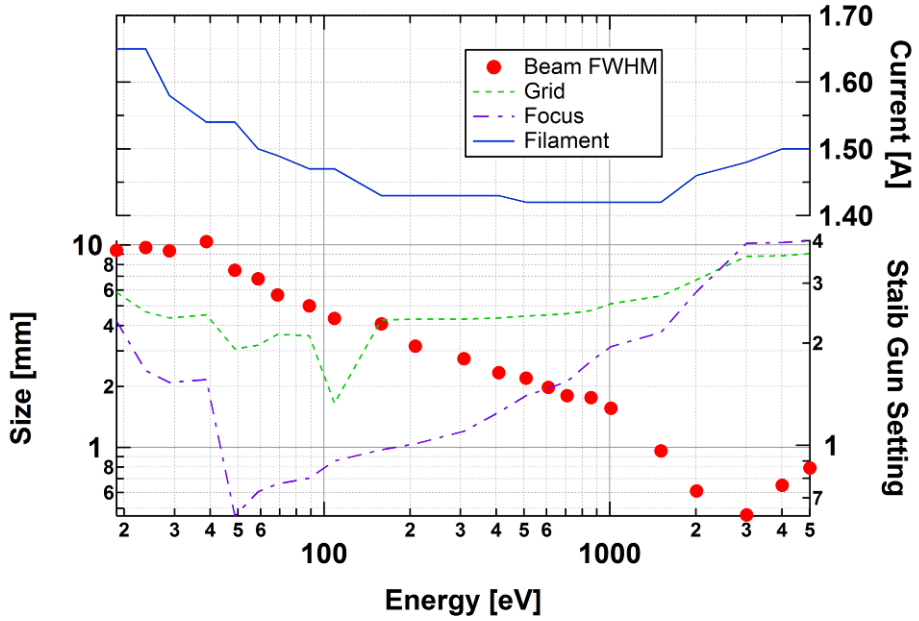

FIG. A.1. Staib gun settings and beam width. Graph shows beam settings used for all tests, and resulting beam widths. Beam energy is adjusted to account for systematic error offset (see Section 4.1.2).

Table A.1. Staib gun beam settings.

Energy [eV] Setting	Filament [A] Current	Grid [V]	Focus [V]	X-Deflect	Y-Deflect
10	1.65	2.82	2.32	0.008	-0.018
15	1.65	2.47	1.66	-0.008	0.008
20	1.58	2.37	1.53	0.000	0.010
30	1.54	2.42	1.56	0.010	0.018
40	1.54	1.92	0.62	0.012	-0.003
50	1.50	1.97	0.73	0.022	-0.002
60	1.49	2.12	0.77	0.020	0.003
80	1.47	2.10	0.80	0.040	0.004
100	1.47	1.33	0.90	0.063	0.009
150	1.43	2.34	0.97	0.114	0.012
200	1.43	2.35	1.01	0.130	0.010
300	1.43	2.35	1.10	0.222	0.032
400	1.43	2.37	1.25	0.268	0.042
500	1.42	2.40	1.40	0.297	0.059
600	1.42	2.42	1.47	0.408	0.065
700	1.42	2.44	1.54	0.489	0.074
850	1.42	2.49	1.77	0.578	0.088
1000	1.42	2.61	1.95	0.624	0.115
1500	1.42	2.75	2.15	0.881	0.318
2000	1.46	3.07	2.83	1.23	0.508
3000	1.48	3.60	3.93	1.82	0.840
4000	1.50	3.61	3.95	2.39	1.17
5000	1.50	3.66	4.00	2.85	1.55

APPENDIX B

ELECTRON FLOOD GUN MODIFICATIONS

Modifications were made to improve functionality of the low-energy electron flood gun, which is used to neutralize positive sample charge. These modifications improved the current output of the gun, as well as simplified its assembly to help minimize the chances of breaking the filament during assembly. Details of the original electron flood gun design are found in Hoffmann (Hoffmann, 2010) and Thomson (Thomson, 2005). These improvements are discussed below.

Filament Upgrade

The previous electron source used was a simple tungsten (W) filament (Kimball Physics, ES-020 filament on cb-104 base). A few problems were encountered with this source: it did not produce a stable current, the emission angular distribution was not well defined, and the filament burned out often (see Fig. B.1.).

The new electron source has a tungsten filament with a tantalum disk attached on the tip. The W filament provides indirect heating of the Ta disk; it is the Ta disk that produces the electrons in the electron beam. Because Ta has a work function of 4.1 eV compared to 4.5 eV for W, this filament has a larger current output at lower filament heating currents. This increased emission at lower emitter temperature increases the lifespan of the source, as well as allows for shorter charge neutralization times. Because the tantalum disk has a round flat surface and it is welded to the tungsten filament at a single spot, the surface

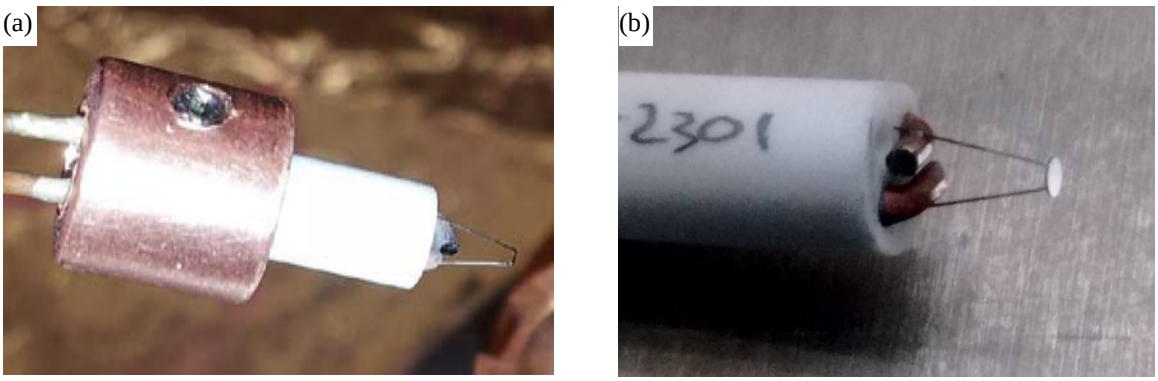

FIG. B.1. Flood gun source upgrade. (a) Old tungsten filament. (b) New tantalum disk filament.

potential of the disk is very uniform, which produces a very uniform electron distribution with very little energy uncertainty.

Gun Design Modifications

The previous gun design had a few problems, which caused it to regularly malfunction. The first problem was that the wire routing holes were too small and had sharp edges, which caused damage to wire insulation during assembly or disassembly. These tight holes also caused strain on the electrical connections inside the gun, which would cause them to break and short. The other major design flaw occurred when the filament was inserted and removed from the gun. In order to put the gun back together, the filament had to be inserted blindly into the gun and would easily catch on the edge of the extractor Wehnelt can and break.

To fix these problems the wire holes were enlarged and insulating sleeves were placed between the wires and the edges of these holes to protect the wires from any sharp edges. To fix the filament insertion problem, wiring for the extractor Wehnelt can was rerouted through the back of the gun so that the filament and Wehnelt can would be inserted and removed from the gun as one solid element (see Fig. B.2). This made it easier to position the filament inside the Wehnelt can; then the Wehnelt can acted as a shield to protect the filament when inserting the assembly into the gun.

After these modifications, the settings, which gave the best emission of low-energy electrons, were measured by putting the HGRFA over the FC and adjusting settings until the FC current was maximized. These settings are given in Table B.1.

Table B.1. Flood gun settings.

Flood Gun Settings			
Element	Current	Voltage	Notes
Filament	1.6 A	CW*	Voltage drifts. Current knob is more sensitive at high currents.
Wehnelt Can	NA	-1.5 V	
Suppression Grid	NA	8 V	Switch to Sup to see this voltage.
Emit Voltage	NA	0 V CW*	Switch to Emit to see this voltage.
Lens	NA	0V CCW*	Not readable without using a multimeter.

* Clockwise (CW) Counter Clockwise (CCW)

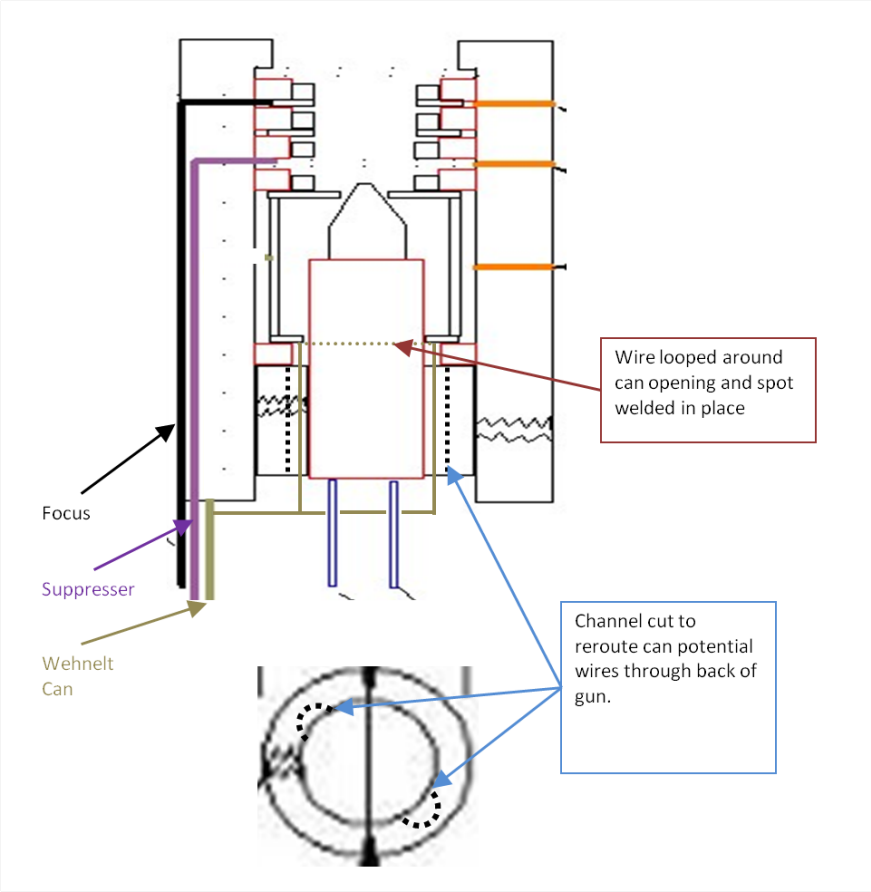

FIG. B.2. Flood gun wiring modifications. Figure shows changes made to Wehnelt can wiring and new channels cut in the filament block.

APPENDIX C

ELECTRON YIELD TOOLS V3.0.1

Electron Yield Tools V3.0.1 is an Igor Pro 6.37 procedure file designed as part of this thesis research. Its purpose is to provide a collection of electron yield analysis tools for the USU Materials Physics Group. It contains tools to easily:

- load data saved by the LabView yield data collection vi (Yield Pulse v4.vi, see Appendix D).
- Integrate the oscilloscope pulsed current data and convert to integrated charge.
- Combine integrated charge data to determine total or backscattered yield values.
- Create plots of pulse data, point-wise yield data, and yield versus energy data.
- Save yield versus energy data.

The following text gives a more thorough explanation of the options provided and instructions on how to analyze yield data.

Yield Tools Menu

The Igor PRO ElectronYieldTools_3-1-0 procedure file creates an additional menu at the top of the screen (see Fig. C.1). This Yield Tools menu contains menu and submenu items, which provide easy access to the analysis procedures. To learn how to make new menus, type menu in the command line, right

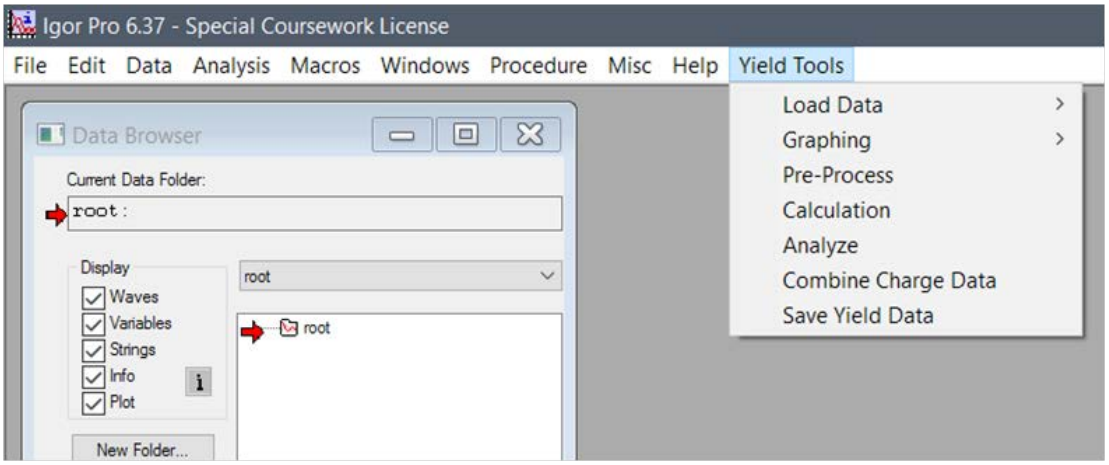

FIG. C.1. Screenshot of Yield Tools menu. Shortcuts to the yield analysis tools under the [Yield Tools] menu item are shown.

click on what you typed (menu), and select [help for menu].

The menu items are:

Load Data File

Load Waveform Data: This item contains two sub-items for loading oscilloscope traces saved by the LabView pulsed yield program. These files are saved as plain text files (.txt). Their first sub-item, Load Folder, allows the user to select a folder containing many of these files. Alternatively, the second option, Load Waveform Data, allows the user to load a single file at a time. This is useful if data has already been loaded and the user wants to retake any of the data points. Each option opens a file browser for the user to find the appropriate folder or file. Once the user clicks the Open button, Igor creates a folder to hold the waves, which are loaded and appropriately named. The naming convention for the loaded waves is: run + run number + sensor (i.e., run1sample). If there are many individual files that the user desires to load, a keyboard shortcut (ctrl+1) has been defined to access the load single file option more quickly.

Graphing

Display Graphs: This menu item displays the oscilloscope traces for each run in the current data folder. Note that in order for this to work, you must have the current data folder set to one of the data folders and not the root folder. (To do this, right click the folder with the data you want to graph and select Set Current DataFolder.)

Create Point-wise Plot: This menu item averages all the point-wise curves in the currently selected data folder and creates an averaged plot of the point-wise yield for the currently selected data folder. It also shows the standard deviation of the point-wise yield curves from the averaging done above. Note that the graph only makes sense for the duration of the pulse, so it produces a lot of noise to the left and right of the pulse. You will have to adjust the range of the graph in order to make it look pretty. Similar to the previous item, the data folder must be set to one that contains yield data. In addition, it does not work if the data have not been analyzed, because the point-wise data is calculated in the analysis step.

Clear Graphs: This menu item is given just for convenience. It is used to close all open graphs and tables in the Igor Pro work area. Note that it kills these windows without saving a window recreation

macro; if you care about any of the graphs in the window, close them manually and save a macro so you can open it later.

Pre-Process: This is where all the action happens. The Pre-Process menu begins the process for removing background noise and integration of each oscilloscope trace to determine the amount of charge deposited in each element of the HGRFA per pulse. When the user selects this option, a panel is displayed asking the user to select the zero method, which is desired. The two options are an option to average the points before and after the pulse, or to do a sine fit to these points. The Average option computes the average value for the noise (nonpulse) segments of individual oscilloscope traces and subtracts this value from the data. The Sine option does a fit to the noise segments of individual oscilloscope traces of the form $f(t) = A \cdot \sin(w \cdot t + \phi) + B \cdot t + C$. This is useful for removing periodic oscillations in the measured signals. This function is then subtracted from the oscilloscope trace.

After the user hits continue on this panel, graphs are displayed showing the oscilloscope traces and asking the user to select the regions that are used to define the beginning and end of the pulse, as well as the noise before and after the pulse. After the user selects these regions, the program performs the selected zeroing method on each oscilloscope trace and then performs the integrations to determine the charge per pulse.

Calculation: The Calculation menu item gives the user a method to alter the calculations that are used to combine the charges per pulse in each HGRFA element to produce a final yield value. When pressed, it displays a panel with check boxes and dropdown menus (see Fig. C.2). To calculate incident charge, the collector and sample currents are always used. However, to include the grid and stage currents there is a checkbox for each. Similarly, for the emitted charge calculation, the collector current is always used and there are also two checkboxes to include the grid and the stage in the emitted charge calculation.

The bottom section has a dropdown menu, which allows the user to pick between an averaging or a sine fit method to remove noise.

When the next, Analysis menu item is selected, if the user has not already set these options manually, the TempCalcPanel will be displayed in order to determine how the analysis should be done. After analysis has been done, these options may be changed and analysis can be redone with the new settings so that the

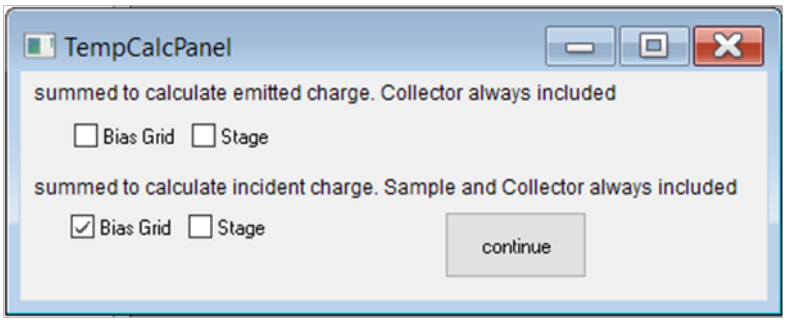

FIG. C.2. Calculation panel. The calculation panel is displayed by selecting the Calculation menu item. It allows the user to change how the yield is calculated by selecting checkboxes, and changing the zero method.

user does not have to reload all the data in a new Igor Pro experiment file. (It is a good idea to save the results of each analysis before reanalyzing the data because you will lose the previous results once this is done.)

Analyze: When this menu item is selected, each data folder is analyzed using the calculation settings (see previous menu item) to determine the average yield for each pulse, as well as the point-wise yield for each pulse. These data are then combined to give average yield for each data folder, as well as uncertainty in the form of a standard deviation of the mean. Lastly, the data from each data folder are combined in a graph showing the yield versus energy profile of the material.

Combine Charge Data: After the data have been analyzed, this tool combines all of the incident and emitted charge data from each folder and displays a graph with the incident and emitted charge statistics for each energy.

Save Yield Data: This menu item is used once analysis has been completed to save the yield versus energy data for the experiment. These data can then be used to create graphs containing multiple materials' yield data, or it can be used in the NASCAP fitting tool to determine the parameters in the NASCAP model.

The above process is represented graphically in Fig. C.3.

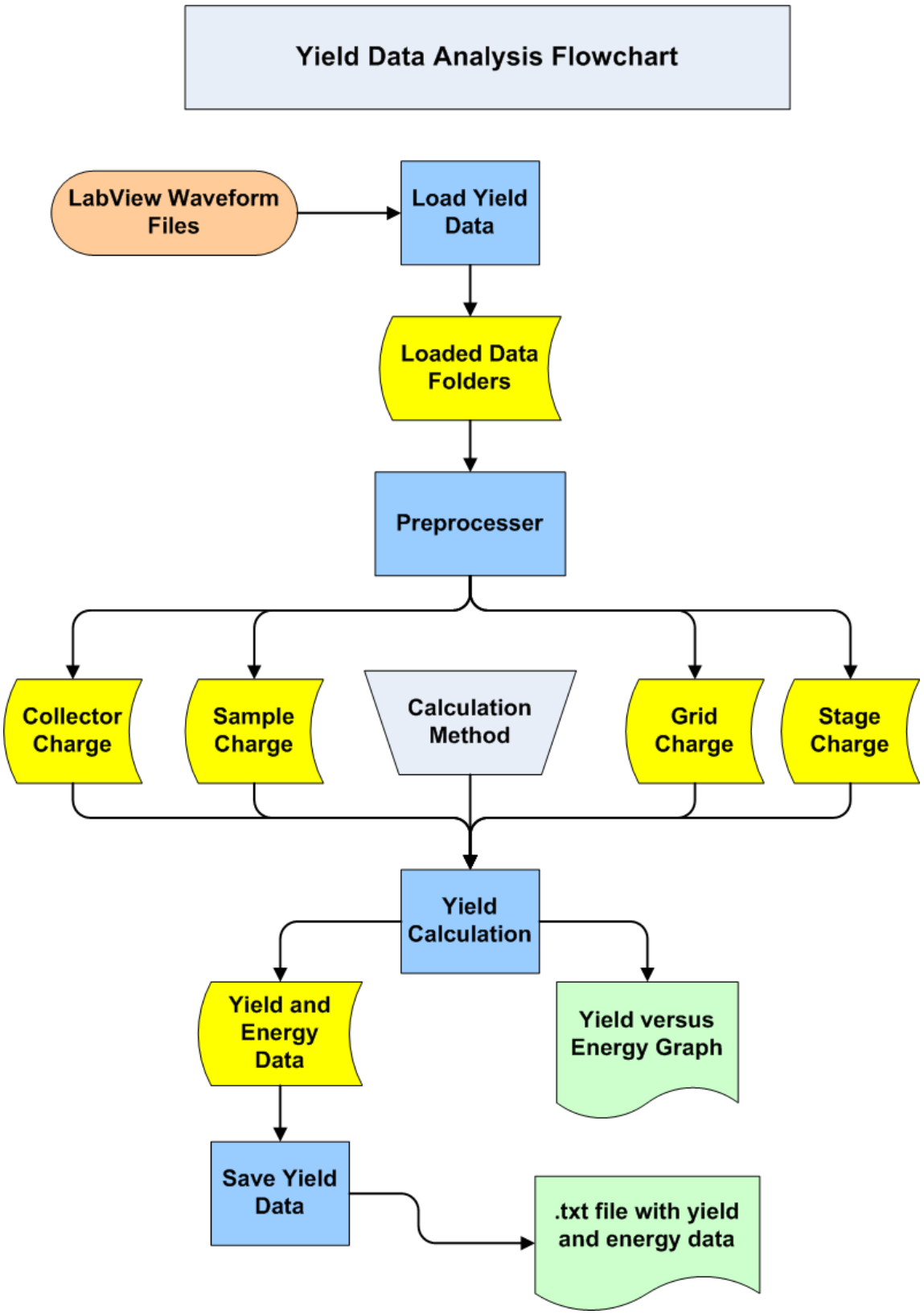

FIG. C.3. Yield data analysis flowchart. Work flow diagram of the Igor Pro yield analysis program.

APPENDIX D

LABVIEW VI FLOWCHARTS

Figure D.1 is a flow chart for the LabView vi used to collect pulse-yield data. The solid lines represent program flow, and dashed lines denote data flow. The flowchart does not show every detail of the program; however, it shows enough to understand how the program works. The blue, striped box shows the only change that was made during this work. This fixed a bug that caused the program to send a pulse before the oscilloscope was ready, causing the first data point to be garbage.

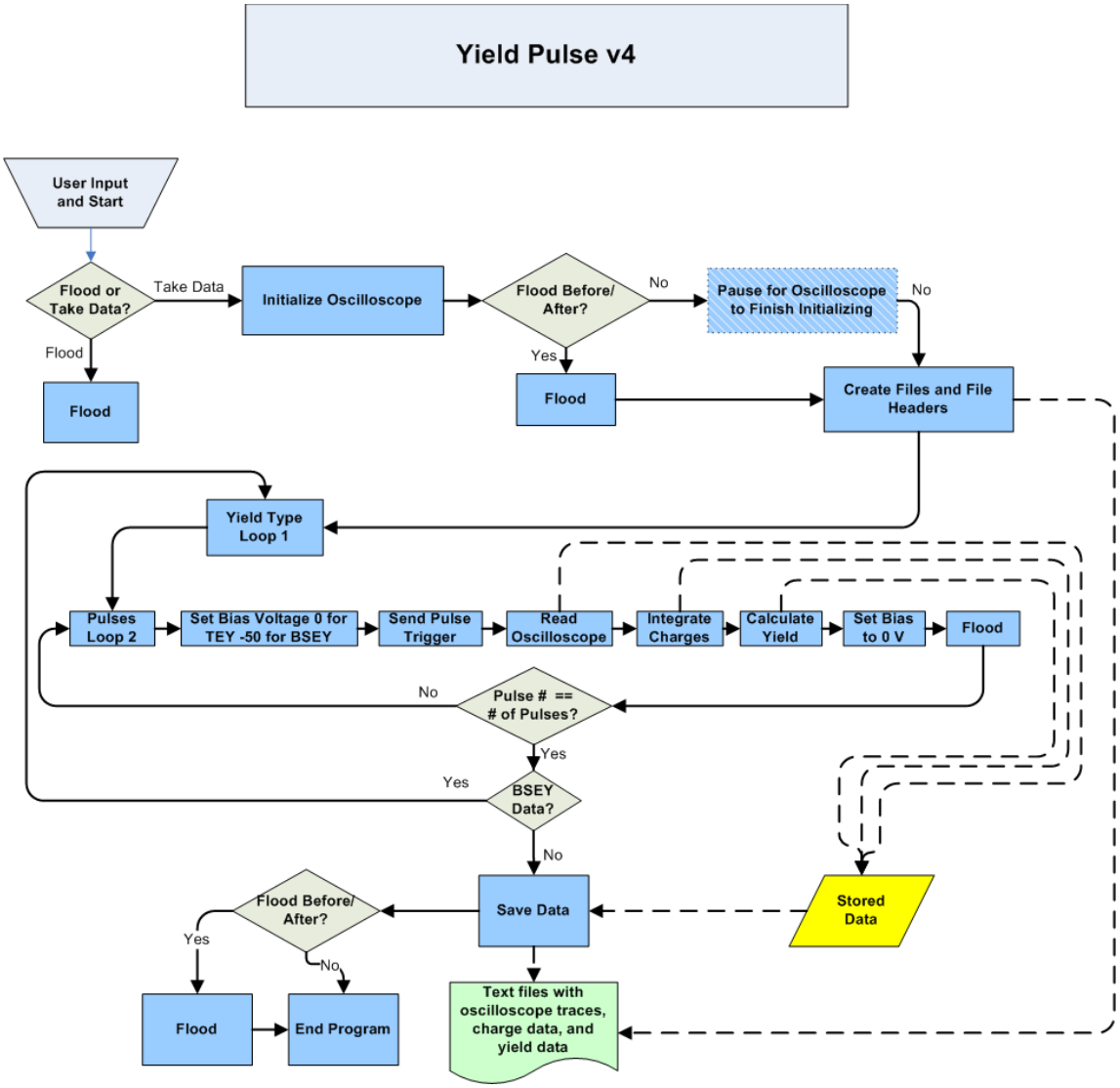

FIG. D.1. Labview Yield Pulse v4.vi flowchart.

Figure D.2 shows a similar flowchart representation of the DC Spectra.vi, which is used to record the change in the collector current with a swept grid bias potential. This produces the emitted electron energy distributions discussed in Sections 4.1.2 and 4.2.6.

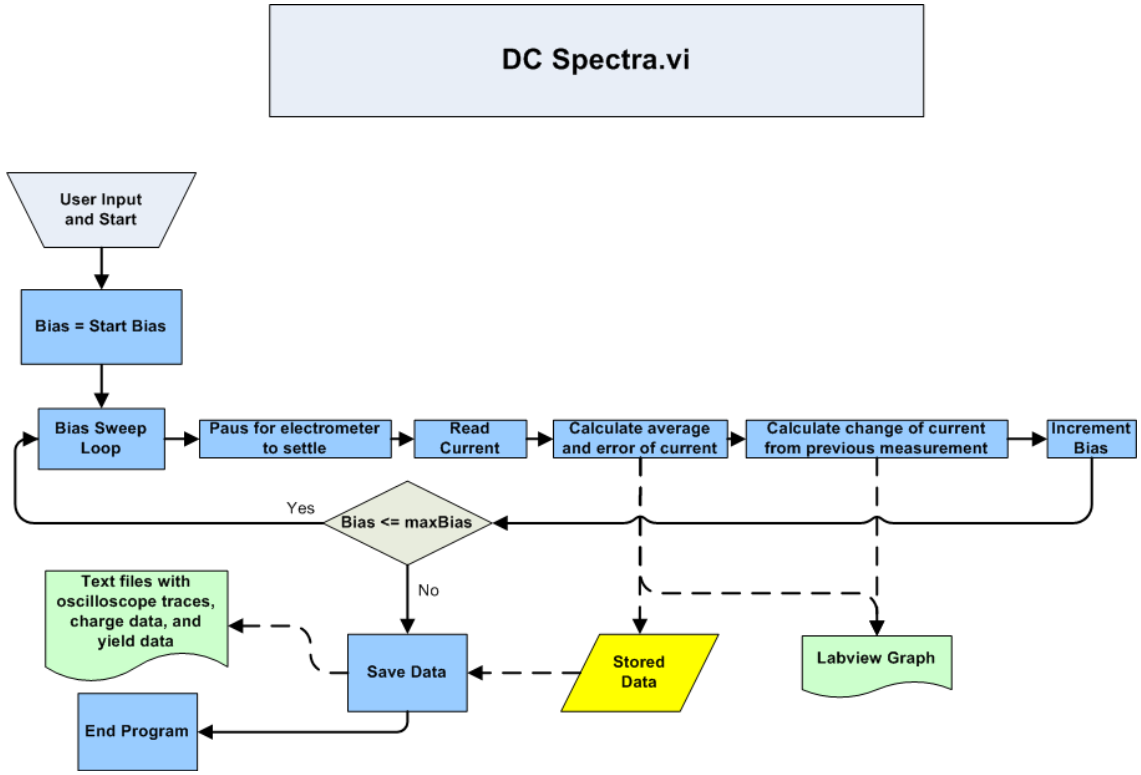

FIG. D.2. Labview DCSpect.vi flowchart.

APPENDIX E

UV LED MODIFICATIONS

To improve the neutralization capabilities of the HGRFA, a high-energy UV LED was added to remove negative deposited charge via the photoelectric effect and radiation-induced conductivity. This LED works much better than previous LEDs used, because it produces deeper UV light (~255 nm or ~4.9 eV) than previous technologies allowed. Because of LED failures, which were encountered due to ESD events in the chamber, some upgrades were made to better shield the LED from electron radiation, as well as protective circuitry to absorb ESD events.

UVTOP255

The new LEDs come in a TO18 case with a flat window cap from Sensor Electronic Technology, Inc (SETI). They produce a minimum wavelength of 255 nm with a peak wavelength of 260 nm with an average optical power of 300μW. An optical emission spectra is shown in Fig. 3.6.

When these LEDs were first added to the HGRFA, they tended to fail on a fairly regular basis. After discussing the problems we were having with SETi, we theorized that the failures were caused by some type of electrostatic discharge event between either wire insulation and the LED wires, or some other nearby insulator. To fix this problem, two opposing Zener diodes (a clipping circuit) were added to the LED circuit parallel to the LED to clip any voltage spikes caused by ESD events (see Fig. E.1).

The former TTL relay for the UVLED drew too much current from the TTL signal, which did not allow the flood gun relay to gate correctly. This was fixed by adding a resistor in series with the relay on the TTL inputs. A potentiometer was used to allow the resistance to be fine tuned so that the LED relay would draw just enough current to trigger. Lastly, two zener diodes were added to this circuit so that the output cable in the LED driver box could be safely disconnected and to add another layer of protection for the LED.

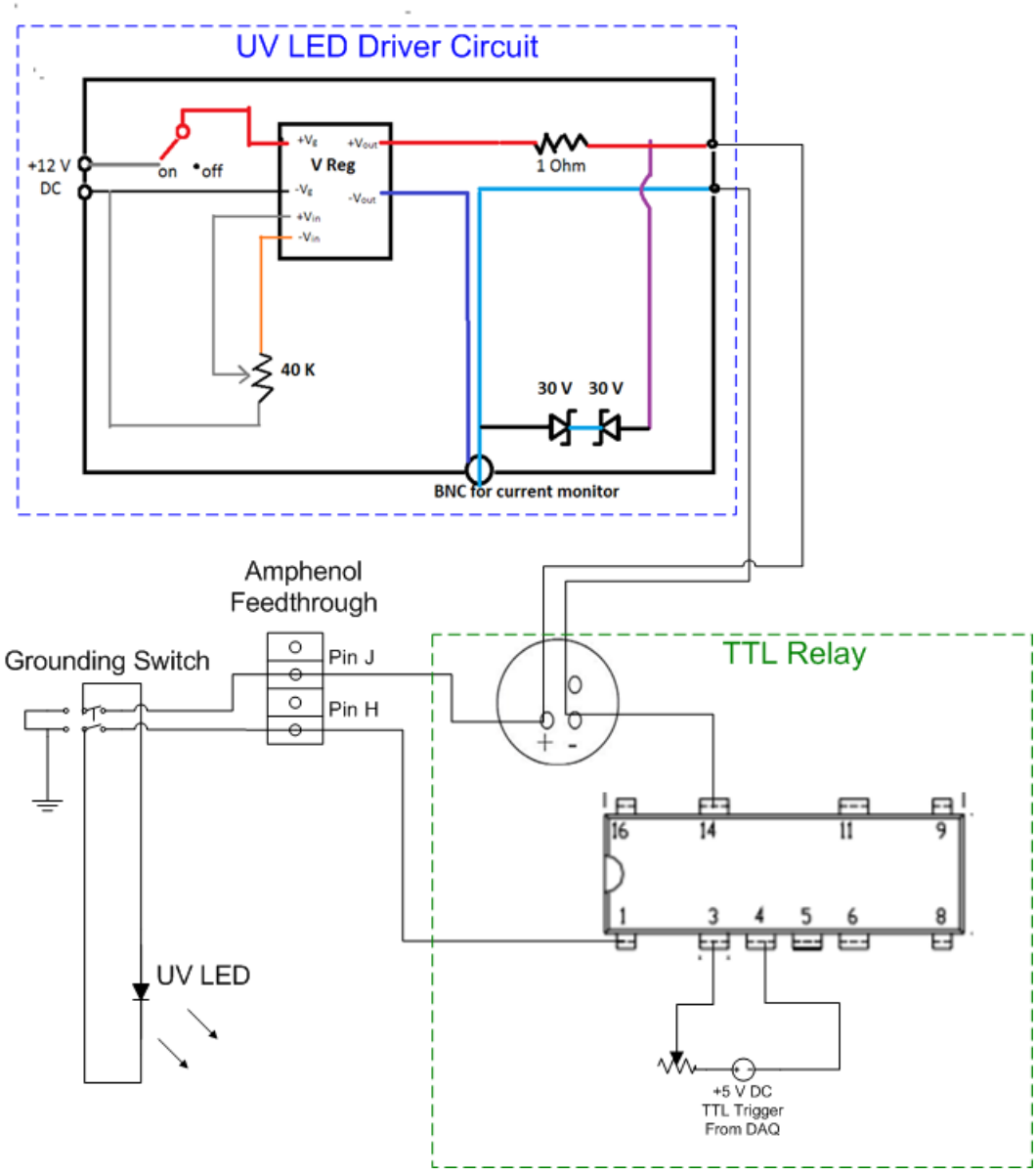

FIG. E.1. UV LED circuit. This figure shows a diagram of the UV LED circuit designed for this work. Main changes are: adding Zener diode clipping circuit and floating BNC for current monitoring to the driver box, and adding a current limiting resistor to the TTL input of the relay. A future modification of adding a grounding switch to the Amphenol feed through is also shown.

In addition to the circuit modifications described above, a new LED mount was designed to better shield the LED body from e^-/ion radiation in the chamber (Fig. E.2). This new LED mount completely covered the LED in a conductive shell to keep charge from building up in insulators close to the LED wires. This replaced the former shield, which was made out of braided ribbon cable, as shown in Fig. E.2(a). The LED leads were previously insulated from each other using fiberglass sleeves, which seemed to charge up and then discharge to the underlying wires. The leads previously had to be bent to the side so that the braided ribbon cable would not stick out too far and snag on protrusions in the chamber. The new mount keeps charging from occurring by isolating the areas that might experience charging at the back of the gun from the conducting wires deeper inside. Also, the only modification that is necessary before the LEDs can be inserted into the mount is to cut the leads down to the correct length to fit into the pin slots.

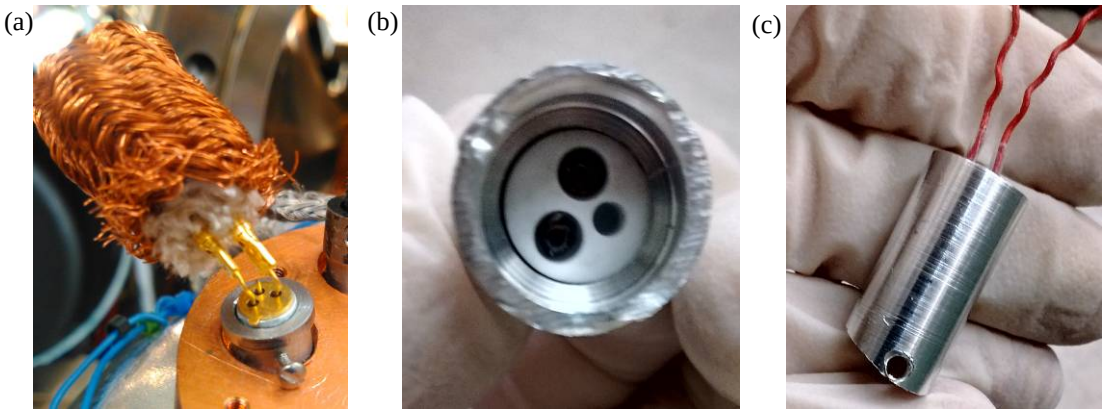

FIG. E.2. UV LED mount. This figure shows the old braided wire LED shield (a) and the new UV LED mount that was designed to protect the LED from charging in the vacuum chamber (b, c). Figures show internal (b) and external (c) views. Figure (b) also shows the slots where the LED pins are inserted.

APPENDIX F

VACUUM AND ELECTRONIC DIAGRAMS

Figure F.1 shows a diagram representing the vacuum system setup for the chamber used in this work. Figure F.2 shows the chamber wiring setup used to make pulsed-yield measurements. Both of these

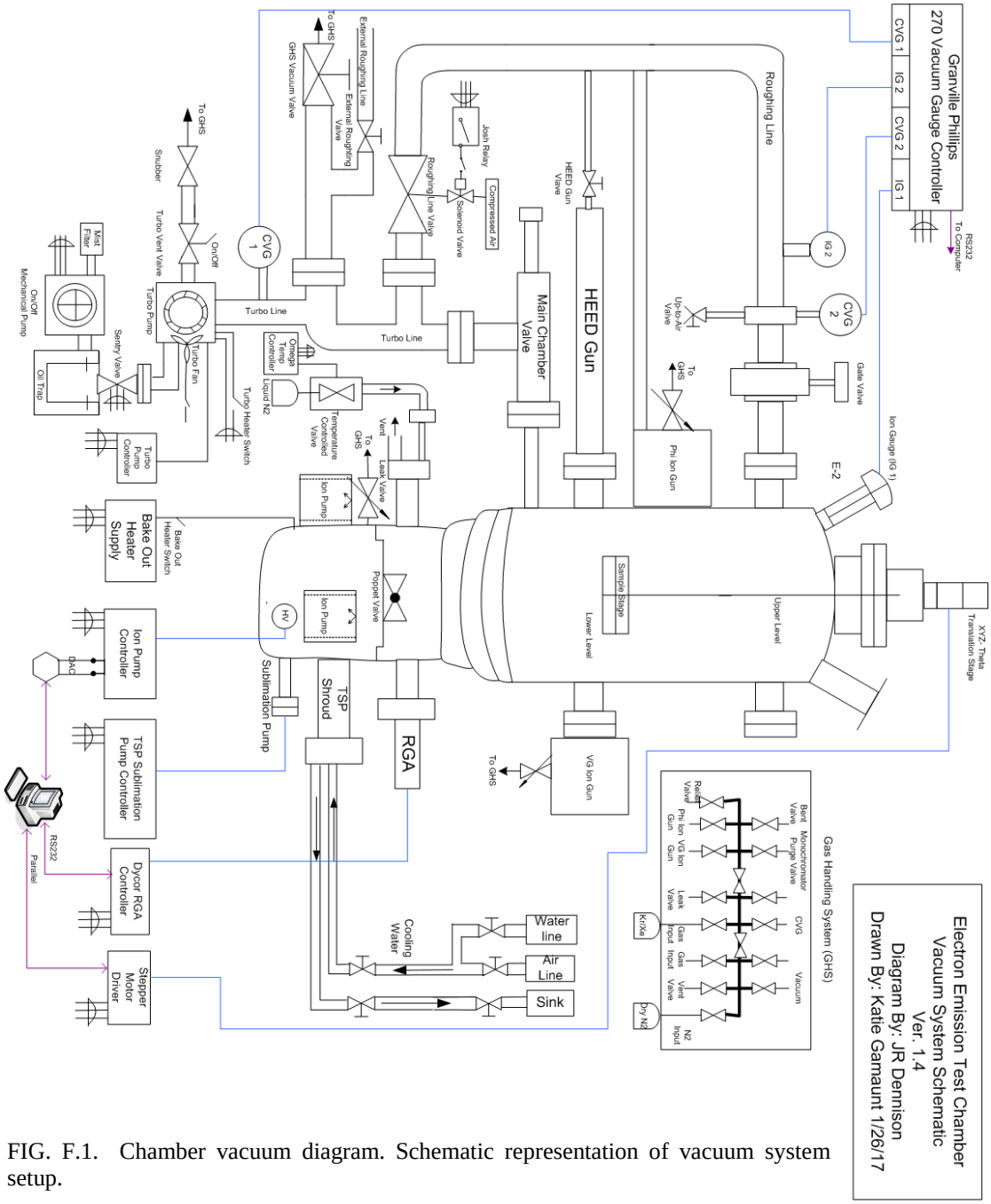

FIG. F.1. Chamber vacuum diagram. Schematic representation of vacuum system setup.

figures were made digitally to make it easier for changes to be made in the future.

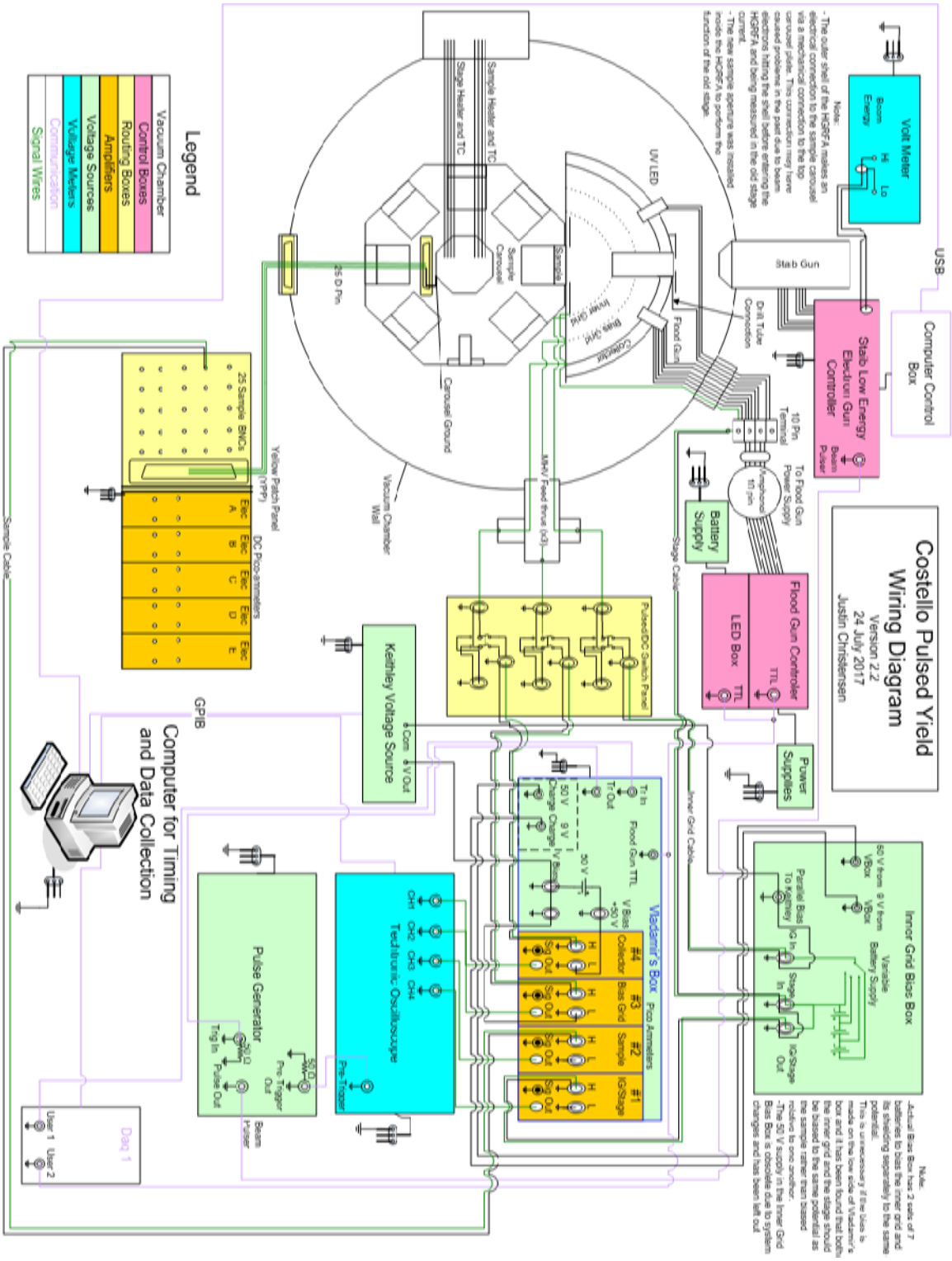

FIG. F.2. Pulsed-yield wiring diagram.

APPENDIX G

ACCOUNTING FOR LOST CHARGE IN TEY AND BSEY CALCULATIONS

In order to make absolute yield measurements, it is necessary to account for every incident and emitted electron used in the measurement. While the HGRFA is designed to capture nearly all the electrons used, there are still some small losses due to electrons emitted through the beam drift tube, under the sample aperture, and through the optics, and flood gun holes. Also, for BSEY measurements, the only component used to measure the backscattered electrons exclusively is the collector, so the efficiency of the collector, Γ_{coll}, is needed, which accounts for losses due to the transmission of the grids (ε_T). The main takeaways from this appendix are the following equations, which account for inefficiencies in the HGRFA. The calculation of TEY can be made as

$$\sigma(E_0) = \frac{(Q_{coll}+Q_{grid}+Q_{stage}+Q_{IG})/\Gamma_{HGRFA}}{Q_{Sample}+(Q_{coll}+Q_{grid}+Q_{stage}+Q_{IG})/\Gamma_{HGRFA}} = \frac{Q_{coll}/\Gamma_{coll}}{Q_{Sample}+(Q_{coll}+Q_{grid}+Q_{stage}+Q_{IG})/\Gamma_{HGRFA}}, \quad \text{(G.1)}$$

where Γ_{HGRFA} is the fraction of emitted electrons, which are contained within the HGRFA, and Γ_{coll} is the fraction of emitted electrons, which deposit in the collector. Since BSEY measurements use the bias grid to screen out low-energy electrons and only BSEs deposit in the collector, an equation similar to the last one above is used giving

$$\eta(E_0) = \frac{Q_{out}^{BSE}(E_0)}{Q_{in}} = \frac{Q_{coll}^{-50\,V}/\Gamma_{coll}^{BSE}}{Q_{sample}^{-50\,V}+(Q_{coll}^{-50\,V}+Q_{grid}^{-50\,V}+Q_{stage}^{-50\,V}+Q_{IG}^{-50\,V})/\Gamma_{HGRFA}}, \quad \text{(G.2)}$$

where the superscript $^{-50\ V}$ denotes measurements done with the bias grid at -50 V. The rest of this appendix will explain how to arrive at these equations, as well as how the Γ factors are determined.

The equation for TEY can most simply be defined as

$$\sigma(E_0) \equiv \frac{Q_{out}(E_0)}{Q_{in}} = \frac{Q_{coll}+Q_{grid}+Q_{stage}+Q_{IG}+Q_{lost}}{Q_{Sample}+Q_{coll}+Q_{grid}+Q_{stage}+Q_{IG}+Q_{lost}}. \quad \text{(G.3)}$$

The numerator is a sum of all HGRFA components plus the electrons, which are lost through an opening in the HRFA. This is done because all electrons that are emitted from the material will either end up in one of the HGRFA elements or being lost. Since the incident charge will either be deposited in the sample or be

emitted, the denominator is just the sum of the sample charge and the emitted charge described above. Since we cannot measure the amount of charge that is lost, we account for it using a couple of assumptions. The first assumption is that the fraction of emitted electrons that goes to each element of the HGRFA or is lost is a constant irrespective of energy and material. This assumption is reasonable because the emitted electron angular distribution is largely not dependent on incident energy or material, and this allows the fractions of emitted electrons to be calculated using the geometry of the HGRFA. This assumption can be written mathematically as

$$Q_{element} = \Gamma_{element} \cdot Q_{out} \;\rightarrow\; Q_{out} = {}^{Q_{element}}\!/_{\Gamma_{element}}\;, \tag{G.4}$$

which leads to

$$Q_{out} = Q_{coll} + Q_{grid} + Q_{stage} + Q_{IG} + Q_{lost} = \left(\Gamma_{coll} + \Gamma_{grid} + \Gamma_{stage} + \Gamma_{IG} + \Gamma_{lost}\right) \cdot Q_{out}$$

$$\rightarrow\; \Gamma_{coll} + \Gamma_{grid} + \Gamma_{stage} + \Gamma_{IG} + \Gamma_{lost} = 1. \tag{G.5}$$

From this point on, I will denote the sum over HGRFA elements using a subscript HGRFA. Γ_{lost} is very difficult to measure. In the past it has been calculated using measured emission angular distributions and the geometry of the HGRFA. Another option that may be used is to measure the current of a tightly focused DC electron beam over a Faraday cup and then send the same beam into the HGRFA placed over a conductive sample and measure the charge deposited in the sample and each of the HGRFA elements. Using the following equations,

$$I_{in} = I_{sample} + I_{HGRFA} + I_{lost}$$

$$\therefore I_{lost} = I_{in} - I_{sample} - I_{HGRFA} \text{ and } I_{out} = I_{HGRFA} + I_{lost} = I_{in} - I_{sample},$$

the fraction of emitted electrons that are lost is given as

$$\Gamma_{lost} \equiv \frac{I_{lost}}{I_{out}} = \frac{I_{in} - I_{sample} - I_{HGRFA}}{I_{in} - I_{sample}} = 1 - \frac{I_{HGRFA}}{I_{in} - I_{sample}}. \tag{G.6}$$

Since the last term in the previous equation is just the fraction of emitted electrons that are captured by the HGRFA, this can be rewritten as

$$\Gamma_{HGRFA} = \frac{I_{HGRFA}}{I_{in} - I_{sample}} \rightarrow \Gamma_{lost} = 1 - \Gamma_{HGRFA}. \tag{G.7}$$

Finally, this allows us to rewrite Eq. (G.3) as

$$\sigma(E_0) \equiv \frac{Q_{out}(E_0)}{Q_{in}} = \frac{(Q_{coll} + Q_{grid} + Q_{stage} + Q_{IG})/\Gamma_{HGRFA}}{Q_{Sample} + (Q_{coll} + Q_{grid} + Q_{stage} + Q_{IG})/\Gamma_{HGRFA}},$$

which gives us the first result of Eq. (G.1). The second result of Eq. (G.1) can be reached using the implication of Eq. (G.4) with

$$Q_{out} = {Q_{coll}}/{\Gamma_{coll}},$$

giving

$$\sigma(E_0) \equiv \frac{Q_{out}(E_0)}{Q_{in}} = \frac{Q_{coll}/\Gamma_{coll}}{Q_{Sample} + (Q_{coll} + Q_{grid} + Q_{stage} + Q_{IG})/\Gamma_{HGRFA}}.$$

From past experience it has been observed that Γ_{coll} does, in fact, change at low incident energies. This is presumed to be caused by an increased susceptibility of low-energy electrons to be affected by small electric fields in the HGRFA. While it is not readily apparent what may be causing these small electric fields, it is theorized that a possible source is the difference of work functions between dissimilar materials in and around the HGRFA. While this may seem to break down the assumptions necessary to come to the above results, it has also been observed that the change in collector efficiency is balanced out by an apparently equal change in the fraction of electrons deposited in the sample aperture (stage). This causes Γ_{HGRFA} to stay nearly constant since it is a sum of all HGRFA element efficiencies.

It has been further assumed that the change that occurs in the collector efficiency is not dependent on the material being measured, but only on the incident energy. This would suggest that the collector efficiency may be measured at different energies using the equation

$$\Gamma_{coll} = \frac{Q_{coll}^{0V}}{(Q_{coll}^{0V} + Q_{grid}^{0V} + Q_{stage}^{0V} + Q_{IG}^{0V})/\Gamma_{HGRFA}}. \tag{G.8}$$

This would be an interesting assumption to test to see if this efficiency is, in fact, not dependent on the material being tested. A way to spot check the result of Eq. (G.8) has been proposed using the transmission of each of the two hemispherical grids, ε_T. Since there are two grids, the relationship between Γ_{coll} and Γ_{HGRFA} should be

$$\Gamma_{coll} \approx {\varepsilon_T}^2 \cdot \Gamma_{HGRFA}.$$

Combining Eq. (G.8) with this result gives

$$\frac{\Gamma_{coll}}{\Gamma_{HGRFA}} \approx {\varepsilon_T}^2 = \frac{Q_{coll}^{0\,V}}{Q_{coll}^{0\,V}+Q_{grid}^{0\,V}+Q_{stage}^{0\,V}+Q_{IG}^{0\,V}}.$$

Nickles measured the combined transmission of the two grids to be ${\varepsilon_T}^2 = 0.72$ (Nickles,2002).

The calculation of BSEY is very similar to the last equality in Eq. (G.1). The only thing to point out here is that for BSEY, the definition of collector efficiency is the fraction of emitted BSEs, that reach and are captured by the collector. This may be slightly off because of the possibility of these high-energy BSEs to backscatter from the collector surface and end elsewhere. This can be adjusted for by using the backscattered yield of the collector (coated in aquadag®), or

$$Q_{coll}^{-50\,V} = \Gamma_{coll} \cdot Q_{BSE} - \eta_{coll} \cdot \Gamma_{coll} \cdot Q_{BSE} = \Gamma_{coll} \cdot (1 - \eta_{coll}) \cdot Q_{BSE}, \tag{G.9}$$

which gives a corrected BSE collector efficiency of

$$\Gamma_{coll}^{BSE} = \Gamma_{coll} \cdot (1 - \eta_{coll}). \tag{G.10}$$

Finally, this brings us to our equation for BSEY [Eq. (G.2)] accounting for electrons lost from the HGRFA and the BSE collection efficiency of the collector as

$$\eta(E_0) = \frac{Q_{BSE}(E_0)}{Q_{in}} = \frac{Q_{coll}^{-50\,V}/\Gamma_{coll}^{BSE}}{Q_{sample}^{-50\,V}+(Q_{coll}^{-50\,V}+Q_{grid}^{-50\,V}+Q_{stage}^{-50\,V}+Q_{IG}^{-50\,V})/\Gamma_{HGRFA}}.$$